



# Naval Research Laboratory

Washington, DC 20375-5320

NRL/MR/5050--01-8565

## Ultra-Near Field Facility for RCS Research

L. N. MEDGYESI-MITSCHANG

P. G. MOORE

D. L. SMITH

S. G. LAMBRAKOS

*Signature Technology Office*

August 31, 2001

Approved for public release; distribution is unlimited.

20011010 078

<b>REPORT DOCUMENTATION PAGE</b>				<i>Form Approved</i> <b>OMB No. 0704-0188</b>	
Public reporting burden for this collection of information is estimated to average 1 hour per response, including the time for reviewing instructions, searching existing data sources, gathering and maintaining the data needed, and completing and reviewing this collection of information. Send comments regarding this burden estimate or any other aspect of this collection of information, including suggestions for reducing this burden to Department of Defense, Washington Headquarters Services, Directorate for Information Operations and Reports (0704-0188), 1215 Jefferson Davis Highway, Suite 1204, Arlington, VA 22202-4302. Respondents should be aware that notwithstanding any other provision of law, no person shall be subject to any penalty for failing to comply with a collection of information if it does not display a currently valid OMB control number. <b>PLEASE DO NOT RETURN YOUR FORM TO THE ABOVE ADDRESS.</b>					
<b>1. REPORT DATE (DD-MM-YYYY)</b> August 31, 2001		<b>2. REPORT TYPE</b> Memorandum		<b>3. DATES COVERED (From - To)</b>	
<b>4. TITLE AND SUBTITLE</b>  Ultra-Near Field Facility for RCS Research				<b>5a. CONTRACT NUMBER</b>	
				<b>5b. GRANT NUMBER</b>	
				<b>5c. PROGRAM ELEMENT NUMBER</b>	
<b>6. AUTHOR(S)</b>  L.N. Medgyesi-Mitschang, P.G. Moore, S.L. Smith, and S.G. Lambrakos				<b>5d. PROJECT NUMBER</b>	
				<b>5e. TASK NUMBER</b>	
				<b>5f. WORK UNIT NUMBER</b>	
<b>7. PERFORMING ORGANIZATION NAME(S) AND ADDRESS(ES)</b>  Naval Research Laboratory Washington, DC 20375-5320				<b>8. PERFORMING ORGANIZATION REPORT NUMBER</b>  NRL/MR/5050--01-8565	
<b>9. SPONSORING / MONITORING AGENCY NAME(S) AND ADDRESS(ES)</b>  Office of Naval Research 800 North Quincy Street Arlington, VA 22217-5660				<b>10. SPONSOR / MONITOR'S ACRONYM(S)</b>	
				<b>11. SPONSOR / MONITOR'S REPORT NUMBER(S)</b>  None	
<b>12. DISTRIBUTION / AVAILABILITY STATEMENT</b>  Approved for public release distribution is unlimited.					
<b>13. SUPPLEMENTARY NOTES</b>					
<b>14. ABSTRACT</b>  This investigation demonstrated, experimentally and theoretically, the application of near field and ultra-near field techniques in the microwave region to characterize the scattering and radiation phenomena near targets and in the reactive region of antenna. The Ultra-Near Field Facility research facility was designed and built at NRL for this purpose. Requisite sensors and associated processing software for measuring the ultra-near fields from bistatically illuminated targets as well as antenna systems were developed and tested.  The present phase of the program focused principally on the investigation of the ultra-near field scattering from planar structures. Important features of EM phenomena associated with ship stacks/masts can be analyzed by studying the scattering from classes of planar structures. This motivated the present approach.  To gain deeper insight into the scattering mechanisms and to characterize the fields in the proximity of such surfaces, extensive computer simulations were also carried out. In the modeling, it was assumed that the surfaces were two dimensional (2-D) permitting the effect of vertical and horizontal polarization to be studied independently. The numerical simulations were based on a method of moments formulation for bodies of translation (BOTs). These constitute a general class of 2-D surfaces. They are extensively treated in the literature and thus provide a robust departure point for this effort.  The propagated and evanescent fields in the proximity of these surfaces were delineated using frequency wave-vector ( $\omega$ - $\kappa$ ) transformations of the calculated and measured fields. The effect of surface discontinuities on the propagating and evanescent field structure was examined. Preliminary investigations were also carried out for selected finite quasi-periodic arrays and models provided by NSWCCD. As an adjunct to these studies, the NRL range was also used to map the reactive region of antennas supplied by the Naval Postgraduate School. Exploratory experiments were also carried out for a ship model supplied by SRI. This data is not included in this report.					
<b>15. SUBJECT TERMS</b>  Ultra-near field measurements, Evanscent and propagating fields, Frequency wave-vector transformation, Computer simulation					
<b>16. SECURITY CLASSIFICATION OF:</b>			<b>17. LIMITATION OF ABSTRACT</b>  UL	<b>18. NUMBER OF PAGES</b>  105	<b>19a. NAME OF RESPONSIBLE PERSON</b> L.N. Medgyesi-Mitschang
<b>a. REPORT</b> Unclassified	<b>b. ABSTRACT</b> Unclassified	<b>c. THIS PAGE</b> Unclassified			<b>19b. TELEPHONE NUMBER (include area code)</b> 202-767-6893

## TABLE OF CONTENTS

Preface.....	v
EXECUTIVE SUMMARY.....	E-1
1. BACKGROUND.....	1
2. EXPERIMENTAL INVESTIGATIONS.....	2
2.1. Description of NRL Ultra-near field Facility	
2.2. Probe Issues in Ultra-near field Measurements	
2.3. Experimental Measurements	
2.4 Ultra-Near Field Measurements of NSWCCD Cubes	
3. THEORETICAL/ANALYTICAL INVESTIGATIONS.....	17
3.1. Formulation for p.e.c. BOTs: Case I	
3.2. $\omega$ - $\kappa$ Transformation for Case I	
3.3. Formulation for Penetrable BOTs: Case II	
3.4. $\omega$ - $\kappa$ Transformation for Case II	
4. NUMERICAL RESULTS.....	27
5. SUMMARY/CONCLUSIONS.....	38
APPENDIX A:	
ANCILLARY EQUATIONS FOR SECTION 3 FORMULATIONS.....	39
APPENDIX B:	
MONO- AND BI-STATIC RCS CALCULATIONS FOR 2-D ANALOGS OF NSWCCD TARGETS.....	43
APPENDIX C:	
TECHNOLOGY TRANSFER AND NAVY RELEVANCE .....	97
REFERENCES.....	99

## PREFACE

This report is an account of the work performed by the Naval Research Laboratory (NRL) Code 5050, under sponsorship of the Office of Naval Research (ONR). The report covers the time period from 1 April 1999 through 30 September 2000. Dr. Ronald Radlinski was the contract monitor. The investigators on this effort were: Drs. Douglas Smith, Peter Moore and Samuel Lambrakos and Louis Medgyesi-Mitschang. Dr. Smith was responsible for all phases of the experimental effort, including the design of the Ultra-Near Field Facility at NRL. Dr. Moore assisted by Dr. Lambrakos provided analytical and programming support for this effort. Dr. Medgyesi-Mitschang was the principal investigator.

Mr. Alex Stoyanov of the Naval Surface Weapons Center at Carderock (NSWCCD) provided the target cube fixtures. Mr. Paul Titterton of SRI provided a modified model of the Sea Shadow. Exploratory ultra-near field measurements were carried out for both sets of models. Preliminary measurements were made for antennas supplied by Professor Michael Morgan of NPS to support theoretical studies at the Naval Post Graduate School (NPS).

The support and encouragement of this project by Dr. Donald Forester of NRL is gratefully acknowledged as well as the constructive comments and insights provided by Dr. Earl Williams of the Acoustic Interaction Group of NRL (Code 7137).

## EXECUTIVE SUMMARY

This investigation consisted of experimental and analytical efforts. For the former, the Ultra-Near Field Facility was built at NRL. It is capable of measuring the bistatic fields near a scatterer or the fields in the reactive region of an antenna or an array. The probe techniques were refined to achieve the requisite sensitivity in polarization and absolute field magnitude when the field sampling was carried out to limits of  $0.1 \lambda$  to the target surface. To achieve high precision positioning of the probes, a robotic positioning system was specially developed for NRL by Orbit/FR. As is well known, experimentally produced high resolution  $\omega$ - $\kappa$  maps needed to delineate the propagating and evanescent fields near a target or an antenna, require enormous amounts of data processing. A special effort was made to automate this function.

Specific experimental accomplishments during this effort were:

- To enhance the scan versatility of the Ultra-Near Field Facility an additional degree of freedom was added to the Orbit/FR translating table. This enhancement allowed planar scans of high fidelity to be made over a 5 ft. x 5 ft. x 1 ft. (152.4 cm x 152.4 cm x 30.48 cm) volume. Additionally, cylindrical scans over a cylindrical volume with differential radii of one centimeter were made possible.
- The probes were refined to achieve the needed sensitivity for ultra-near field sampling and  $\omega$ - $\kappa$  mapping when large planar targets were illuminated near grazing or at the Peter's lobe traveling wave angles. The field sampling was extended to 18 GHz. Sufficient sensitivity in the experimental techniques were achieved to reveal the evanescent fields even in the deep shadowed region of an electrically large dihedral.
- A series of experiments were carried out to investigate the evanescent and propagating fields associated with gaps and edges on planar structures. Direct measurements were also made to map the evanescent field decay normal to a target surface.
- Selected finite periodic arrays of rods and strips were measured with and without dielectric substrates and R-cards. While these experiments were preliminary they demonstrated the sensitivity of the range and the associated data extraction techniques. Such validation is critical when multiple evanescent interactions are present as in the case of multi-layered surfaces and in structures associated with the isolation of array elements. It is also the necessary first step in measuring, simulating and hence understanding the surface wave behavior of frequency selective surfaces (FSS) and RCSR treatments in topside arrays.
- While the focus during this past year was on bistatic target scattering, a series of preliminary measurements were carried out for mapping the fields in the reactive region of antennas supplied by the Naval Postgraduate School and the Space Sciences Division at NRL. Exploratory measurements were also made on a scale ship model supplied by SRI and target cubes provided by NSWCCD.

On the analytical front, a general unified formulation was developed for simulating the bistatic fields at any point in the proximity of a target. Since many applications associated

with scattering from ship masts/stacks and coupling/isolation of antenna array elements involve flat or curved discontinuous surfaces, a theoretical formulation was chosen that treats arbitrary 2-D surfaces. The general class of such surfaces is often designated in the literature as bodies of translation (BOTs). In this formulation, the scattering (radiation) physics from BOTs is represented by coupled integro-differential equations. For maximum generality, the formulation allows the BOTs to be perfectly conducting (p.e.c.), penetrable or partially penetrable. For the penetrable cases the surfaces may consist of multi-layered materials. The layers can be dielectric or magnetic with complex permittivity and permeability. Inclusions, whether periodic or otherwise as in the case of frequency selective surfaces (FSS), are special cases.

To achieve a robust solution of the foregoing BOT formulation, the method of moments (MM) was used. Numerical implementation was carried out using an adaptation of a special version of the CARLOS code. This MM based code is computationally robust and has been extensively validated. A direct quasi-analytical method was found to compute the  $\omega$ - $\kappa$  maps. This approach results in an approximately 1000 fold increase in computational throughput compared to earlier indirect methods used in the first two years of this contract. As a consequence the scattering from even electrically large 2-D targets, i.e.  $1000 \lambda$  or greater, can now be computed on the ordinary workstations using this code adaptation.

Specific computational accomplishments during this effort were:

- The accuracy of the simulation of ultra-near fields and the  $\omega$ - $\kappa$  mapping in the direct BOT formulation was found to be superior when compared to the indirect computational methods used earlier. Benchmark calculations were made for large p.e.c. planar strips with and without gaps. The convergence was excellent. Surface wave suppression was demonstrated for TE polarization for surfaces with the larger gaps.
- The direct BOT formulation was used to produce  $\omega$ - $\kappa$  maps for large dihedrals with and without corner rounding and with surface gaps. The dihedrals were bistatically illuminated. A high resolution of the evanescent field structure was achieved even for large values of the surface propagation constant.
- Simulations were carried out for finite periodic arrays of strips. Diffractive broadening of the Bragg lobes was observed correlating with the width of the arrays. This phenomena was observed in both the forward and back-scattered fields.
- The direct BOT formulation was extended to the general case of penetrable surfaces, including those with embedded finite periodic arrays of elements. The penetrable region can be layered and have complex dielectric and magnetic properties. Due to resource limitations the full computer implementation for this case was not completed during this phase of the contract.

## 1. BACKGROUND

The RCS of an object whether air-borne, land-based or sea-based is an important observable used in a multitude of settings, such as surveillance, target discrimination, and target acquisition to name only a few. The RCS of a target is the net composite of all the propagating EM effects and interactions typically measured in the far field (Frauenhofer) region. These measurements are usually carried out in outdoor, ground reflection ranges. With the advent of compact ranges in the last 15 years, these measurements can now be done closer to the target. Often these facilities are termed near field ranges where the illuminated fields impinging on a target approximates a planar wave front. While these RCS measurements can now be carried out indoors under highly controlled, secure, and weather impervious conditions, the resultant fields measured are still the net composite of all scattering phenomena from the target. Using various electronic range gating and data processing techniques, some key EM phenomena of the target can be resolved but not all. One reason for this is that aside from experimental errors and ambiguities, the compact range measurements only capture the propagating components of the scattered fields. The evanescent (non-propagating) ones are mostly lost due to spatial attenuation. Thus the delineation of the scattering physics particularly of surface wave effects from such measurements, is incomplete.

The earlier successes using near field acoustic holography pioneered at NRL by Dr. Earl Williams and his team in extracting dynamic information of a target's scattering physics suggested that similar results should be possible in the microwave region. [1,2] This led to the present approach. Instead of using far- or pseudo far-field data (i.e. from compact ranges) to study a target's scattering characteristics, ultra-near fields are used instead. The specifics of the implementation of this approach are detailed below.

## 2. EXPERIMENTAL INVESTIGATIONS

### 2.1. Description of the NRL Ultra-Near Field Facility

This investigation proceeded on two complementary paths: experimental and analytical. For the former a research range, the Ultra-Near Field Facility, was built capable of measuring the bistatic fields near a target surface. This required the refinement and validation of probe techniques to achieve the requisite sensitivity (polarization and absolute field magnitude) when the field sampling was carried out to limits of  $0.1 \lambda$  or closer to the target surface. This required that the targets and probes to be positioned with great precision. To accomplish this, a robotic positioning system was specially developed by Orbit/FR for this application.

The essential features and dimensions of the NRL Ultra-Near Field Facility are summarized in Figure 1. A photograph of the range is given in Figure 2. The translating and rotating stages made by Orbit/FR, are specially constructed to provide a very stable platform for planar and cylindrical scans. Planar scans covering a volume of  $5 \text{ ft.}^2 \times 1 \text{ ft.}$  depth ( i.e.  $2.32 \text{ m}^2 \times 30.5 \text{ cm}$  ) are possible. Cylindrical scans can be made in small radial increments up to a maximum of 3.5 ft. (1.07 m) radius.

The probe signals are fed into a Hewlett Packard Network Analyzer and peripheral electronics. To achieve high resolution  $\omega$ - $\kappa$  maps needed to delineate propagating and evanescent fields near the target, enormous amounts of data have to be processed. Software was developed to carry out the FFTs and other processing of the probe data automatically and efficiently.

### 2.2. Probe Issues in Ultra-Near Field Measurements

The design and selection of the probes were among the most challenging aspects of this investigation. Significant effort went into characterizing the candidate probes. Some of the probes used in our experiments are depicted in Figure 3. Open-ended waveguide probes were also tested and used, but our experience showed that wire probes discussed below proved more versatile. Regardless of the type of probes used, the probe/target interaction is severe in ultra-near field electromagnetic measurements.

An ideal probe measures the local vector fields at a point without introducing distortions. Of course, this can not be realized in practice. Resonant probes implemented with resonant microstrip lines can provide substantial spatial resolutions on the order of  $1/1000 \lambda$ . The disadvantage is that the high Q of such probes makes their bandwidth very narrow. At the other extreme, low Q probes have good bandwidth but have correspondingly lower sensitivity.

To minimize the probe/target interactions, we experimented with loop probes with diameters much smaller than a  $\lambda$ , electrically small bow-tie probes and fractional wavelength monopole and dipole probes. [3,4] The latter were intermediate in their sensitivity and bandwidth compared to the resonant ones. Our experiments showed that an X-band dipole probe with a small etched balun worked best for the targets under consideration and the range of frequencies that we measured. The dipole had a polarization selectivity of nearly 20 dB at X-band. The dipole being a balanced element, also minimized the currents induced in the probe leads from re-radiation from the target. As a general



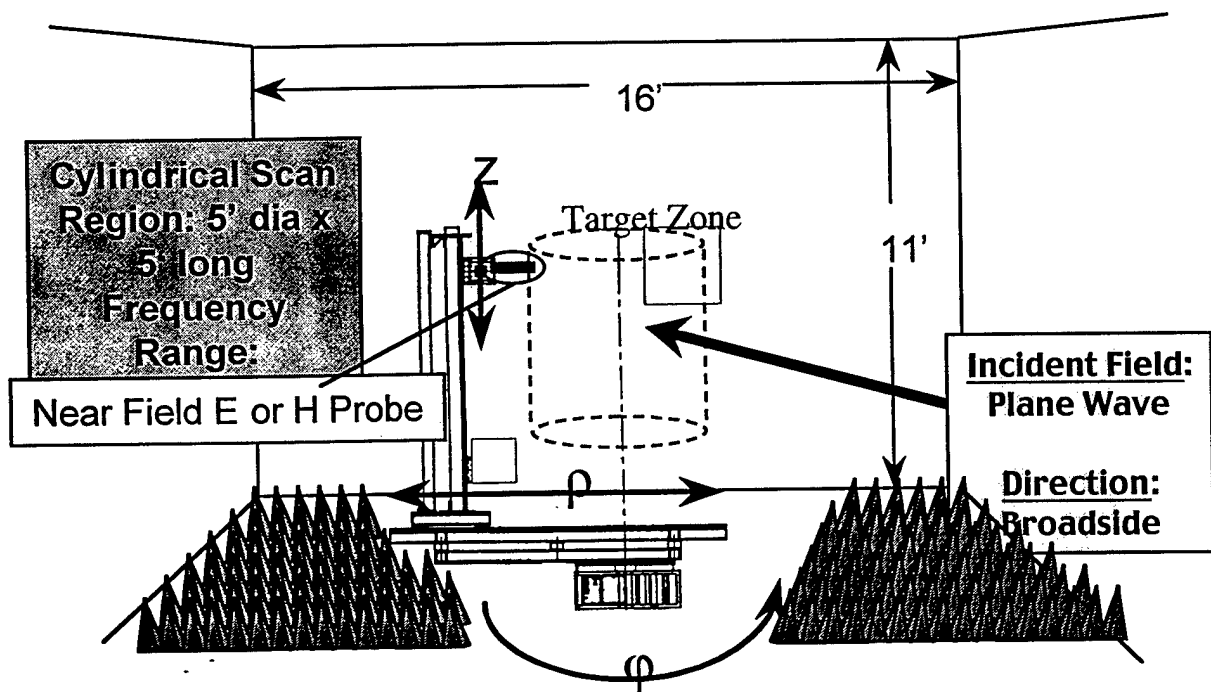


Figure 1. Diagram of the principal elements of the NRL Ultra-Near Field Facility.

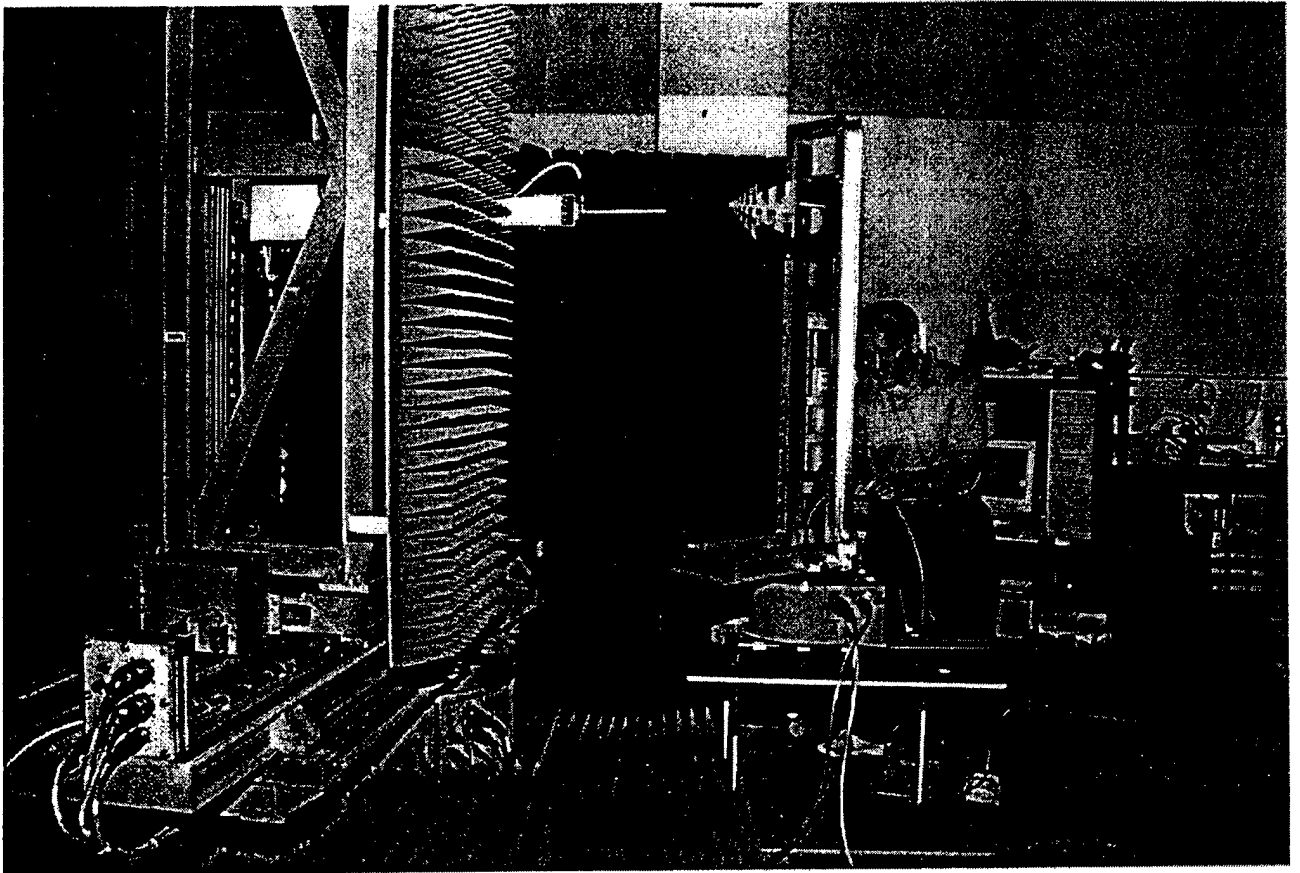


Figure 2: Photo of the NRL Ultra-Near Field Facility

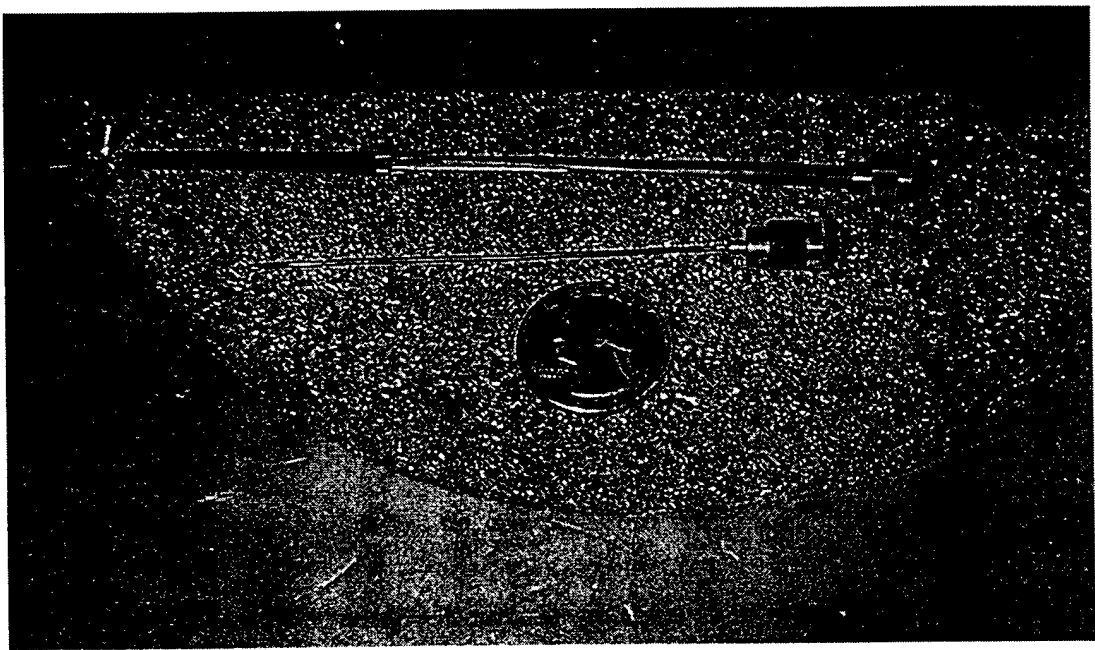


Figure 3: Wire probes used in the ultra-near field measurements

observation, the electrically small loops and monopoles are far less sensitive. In all cases calibration of the probes is difficult. No effective method was found for simultaneous absolute calibration of the small loop (magnetic field) probes and the monopole or dipole (electric field) probes. To support and guide the experimental investigations on the probes, selective computer simulations were also carried out to attempt to quantify probe/target interactions, particularly for the dipole probes. [3]

An electro-optic probe was designed for the present applications and ordered from Mission Research Corporation (MRC). Unfortunately due to technical difficulties experienced by the vendor, the probe was not received by NRL until the end of this contract. Hence only preliminary assessment of its characteristics could be made. However, it appears that its dynamic response is competitive with the X-band dipole probe described above. In addition, the major benefit of this class of probes is that distortions in the data due to ground loop pickup are eliminated since the leads to the probe are optic fibers.

### **2.3. Experimental Measurements**

Experiments were carried out for a series of targets to test the range sensitivity and stability, the probe/target interactions and the data processing software. Representative examples of this effort are summarized below.

To measure the ultra-near fields, the object under test was illuminated bistatically using a Singer broadband horn. The field scans were made for a fixed horn position set at a given illumination angle. Important considerations in the setup were the spot size and position of the source relative to the target. Generally for planar scans, the range of the scan was 3 to 6 inches (7.62 to 15.24 cm) beyond the target surface.

Canonic targets such as a rectangular plate and a dihedral were used to check the operation of the range. The plate was made of aluminum having dimensions of 9 x 18 inches (22.86 x 45.72 cm) and a thickness of 1/8 inches (0.372 cm). The edges were unbeveled. Measurements were also made with a copper taped surface having the same dimensions as the plate. This minimizes the thickness effects of the edges. The dihedral used in the experiments consisted of two of the rectangular aluminum plates described above joined together perpendicularly.

Exploratory measurements were also carried out for planar arrays of rods. These were made of aluminum having a length of 12 inches (30.48 cm) and with a diameter of 1/8 inches (0.372 cm). In addition, various combinations of R-cards and dielectric layers were used with the rod array to study the effects of Bragg lobes and evanescent field guidance. Exploratory measurements were also made of the reactive region of antennas supplied by the Naval Postgraduate School. This data was supplied to the School earlier. Additionally, preliminary ultra-near field data was collected on aluminum foiled target cubes supplied by NSWCCD and a ship model from SRI. The data on the latter will be summarized in a separate document.

### **2.4. Ultra-Near Field Measurements on NSWCCD Cubes**

A series of measurements were carried out on targets supplied by NSWCCD. The targets consisted of 2 ft. (60.96 cm) cubes made of plywood. The surfaces were covered with aluminum foil. One target cube was designated as having a "sharp" edge. The other cubes had edges with various radii of curvature. The nominal radii were 0.25, 0.5, and 0.625 in. (0.64, 1.27, and 2.02 cm). In all cases the edge roundness dimensions were not of high precision due to the plywood construction of the targets and the aluminum foiling. The roundness of the edges varied considerably along the edge. The cube with the nominally

sharp edge had an edge roundness variation of approximately 1/16 to 1/8 in. (0.16 cm to 0.32 cm) along its edges. Furthermore, at the time the cubes were received at NRL, some of the edges appeared to have some damage. It should be noted that for far field measurements, the distortions in the edge diffraction arising from edge imperfections of the cubes play only a secondary role when compared to the strong scattered fields from the faces of the cube. However in ultra-near field measurements, these distortions can significantly influence the evanescent field behavior near the edges.

Earlier monostatic RCS measurements were made by NSWCCD at an outdoor range to assess the edge effects. For reference, a series of computer simulations were made by NRL for the NSWCCD targets. These are summarized in Appendix B. Since the principal focus of the NSWCCD measurements and the ultra-near field measurements in the NRL range were the interaction of parallel edges of the target cubes, the computed results in the Appendix were carried out for equivalent infinite p.e.c cylinders. The calculations were made using the BOT option in the CARLOS code.

Figure 4 depicts the reference frame for the NRL experimental setup. The cubes were illuminated by the Singer horn at 45 degrees to the cube face. The scans were made parallel to the face for various offsets for both TM and TE polarization. In our convention, the TM and the TE polarization refer to the case where the electric field is perpendicular or parallel to the plane of illumination, respectively. For the TM case, the incident electric field is parallel to the edge of the cube; for the TE case, it is perpendicular.

The ultra-near electric fields were probed over a series of frequencies with the small dipole probe described earlier. The frequency response of the dipole peaked at 9 GHz with a gradual fall-off to the limiting frequencies of 4 and 18 GHz. The probe measured the total field (i.e. incident and scattered components) in the vicinity of the target. A few representative results of these measurements are summarized in the following figures.

In Figure 5, the ultra-near electric field scans are given for the cube with the sharp edge when the scan offset is 0.15 in. (0.038 cm). For the TM case, there is a significant beating phenomena present in the scans for  $x > 0$ . This is due to the constructive and destructive interference of the edge radiated fields and the incident illumination. This effect is observed at all frequencies. This effect can be understood by recognizing that the edges in TM polarization act as pseudo line sources producing the interference fields. As expected, the fields roll-off for  $x < 0$  as the probe recedes from the edge. Part of the roll-off is due to the divergence of the incident field beam. The roll-off is greatest at 14 GHz.

The corresponding results for TE polarization summarized in Fig. 5, are considered next. In contrast to the TM case, for  $x > 0$  there is minimal interference (beating) phenomena since the illuminating field is cross-polarized to the target edge. The fluctuations of the fields for  $x < 0$  are indicative of traveling waves excited along the face of the cube for this polarization. The effect increases with the electrical length of the cube face.

It is instructive to compare the ultra-near fields for the two polarizations at the more distant edge from the illuminating horn, i.e. at  $x = -24$  inches. The most striking effect is that the fields for TE polarization drop off sharply at the edge while those for the TM case do not. In fact for 10 GHz they increase. Similar results hold for the 14 GHz case as well. This phenomena is due to the  $O(1/\rho)$  functionality of the TM polarized currents near the edge where  $\rho$  is the distance from the edge. Thus the TM polarized currents near the edge are large and so are the associated ultra-near fields. On the other hand, in the TE case for a sharp edge, the currents on the surface must vanish as  $o(\rho)$ . This results in a sharp falloff

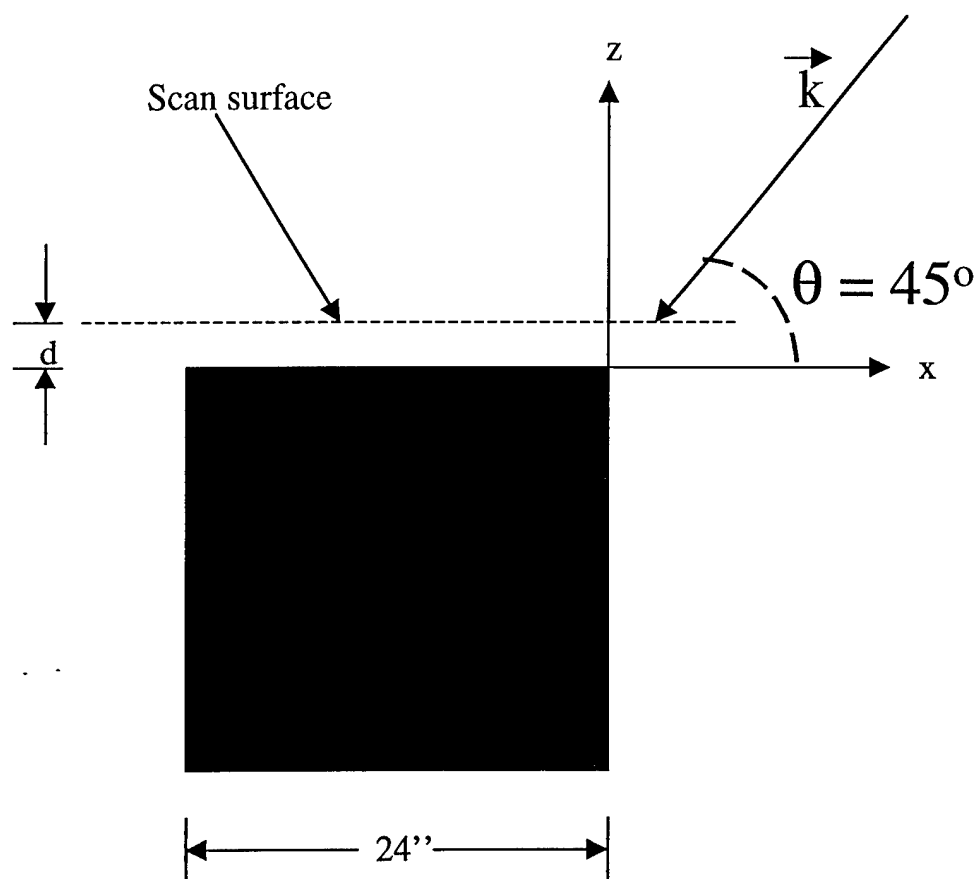


Figure 4: Reference frame used in the ultra near-field scans for the NSWCCD targets. The dashed line represents the scan surface at an offset  $d$  from the cube surface.

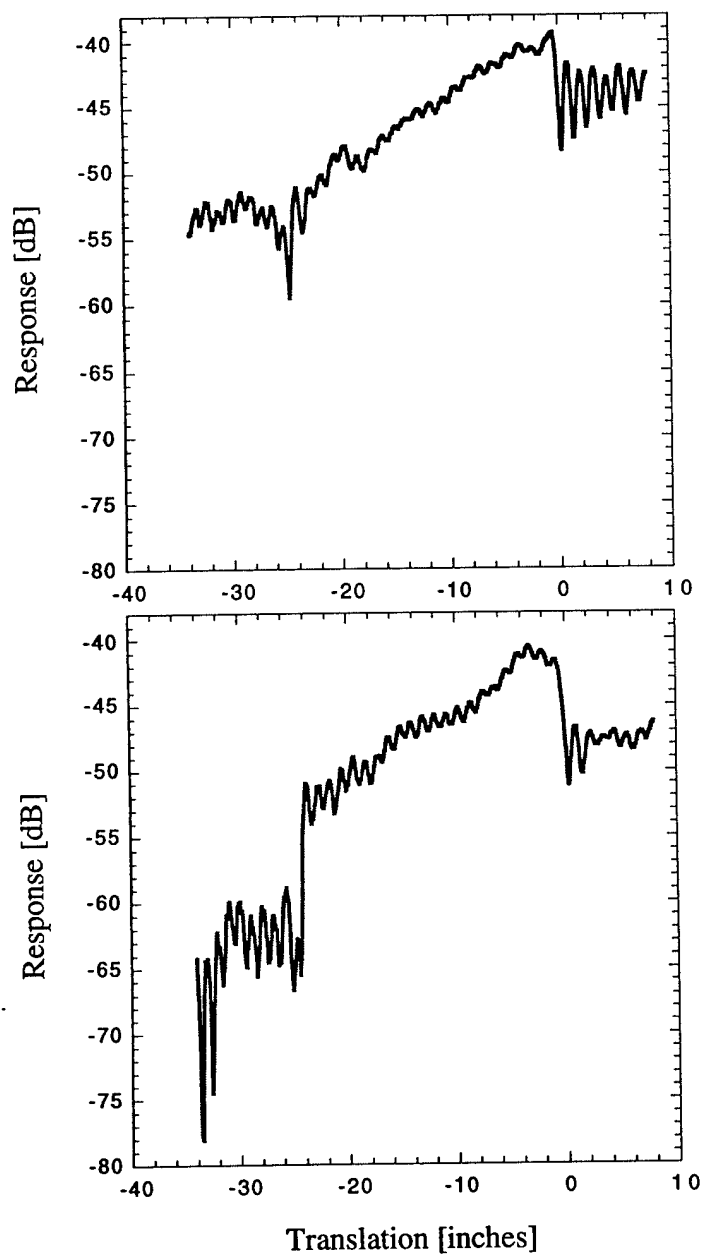


Figure 5: Measured ultra-near electric fields for the NSWCCD cube with a sharp edge: bistatic TM (top) and TE (bottom) polarized illumination at 6 GHz. Cube dimensions are 24 in. (60.96 cm) on a side. Dipole probe offset from the cube face for the scans is 0.15 in. (0.38 cm).

of the fields in the proximity of the edge. The drop-off would have been even more rapid if the edge had a zero radius of curvature. To summarize, the ultra-near fields are strongly correlated with the local behavior of the surface currents. By contrast far fields or fields several wavelengths from the scatterer mirror the integrated (averaged) distribution of the surface currents.

The ultra-near field results for the target cube with a rounded ( $r = 0.25$  in.) edge are summarized in Figure 6 for an offset of 0.15 in. As noted before with the actual target cube, this edge was not substantially different in edge radius than the previous "sharp" edge. The principal differences observed between the two cases are seen in TE polarization at 10 GHz and likewise at 14 GHz not shown here. Notably, the field roll-off for  $x < 0$  does not have the fluctuations associated with traveling waves observed before. This is not an unexpected result since the rounding of the edges particularly that of the farther edge from the illuminating horn, suppresses the traveling waves. With edge rounding, the fields are more likely to be scattered forward nonspecularly than in the backward direction toward the source.

As noted before with the sharp edged fixture in Figure 5, the behavior of the ultra-near fields is very different in the vicinity of a rounded trailing edge ( $x = -24$  in.). Again for the TM case there is an increase of the fields, while for the TE case the fields dropoff significantly. The same mechanism is in evidence here as the one described earlier with reference to Figure 5.

The corresponding results for an offset of 3 in. (7.62 cm) are given in Figure 7. In this case the fields are not ultra-near. They are measured at a distance comparable to a wavelength, i.e. at 10 GHz the offset distance is 2.54 wavelengths. At this distance, the evanescent fields have already decayed significantly. Thus the total electric near fields measured by the probe are dominated by the propagating fields in both polarizations although considerable interference (beating) in the total electric near fields (incident and scattered) remains for  $x > 0$ . At this distance the propagating fields begin to form lobes as evidenced by the "dips" in the curves for both polarizations.

Figures 8 and 9 compare the measured ultra-near electric fields at 6 and 10 GHz for TM polarization for the cubes with the sharp and the rounded ( $r = 0.25$  in.) edges. The slight displacement of the two curves near  $x = 0$ , is due to small experimental misalignments in the targets. The plots show that for TM polarization the edge interference (beating) effects noted before are somewhat smaller with the cube having the sharp edge than with the one having the rounded (0.25 in.) edge. In part this is due to the fact that the latter edge projects a greater surface area to the illuminating fields than the sharp edge. The corresponding results for the TE case are given in Figures 10 and 11. In this case the quasi-periodic fluctuations of the measured fields with the sharp edged cube for  $-24$  inches  $< x < 0$  are in contrast with the more muted fluctuating field behavior from the rounded edged cube.

These foregoing observations are consistent with and support the conclusions derived from the earlier NSWCCD far field data. Those investigations showed that the TE polarized monostatic RCS (measured at the angle bisecting the illuminated edge) was reduced when the edge was appropriately rounded. In TE polarization, the suppression of surface waves is the principal mechanism for RCS reduction when there is edge rounding. As the edge radius increases, the specular reflection from the illuminated surface of the edge increases, counter-balancing the diminution of the nonspecular surface waves. On the other hand for TM polarization, the parallel edges act as line sources that are relatively insensitive to the radius of the edge. Hence in this case, the RCS is impacted minimally by a rounding of the cube edges.



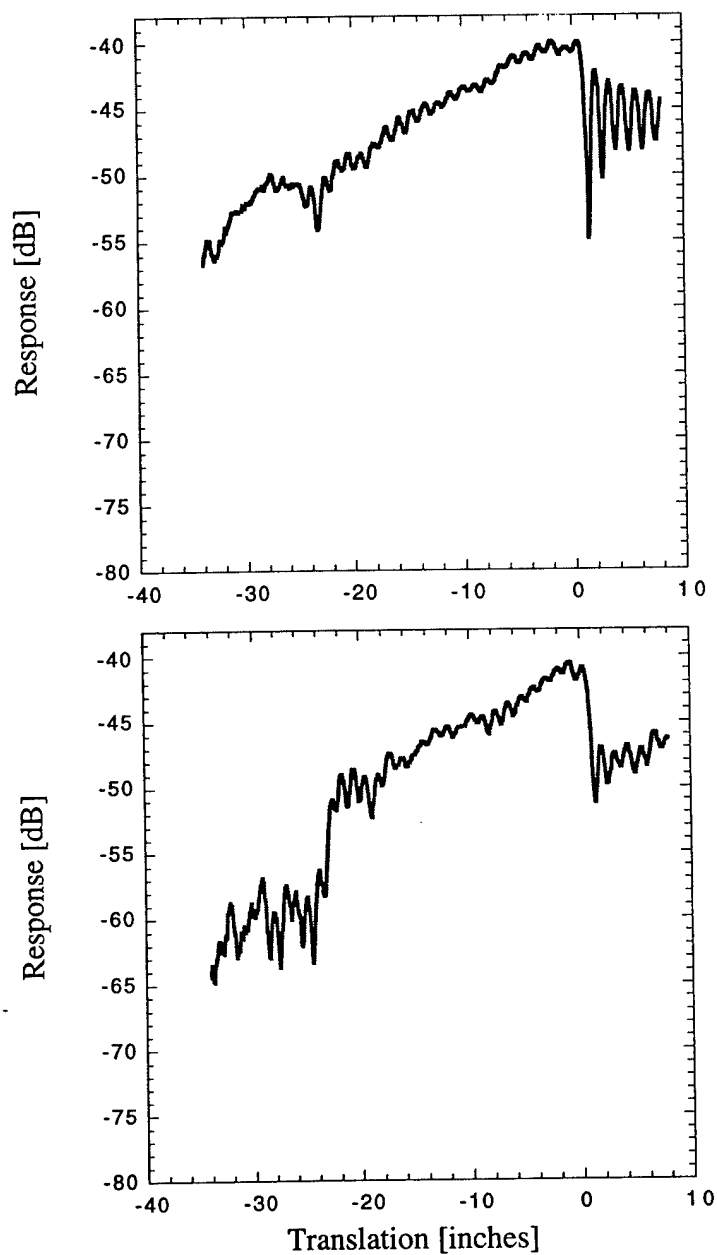


Figure 6: Measured ultra-near electric fields for the NSWCCD cube with a rounded edge: bistatic TM (top) and TE (bottom) polarized illumination. Cube dimensions are 24 in. (60.96 cm) on a side with an edge radius is 0.25 in. (0.64 cm). Dipole probe offset from the cube face for the scans is 0.15 in. (0.38 cm).

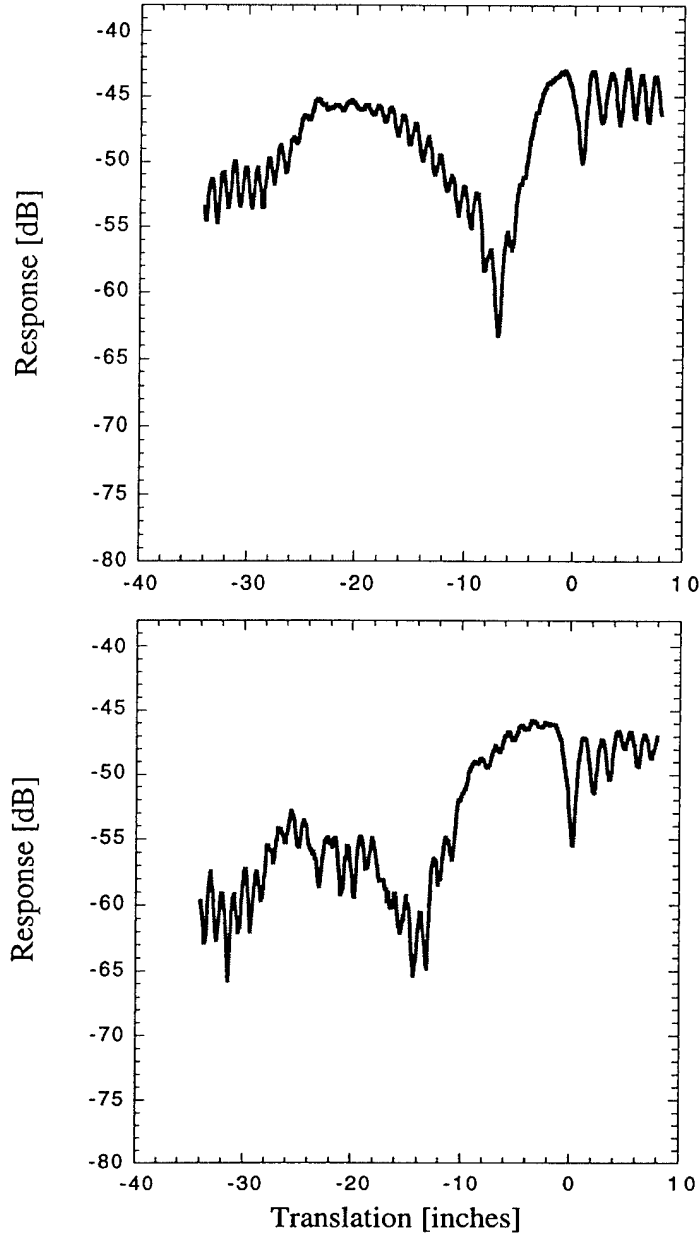


Figure 7: Measured ultra-near electric fields for the NSWCCD cube with a rounded edge: bistatic TM (top) and TE (bottom) polarized illumination. Cube dimensions are 24 in. (60.96 cm) on a side with an edge radius is 0.25 in. (0.64 cm). Dipole probe offset from the cube face for the scans is 3.0 in. (7.62 cm).

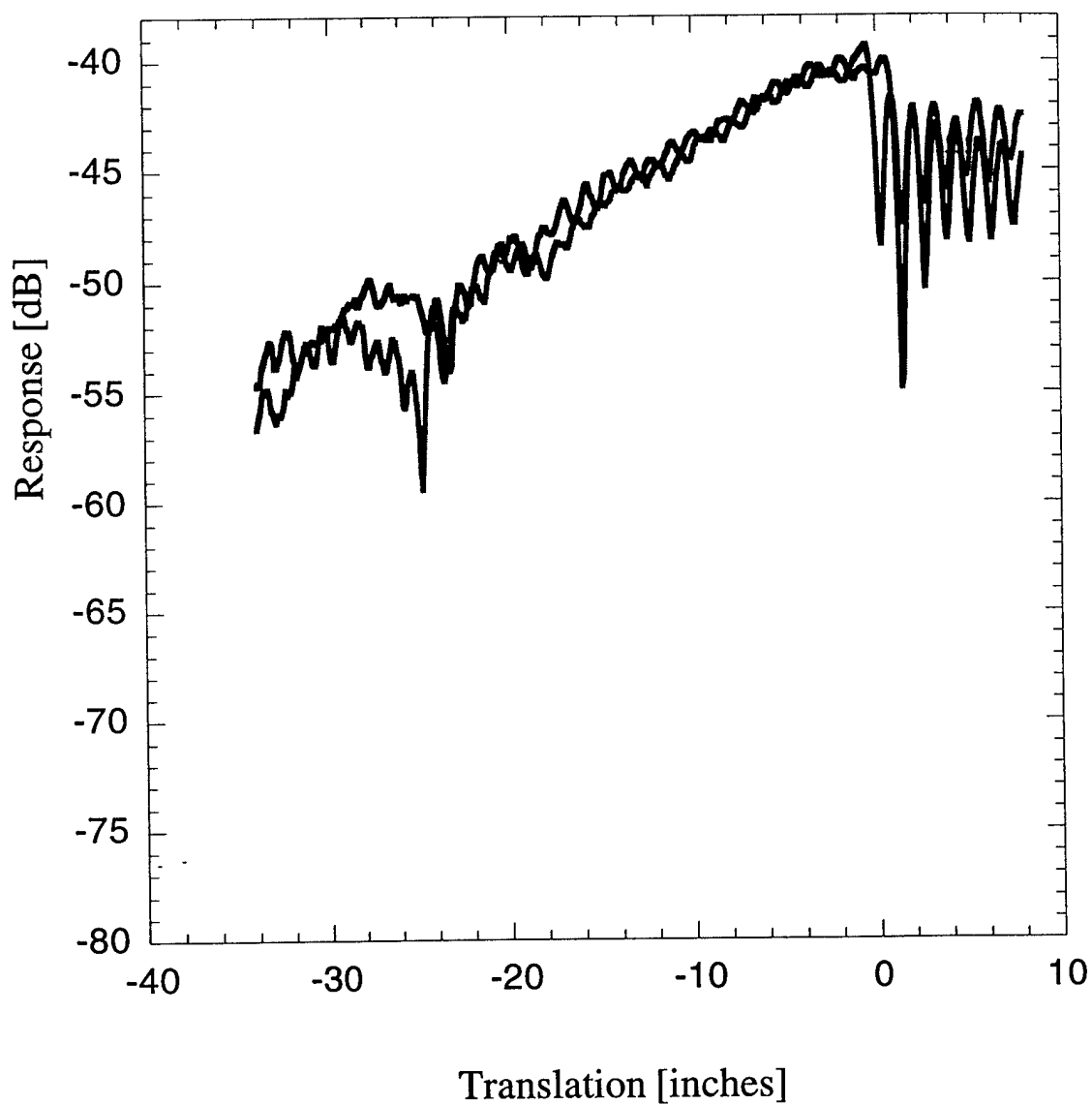


Figure 8: Comparison of the measured ultra-near electric fields for NSWCCD cubes with sharp (red) and rounded (blue) edges: bistatic TM polarized illumination at 6 GHz. Cube with the rounded edge has an edge radius of 0.25 in. (0.64 cm). Probe offset is 0.15 in. (0.38 cm).

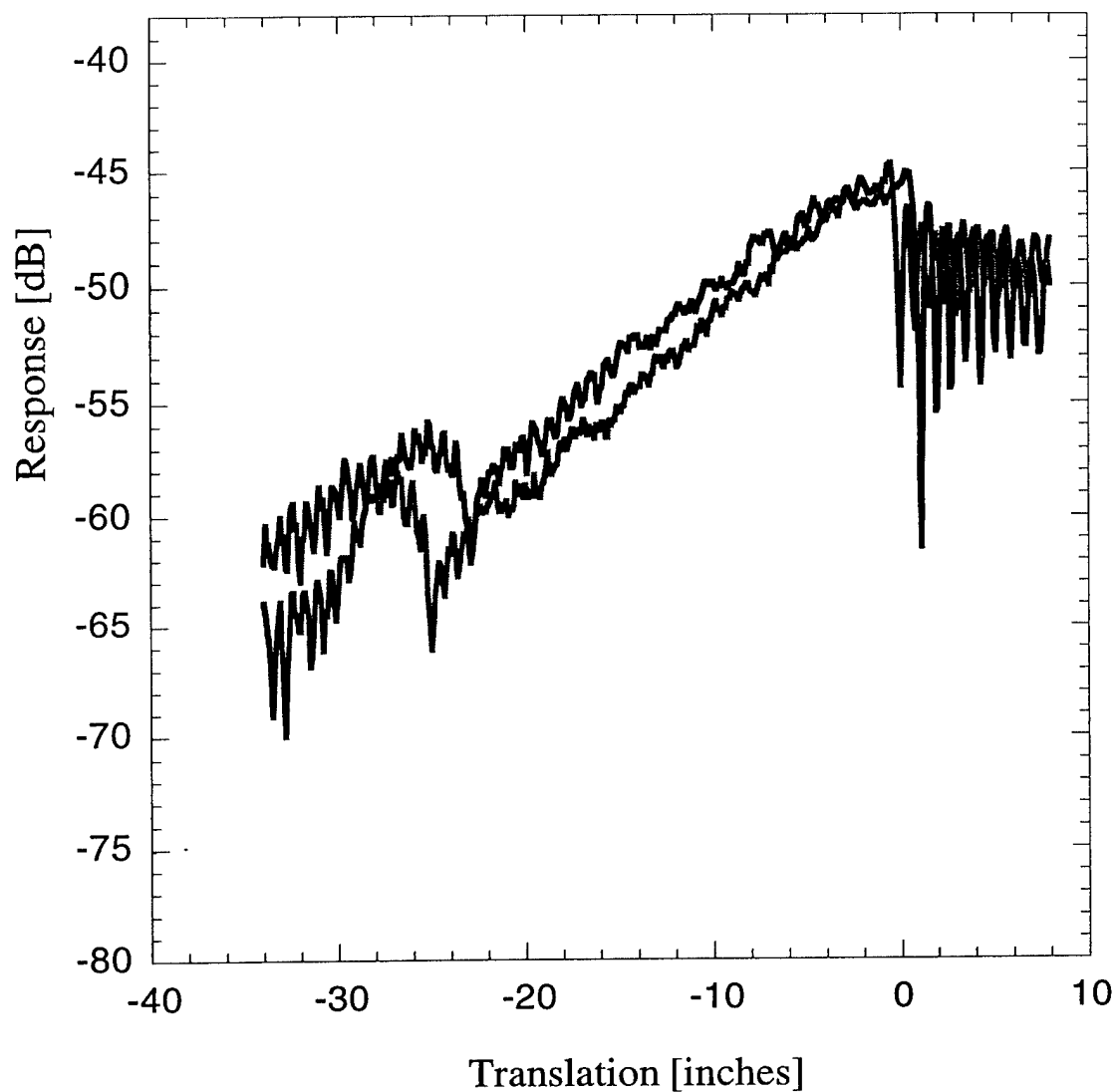


Figure 9: Comparison of the measured ultra-near electric fields for NSWCCD cubes with sharp (red) and rounded (blue) edges: bistatic TE polarized illumination at 10 GHz. Cube with the rounded edge has an edge radius of 0.25 in. (0.64 cm). Probe offset is 0.15 in. (0.38 cm).

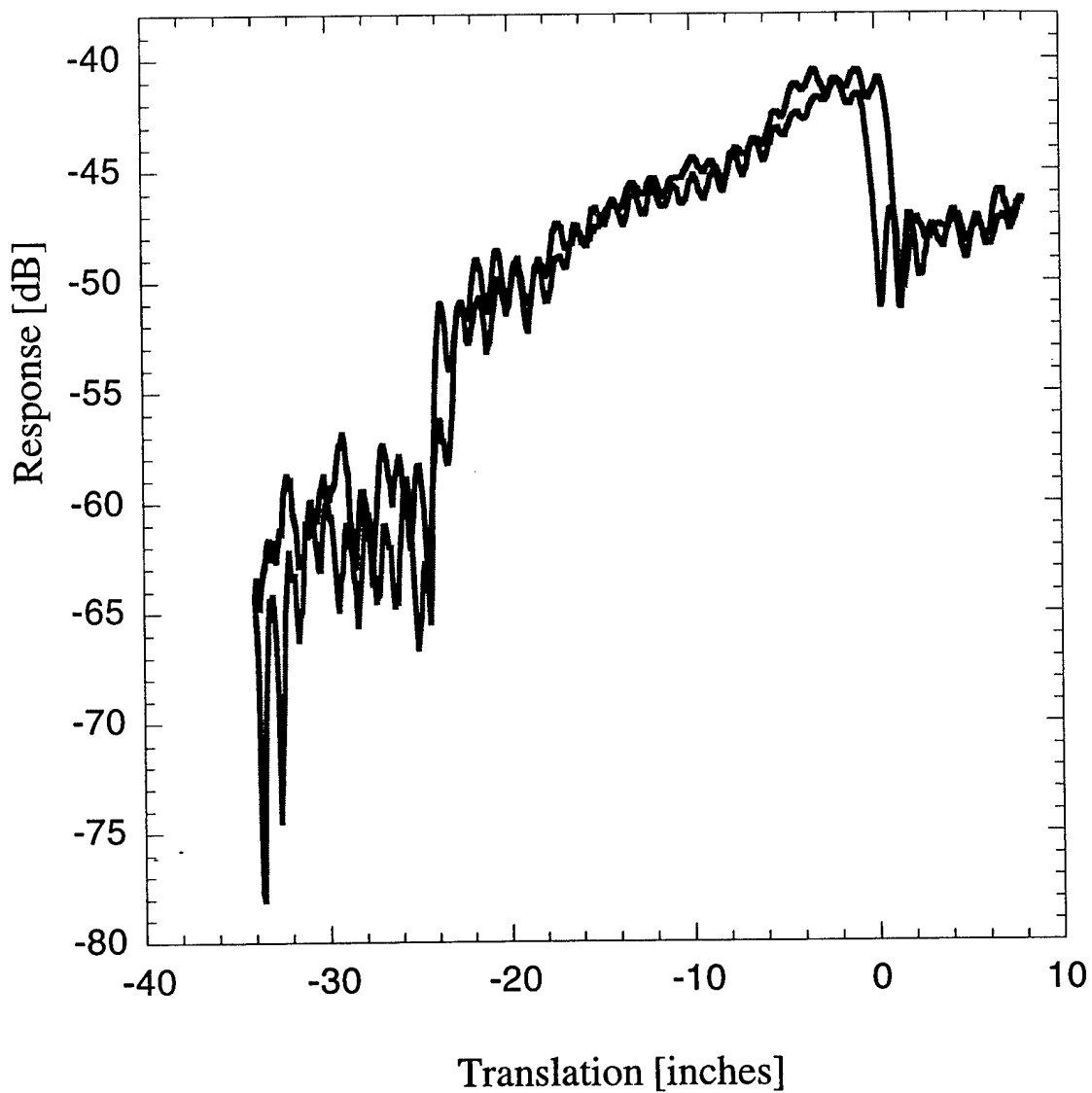


Figure 10: Comparison of the measured ultra-near electric fields for NSWCCD cubes with sharp (red) and rounded (blue) edges: bistatic TM polarized illumination at 6 GHz. Cube with the rounded edge has an edge radius of 0.25 in. (0.64 cm). Probe offset is 0.15 in. (0.38 cm).

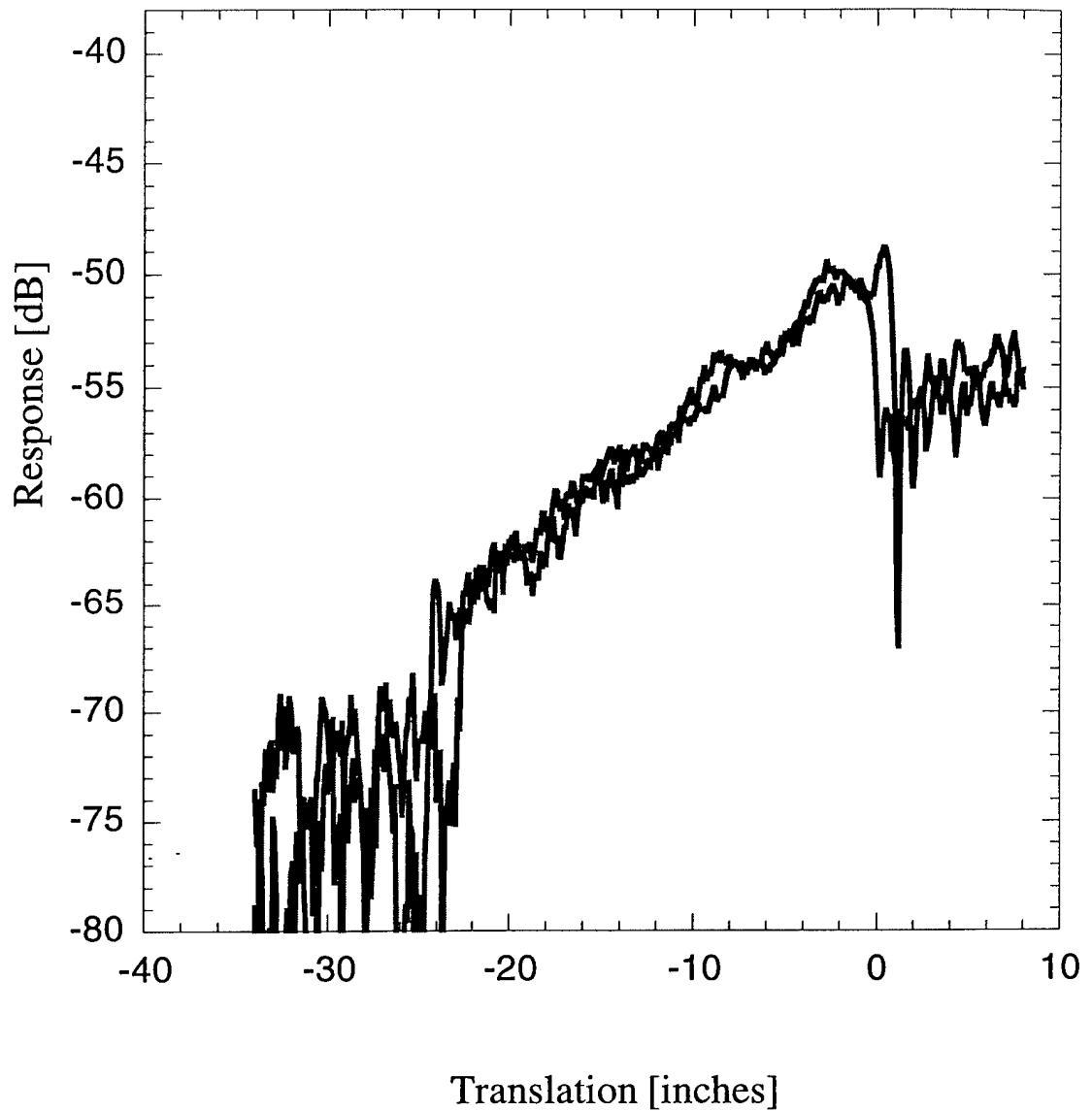


Figure 11: Comparison of the measured ultra-near electric fields for NSWCCD cubes with sharp (red) and rounded (blue) edges: bistatic TM polarized illumination at 10 GHz. Cube with the rounded edge has an edge radius of 0.25 in. (0.64 cm). Probe offset is 0.15 in. (0.38 cm).

### 3. THEORETICAL/ANALYTICAL INVESTIGATIONS

This phase of the effort focused on developing methods for calculating the ultra-near fields EM fields and  $\omega$ - $\kappa$  maps in the proximity of electrically large planar or curved 2-D surfaces. A special focus was the effect of edges and surface gaps. The principal scattering and diffraction mechanisms associated with ship topside structures such as masts and stacks can often be modeled at a specified angle of illumination and polarization in terms of such surfaces. To gain quantitative insights into the EM phenomena near such structures, a general unified formulation was developed based on the method of moments for bodies of translation (BOTs). With minor modifications, this formulation can be adapted to study the coupling and isolation of active or passive antenna elements on such surfaces. These applications are not discussed here.

For maximum generality, the BOTs considered here are either perfectly electrically conducting (p.e.c) or penetrable. A partially penetrable BOT is a subcase of the former. For the penetrable cases the surfaces may consist of multi-layered materials. Inclusions of periodic or non-periodic inclusions as in the case of frequency selective surfaces (FSS) are special cases. The materials can be dielectric or magnetic with complex permittivity and permeability. We begin with the simpler p.e.c. case, followed by the more general penetrable case.

#### 3.1. Formulation for p.e.c. BOTs: Case I

Representative formulations for BOTs based on the MM technique are given in [6-12]. The present formulation is adapted from [9]. Referring to Figure 12, the p.e.c. BOT surface is formed by translating the generating curve  $C(t)$  along the  $z$ -axis. The curve is parametrized by  $t$  and may have an arbitrary number of discontinuities as shown. The curve can be partially convex or concave, and either open or closed.

Assuming a time harmonic incident plane wave  $E^i$  ( $e^{j\omega t}$  is assumed), the total electric field  $E^t$  outside the body is:

$$\vec{E}^t = \vec{E}^i + \vec{E}^s \quad (1)$$

where the scattered field  $E^s = -L[J]$  and  $L[ ]$  is the integro-differential operator over the unknown surface currents  $J(t)$  on the BOT given by

$$\vec{E}^s = -L[\vec{J}] = -j\omega\mu_0 \int_{C(t)} dt' \left[ \vec{J} + \left( \frac{1}{\omega^2 \epsilon_0 \mu_0} \right) \nabla \nabla' \cdot \vec{J} \right] \Phi \quad (1a)$$

The integral is interpreted in the principal value sense. The 2-D free space Green's function kernel  $\Phi$  is given by

$$\Phi(kR) = \frac{1}{4j} H_0^{(2)}(kR) \quad R = \sqrt{(x-x')^2 + (y-y')^2} \quad (1b)$$

where  $H_0^{(2)}$  denotes the zeroth order Hankel function of the second kind;  $k=2\pi/\lambda$ , and  $\mu_0$  and  $\epsilon_0$  are the permeability and permittivity of free space, respectively. Noting that the total field on a perfect conductor vanishes, i.e.

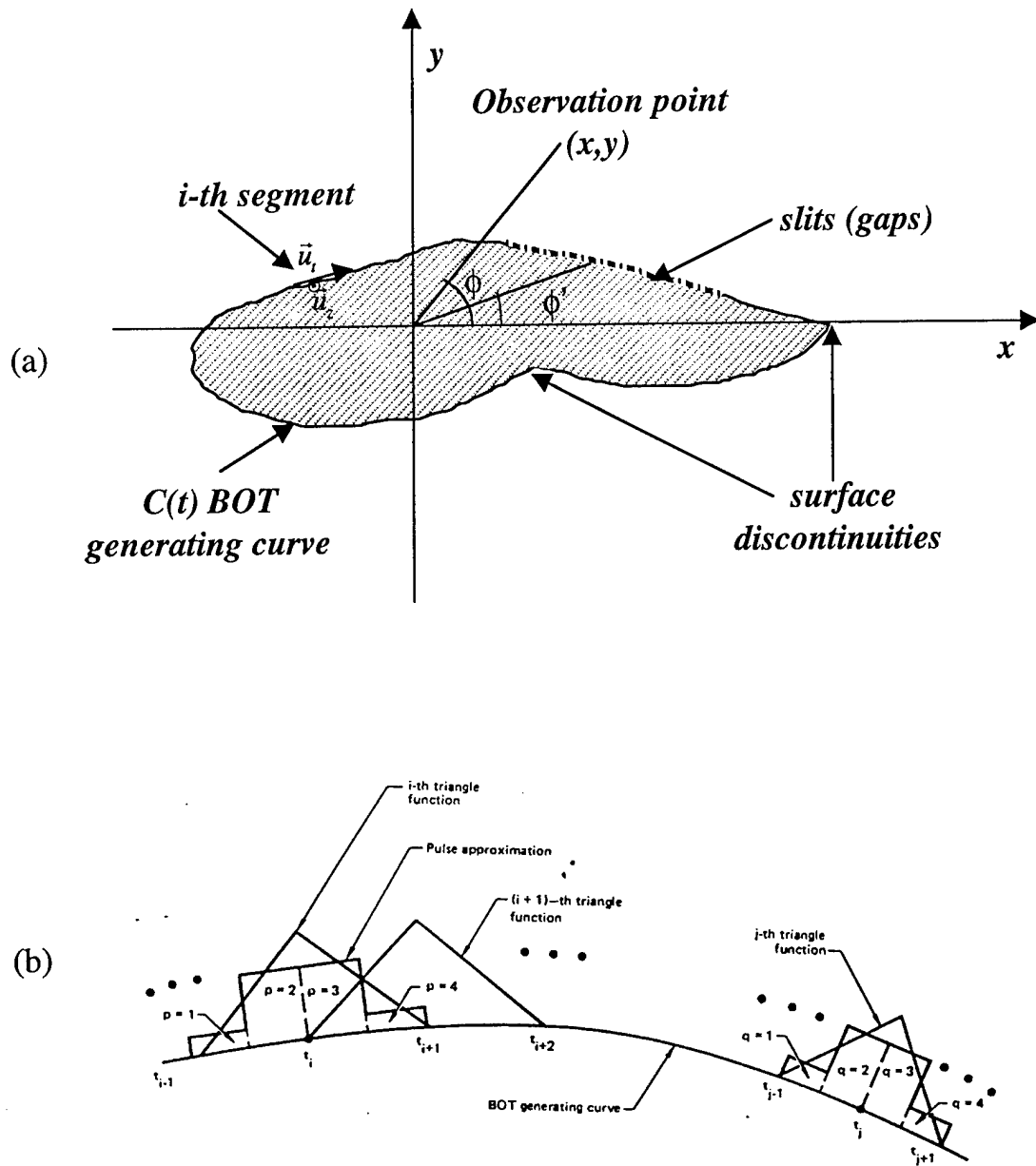


Figure 12: Generic p.e.c. body of translation. (a) coordinate geometry and (b) subdomain representation of the BOT generating curve used in the MM implementation.



$$\vec{E}_{\text{tan}}^i = L[\vec{J}]_{\text{tan}} \quad (2)$$

where the subscript denotes the tangential component on the BOT surface. Equation 2 is the well known electric field integral equation (EFIE). This equation can be solved for the unknown currents.

Since the focus of the present effort is on finite 2-D open or closed p.e.c surfaces with gaps, the issue of spurious solutions with the EFIE does not arise. If the surfaces are closed then one can use the Harrington-Mautz combined formulation to avoid these instabilities. In practice though, even for closed bodies the EFIE formulation is generally robust except where internal resonances occur. (For details see [6 - 12].)

If we apply the MM technique, the BOT generating curve  $C(t)$  is discretized into  $N$  sub-segments  $C_j$  parallel to the  $z$ -axis. The unknown surface currents on these segments are expanded as

$$\vec{J}(t) = \sum_j I_j^\alpha \vec{J}_j^\alpha \quad (3)$$

with  $\alpha = t$  for TE polarization and  $\alpha = z$  for TM polarization and where

$$\vec{J}_j^\alpha = \vec{u}_t f_j^\alpha(t) \quad (3a)$$

$\vec{u}_t$  is the tangent vector on  $C(t)$ , i.e.  $\vec{u}_t = \vec{u}_x \cos v' + \vec{u}_y \sin v'$  and  $v'$  is the angle subtended by the BOT generating curve and the  $x$ -axis. In the present formulation we let the discretized segments  $C_j$  be straight lines. The basis functions  $f_j(t)$  are chosen to be overlapping triangle functions spanning  $C_j$  (See Figure 12 b). They are defined as

$$f_j^\alpha(t) = \begin{cases} 1 - |t - t_j| & |t - t_j| \leq 1 \\ 0 & |t - t_j| > 1 \end{cases} \quad (3b)$$

A non-vanishing half-triangle at an edge of a gap discontinuity is chosen for  $f_j^z(t)$ . The TE and TM polarization denote the case where the incident electric field is perpendicular or parallel to the  $z$ -axis, respectively. (For alternate representations of currents on a BOT see [10] and [11].)

Following the usual MM (Galerkin) procedure, the current expansions in Eq. 3 are substituted into Eq. 2 to form the inner products of the integral operator  $L[\ ]$  with the testing functions  $\vec{W}^\alpha (= \vec{J}^{\alpha*})$ . The asterisk denotes the conjugate operation. This yields a system of algebraic equations for the unknown current expansion coefficients  $I_j^\alpha$ :

$$\sum_j Z_{ij}^{\alpha\alpha} I_j^\alpha = V_i^\alpha \quad i = 1, 2, \dots, N \quad \alpha = t \text{ or } z, t \in C(t) \quad (4)$$

where

$$Z_{ij}^{\alpha\alpha} = \langle \vec{W}_i^\alpha, L[\vec{J}_j^\alpha] \rangle \quad (4a)$$

and where  $\vec{W}_i^\alpha$  and  $\vec{J}_j^\alpha$  are the i-th testing and j-th current basis functions on  $C(t)$ , respectively. The term  $V_i^\alpha$  is the incident electric field tested on the BOT segment spanning the i-th triangle function, i.e.

$$V_i^\alpha = \langle \vec{W}_i^\alpha, \vec{E}_{\text{tan}}^i \rangle \quad (4b)$$

For ease of reference and completeness, the defining expressions for the Z's and V's in Eq. 4 are given in Appendix A adapted from [9]. The unknown current coefficients in Eq. 4 are obtained using standard matrix solution methods.

### 3.2. $\omega$ - $\kappa$ Transformation for Case I

Knowing the MM derived currents, we carry out the Fourier transform directly on the scattered electric field given by the L [J] operator in Eq. 1a. Formally, the transformed electric field over  $x$  for the propagation constant  $k_x$  is given by:

$$\begin{aligned} \vec{\mathcal{E}}^s(k_x, y) &= \int_{-\infty}^{\infty} \vec{E}^s(x, y) e^{jk_x x} dx \\ &= -j\omega\mu_0 \int_{C(t)} dt' \vec{J}A - \frac{j}{\omega\epsilon_0} \int_{C(t)} dt' (\nabla' \cdot \vec{J}) \vec{B} \end{aligned} \quad (5)$$

where

$$A = \frac{1}{4j} \int_{-\infty}^{\infty} H_0^{(2)}(kR) e^{jk_x x} dx \quad (5a)$$

and

$$\vec{B} = \nabla A \quad (5b)$$

In the foregoing the implicit assumption is made that the interchange of the order of integrations (i.e. over  $x$  and  $t$ ) does not affect the value of the result. This is justified by the convergence of the reordered infinite integral over  $x$ . The transform in Eq. 5 can be carried out analytically. Considering the  $A$  (vector potential) term,

$$A = \frac{1}{4j} e^{jk_x x'} \int_{-\infty}^{\infty} H_0^{(2)}(k\bar{R}) (\cos k_x \bar{x} + j \sin k_x \bar{x}) d\bar{x} \quad \bar{R} = \sqrt{\bar{x}^2 + \bar{y}^2} \quad (6)$$

where  $\bar{R}$  is defined in terms of the shifted coordinates  $\bar{x} = x - x'$  and  $\bar{y} = y - y'$ . The integrand with the sine term is odd and hence its contribution is zero, thus yielding

$$A = \frac{1}{2j} e^{jk_x x'} \int_0^{\infty} H_0^{(2)}(k\bar{R}) \cos k_x \bar{x} d\bar{x} \quad (7)$$

Expressing the Hankel function in terms of the zeroth order Bessel and Neumann functions, i.e.  $H_0^{(2)} = J_0 - j N_0$  and invoking the integral identities [13], we obtain for  $y > 0$ ,

$$A = \frac{1}{2j} e^{jk_x x'} \begin{cases} \frac{1}{K_1} e^{-jK_1 \bar{y}} & 0 < k_x < k_1 \\ \frac{j}{K_x} e^{-K_x \bar{y}} & 0 < k_1 < k_x \end{cases} \quad (8)$$

where  $K_1 = \{k_1^2 - k_x^2\}^{1/2}$  and  $K_x = \{k_x^2 - k_1^2\}^{1/2}$ . Explicitly written, the  $\bar{B}$  (scalar potential) term is

$$\bar{B} = \bar{u}_x \frac{1}{4j} e^{jk_x x'} \int_{-\infty}^{\infty} \frac{\partial H_0^{(2)}(k\bar{R})}{\partial \bar{x}} e^{jk_x \bar{x}} d\bar{x} + \bar{u}_y \frac{\partial A}{\partial \bar{y}} \quad (9)$$

For the first part of Eq. 9 we invoke the theorem in [14]. For the second part we use the result in Eq. 7, yielding

$$\bar{B} = -\frac{1}{2} e^{jk_x x'} \begin{cases} \left( \bar{u}_x \frac{k_x}{K_1} + \bar{u}_y \right) e^{-jK_1 \bar{y}} & 0 < k_x < k_1 \\ \left( \bar{u}_x j \frac{k_x}{K_x} + \bar{u}_y \right) e^{-K_x \bar{y}} & 0 < k_1 < k_x \end{cases} \quad (10)$$

The terms in Eqs. 8 and 10 with the imaginary exponential represent the propagating parts of  $A$  and  $\bar{B}$ , respectively. The others denote the evanescent parts. (To obtain corresponding results for the  $\omega$ - $k_y$  domain, one substitutes  $k_y$  for  $k_x$  and  $y$  for  $x$  in the above expressions.)

The transformed electric field in Eq. 5 can be evaluated numerically using the Galerkin discretization used earlier on the  $L[\ ]$  operator in computing the impedance elements in Eq. 4. Using the current coefficients obtained from the solution of Eq. 4 we obtain the desired expressions for the transformed fields for the respective polarizations as:

$$\begin{aligned} \vec{\mathcal{E}}_{TE}(k_x, y) = j\omega\mu_0 \sum_j I_j^t \int_{C_j} dt' \left\{ \bar{u}_t' f_j'(t') A_j \right. \\ \left. + \frac{j}{\omega\epsilon_0} \left( \frac{1}{y_j} \sin v_j f_j'(t') + \frac{df_j'(t')}{dt'} \right) \bar{B}_j \right\} \end{aligned} \quad (11)$$

and

$$\vec{\mathcal{E}}_{TM}(k_x, y) = j\omega\mu_0 \bar{u}_z \sum_j I_j^z \int_{C_j} dt' f_j^z(t') A_j \quad (12)$$

Note the summation of the integrals in the above expressions is over the discretized BOT segments  $C_j$ , spanned by the  $j$ -th triangle function  $f_j^\alpha(t)$ . The terms  $A_j$  and  $\bar{B}_j$  are the discretized forms of  $A$  and  $\bar{B}$  in Eq. 8 and 10, respectively, where  $x' \rightarrow x_j$  and  $y' \rightarrow y_j$ , and the angle  $v' \rightarrow v_j$  in the sine and cosine terms. The numerical integrations in Eqs. 11 and 12 can be performed by standard methods such as the Simpson rule or Gaussian quadrature.

### 3.3. Formulation for Penetrable BOTs: Case II

The MM solution for penetrable composite laminate planar strips is summarized in [15]. Such laminates are a subcase of BOTs. The present formulation extends the foregoing results for arbitrary penetrable BOTs. Representative BOT configurations addressed here are depicted in Figure 13. As detailed in [15], the MM based solution proceeds by solving a system of equations that arise from the electric and magnetic boundary conditions between the various regions. The resulting solution gives the surface currents on the boundaries between the various regions. In all the cases shown in Figure 13, the surface currents on the outermost boundary are explicitly expressed in terms of the currents on the interior boundaries. Using these external currents, the external fields are then computed. Since we are interested only in the external fields, the simplest penetrable case (i.e. Figure 13a) is the starting point of our discussion.

As shown in Figure 13a, the outermost surface of the BOT scatterer is again defined by the generating curve  $C(t)$  translated along the  $z$ -axis. As before, the curve is parameterized by  $t$  and can be partially convex or concave. Penetrable BOTs of multiple disconnected regions are special cases of the foregoing. Since they do not pose new technical difficulties but only add notational complexity, for sake of brevity we omit their discussion here. The implementing numerical expressions to be programmed include this generalization.

Given a time harmonic incident plane wave  $\vec{E}^i, \vec{H}^i$  ( $e^{j\omega t}$  is assumed), the total electric and magnetic fields outside an arbitrary penetrable scatterer (region 1) are given by the sum of the incident and scattered fields, i.e.

$$\vec{E}^t = \vec{E}^i + \vec{E}^s \quad (13)$$

$$\vec{H}^t = \vec{H}^i + \vec{H}^s \quad (14)$$

where the fields are implicitly functions of  $(x, y)$  and the scattered fields are given by

$$\vec{E}^s = -L_1 \vec{J}_1 + K_1 \vec{M}_1 \quad (15)$$

$$\vec{H}^s = -K_1 \vec{J}_1 - \frac{1}{\eta_1^2} L_1 \vec{M}_1 \quad (16)$$

and  $\eta_1 = \sqrt{(\mu_1/\epsilon_1)}$ , and  $\mu_1$  and  $\epsilon_1$  are the permeability and permittivity of region  $R_1$ , respectively. These can be and generally are complex quantities. If this region is free space then  $\mu_1 = \mu_0$  and  $\epsilon_1 = \epsilon_0$ . The coupled equations above define the surface electric and magnetic current densities,  $\vec{J}_1$  and  $\vec{M}_1$  which are functions of  $t$ , the parametrization variable. The  $L_1$  and  $K_1$  terms are integro-differential operators and defined for a vector quantity  $\vec{X}(t)$  representing either the electric or magnetic surface currents, i.e.

$$L_1 \vec{X}(t) = j\omega\mu_1 \int_{C(t)} \left[ \vec{X}(t) + \frac{1}{\omega^2 \mu_1 \epsilon_1} \nabla \nabla' \cdot \vec{X}(t) \right] \Phi(k_1 R) dt' \quad (17)$$

$$K_1 \vec{X}(t) = j\omega\mu_1 \int_{C(t)} \vec{X}(t) \times \nabla \Phi(k_1 R) dt' \quad (18)$$

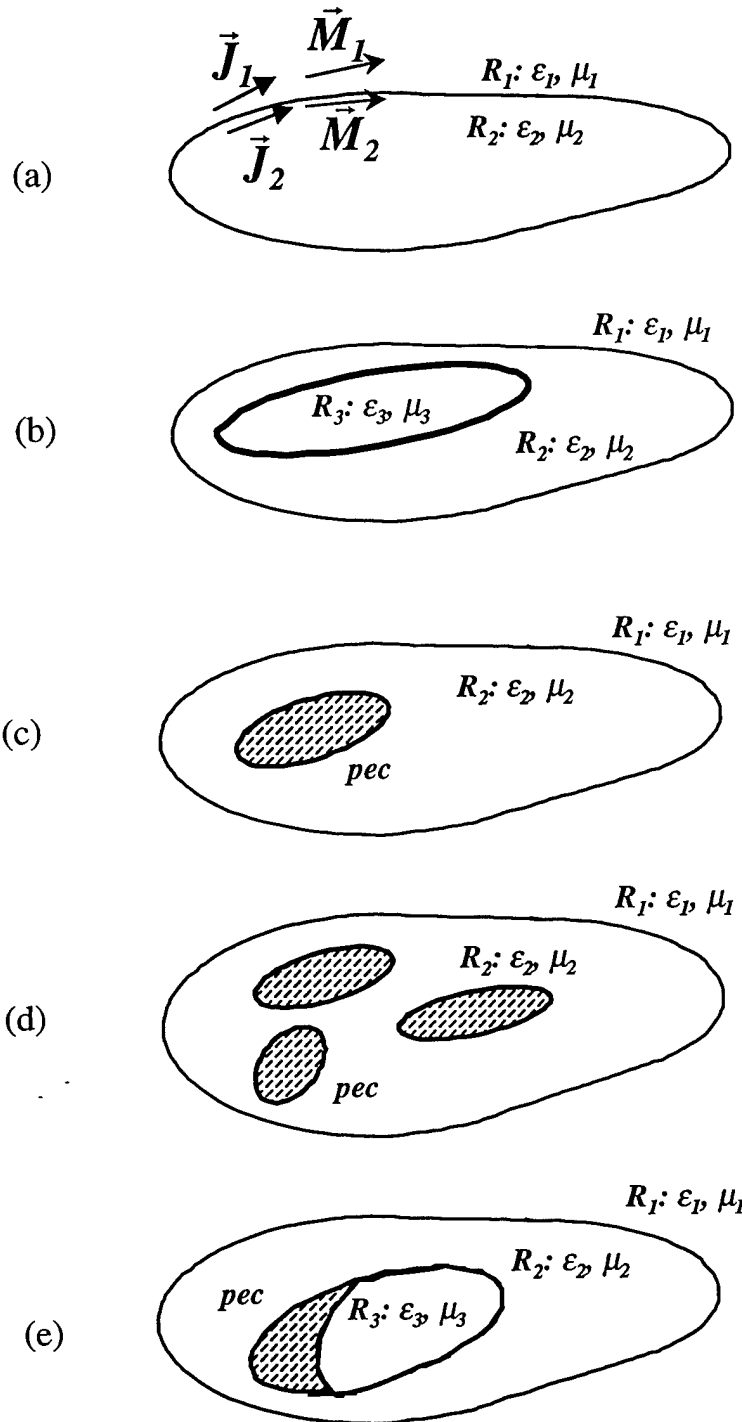


Figure 13: Hierarchy of general penetrable bodies of translation: (a) homogeneous internal region, (b) layered multiple homogeneous internal regions, (c) homogeneous internal region with p.e.c. inclusion, (d) homogeneous region with discrete p.e.c. inclusions, (e) homogeneous region with inhomogeneous inclusions

To specialize these operators to a BOT, for the external region  $R_1$  again the 2-D free space Green's function is used, i.e.

$$\Phi(k_1 R) = \frac{1}{4j} H_0^{(2)}(k_1 R) \quad R = [(x - x')^2 + (y - y')^2]^{1/2} \quad (19)$$

where  $k_1 = 2\pi/\lambda$ . For the internal region  $R_2$ , the electric and magnetic fields are given by:

$$\vec{E}' = -L_2 \vec{J}_2 + K_2 \vec{M}_2 \quad (20)$$

$$\vec{H}' = -K_2 \vec{J}_2 - \frac{1}{\eta_2^2} \epsilon_2 \vec{M}_2 \quad (21)$$

where the subscripts are associated with region  $R_2$ . The Green's function is defined over the wave number of this region. Imposing the continuity of the tangential electric and magnetic fields on the boundary of the scatterer and noting that  $\vec{J}_1 = -\vec{J}_2$  and  $\vec{M}_1 = -\vec{M}_2$ , yields the following coupled system of equations for the electric and magnetic currents:

$$\vec{E}'|_{\text{tan}} = \{(L_1 + L_2)\vec{J}_1 - (K_1 + K_2)\vec{M}_1\}|_{\text{tan}} \quad (22)$$

$$\vec{H}'|_{\text{tan}} = \{(K_1 + K_2)\vec{J}_1 + \left(\frac{1}{\eta_1^2} L_1 + \frac{1}{\eta_2^2} L_2\right)\vec{M}_1\}|_{\text{tan}} \quad (23)$$

Equations 22 and 23 are solved by the usual MM procedure. As before the generating curve  $C(t)$  is discretized by straight line segments. The unknown currents are next expanded in a finite set of basis functions weighted by unknown coefficients on each of these segments. Specifically for TE polarization, the electric and magnetic surface currents are

$$\vec{J}_1 = \vec{u}_t J^t \quad (24a)$$

$$\vec{M}_1 = \vec{u}_z M^z \quad (24b)$$

and similarly for TM polarization,

$$\vec{J}_1 = \vec{u}_z J^z \quad (24c)$$

$$\vec{M}_1 = \vec{u}_t M^t \quad (24d)$$

where

$$\left. \begin{matrix} J^\alpha \\ M^\alpha \end{matrix} \right\} = \sum_j \left\{ \begin{matrix} a_j^\alpha \\ b_j^\alpha \end{matrix} \right\} f_j^\alpha(t)$$

and

$$f_j^\alpha(t) = \begin{cases} 1 - |t - t_j| & |t - t_j| \leq 1 \\ 0 & |t - t_j| > 1 \end{cases}$$

where  $f_i^\alpha(t)$  are again chosen as overlapping triangle functions defined earlier and spanning the discretized segments of  $C(t)$  with tangent vector  $\vec{u}_i$ . Further details of the MM (Galerkin) solution process are given in [15]. Using the convention from Case I, the TE and TM polarization denote the case where the incident electric field is perpendicular or parallel to the z-axis, respectively. Knowing the surface currents, the external fields can be obtained at any point  $(x,y)$  and are given explicitly in terms of the L and K operators in Eqs.17 and 18.

### 3.4. $\omega$ - $\kappa$ Transformation for Case II

To obtain the  $\omega$ - $\kappa$  representation, we Fourier transform the scattered fields along a propagation direction. If this direction is along the x-axis, the transform is over  $k_x$ , i.e.

$$\begin{aligned}\vec{\mathcal{E}}^s(k_x, y) &= \int_{-\infty}^{\infty} \vec{E}^s(x, y) e^{jk_x x} dx \\ &= -\tilde{L} \vec{J} + \tilde{K} \vec{M}\end{aligned}\quad (25a)$$

$$\begin{aligned}\vec{\mathcal{H}}^s(k_x, y) &= \int_{-\infty}^{\infty} \vec{H}^s(x, y) e^{jk_x x} dx \\ &= -\tilde{K} \vec{J} - \frac{1}{\eta_0^2} \tilde{L} \vec{M}\end{aligned}\quad (25b)$$

where  $\tilde{L}$  and  $\tilde{K}$  are the Fourier transforms of  $L$  and  $K$ , respectively, formally they are given by

$$\left. \begin{array}{l} \tilde{L}\vec{X} \\ \tilde{K}\vec{X} \end{array} \right\} = \int_{-\infty}^{\infty} \left\{ \begin{array}{l} L \\ K \end{array} \right\} \vec{X}(t) e^{jk_x x} dx \quad (26)$$

For simplicity we have dropped the subscripts in the foregoing expressions. The transforms of the L and K operators are derived in Appendix A. For TE polarization, the scattered fields in the  $\omega$ - $\kappa$  domain for any surface  $y = \text{constant}$  are:

$$\vec{\mathcal{E}}_{\text{TE}}^s(k_x, y) = -j\omega\mu_0 \int_{C(t)} dt' \vec{u}_i J'(t') A - \frac{j}{\omega\epsilon_0} \int_{C(t)} dt' (\nabla' \cdot \vec{u}_i J') \vec{B} + \int_{C(t)} dt' M^z(t') \vec{B}_1 \quad (27a)$$

$$\vec{\mathcal{H}}_{\text{TE}}^s(k_x, y) = - \int_{C(t)} dt' J'(t') \vec{B}_2 - \frac{j\omega\mu_0}{\eta_0^2} \int_{C(t)} dt' \vec{u}_i M^z(t') A \quad (27b)$$

For TM polarization, the corresponding expressions are:

$$\vec{\mathcal{E}}_{\text{TM}}^s(k_x, y) = -j\omega\mu \int_{C(t)} dt' \vec{u}_z J^z(t') A + \int_{C(t)} dt' M^t(t') \vec{B}_2 \quad (28a)$$

$$\tilde{\mathcal{H}}_{\text{TM}}^s(\mathbf{k}_x, y) = -\int_{C(t)} dt J^z \tilde{B}_1 - \frac{j\omega\mu_0}{\eta_0^2} \int_{C(t)} dt \tilde{u}_t M'(t') A - \frac{j}{\omega\epsilon_0\eta_0^2} \int_{C(t)} dt (\nabla' \cdot \tilde{u}_t M') \tilde{B} \quad (28b)$$

The TE and TM cases are duals of each other. The expressions for  $A$ ,  $\tilde{B}$ ,  $\tilde{B}_1$ , and  $\tilde{B}_2$  are given in Appendix A.

The expressions for the transformed fields are evaluated numerically by substituting the expansions for  $\tilde{J}_1(t)$  and  $\tilde{M}_1(t)$  from Eq. 24 where the coefficients  $a_j$  and  $b_j$  are determined from the MM solution of Eqs. 22 and 23. For example, Eq. 27b becomes:

$$\tilde{\mathcal{H}}_{\text{TE}}^s(\mathbf{k}_x, y) = -\sum_j a_j' \int_{C_j} dt f_j'(t') \tilde{B}_{2j} - \tilde{u}_z \frac{j\omega\mu_0}{\eta_0^2} \sum_j b_j^z \int_{C_j} dt f_j^z(t') A_j \quad (29)$$

and similarly for the other fields given in Eqs. 27 and 28. The remaining integrations over  $t$  become a sum of integrals over each segment  $C_j$  of the BOT generating curve  $C(t)$ . As before, they are evaluated by standard numerical techniques such as a Simpson method or a Gaussian quadrature.



#### 4. NUMERICAL RESULTS

The  $\omega$ - $\kappa$  formulation for p.e.c. BOTs was numerically implemented by modifying the CARLOS code. This code is a general purpose electromagnetics code based on the MM technique for solving complex 2-D and 3-D scattering problems. [16,17] The code has a number of options for discretization of the unknowns in the underlying integro-differential equations. We restricted ourselves here to the Galerkin option using compact support functions, i.e. overlapping triangle functions. This provides the needed flexibility to handle a broad range of surface and material discontinuities and gaps. These can be large or small compared to the wavelength.

Using the computational engine in CARLOS, the surface currents are computed at a given frequency, illumination angle and polarization. Using these currents, the fields can then be computed everywhere: either in the far field (Frauenhofer region) yielding the monostatic and bistatic RCS or in the proximity of the body (Fresnel region or closer.)

Previously, the computational algorithms embedded in CARLOS have been validated extensively for a variety of targets subject to monostatic and bistatic illumination. The remaining validation involved the algorithms used in computing the  $\omega$ - $\kappa$  representation of the fields. This validation involved calculating the near or ultra-near fields by two totally different methods. In one approach, designated here as the indirect method, the near fields in the vicinity of a target were computed numerically at a finite set of spatial points. These were then FFT to the  $\omega$ - $\kappa$  domain. Since the near field sample was finite, the truncation of the spatial data along the propagation direction could lead to significant errors in the  $\omega$ - $\kappa$  results unless a very large spatial sample was used. In addition to the errors incurred, the computational resources (time and memory) required with the indirect approach in numerical simulations were considerable.

The alternate, direct approach was discussed in the preceding sections. The currents on the targets were obtained using the MM technique as outlined for Case I and II. Next the scattered fields expressed in operator form were Fourier transformed analytically over the spatial domain along the desired propagation direction. The resulting transformed fields were mapped directly into the  $\omega$ - $\kappa$  space delineating the propagating and evanescent field components in the proximity of the target.

The  $\omega$ - $\kappa$  results obtained by both methods were compared. The convergence of the solutions and the computed ultra-near fields were investigated as a function of the Galerkin discretization. For the indirect method the set of field sampling points was also varied and various smoothing functions were introduced to minimize the truncation effects. The computational resource requirements with the direct method were found to be significantly less when compared with the earlier indirect method without loss of accuracy.

The direct and indirect methods were applied to two classes of generic targets: p.e.c. strips and dihedrals with and without gaps. As a subcase of the latter, dihedrals with right angle and rounded corners were also considered.

Figure 14 compares the calculated scattered fields from a strip lying on the x-axis, having a width  $w = 18$  inches (45.72 cm) with and without a bisecting gap. The fields are sampled at  $y = 0.1$  inches (0.254 cm). The strip is illuminated bistatically at  $\phi = 167^\circ$  measured

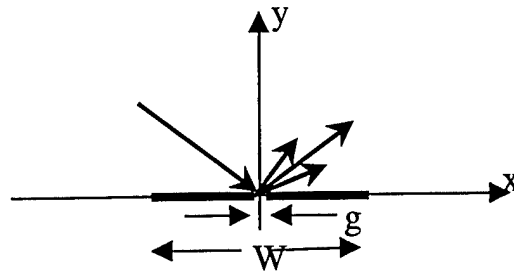
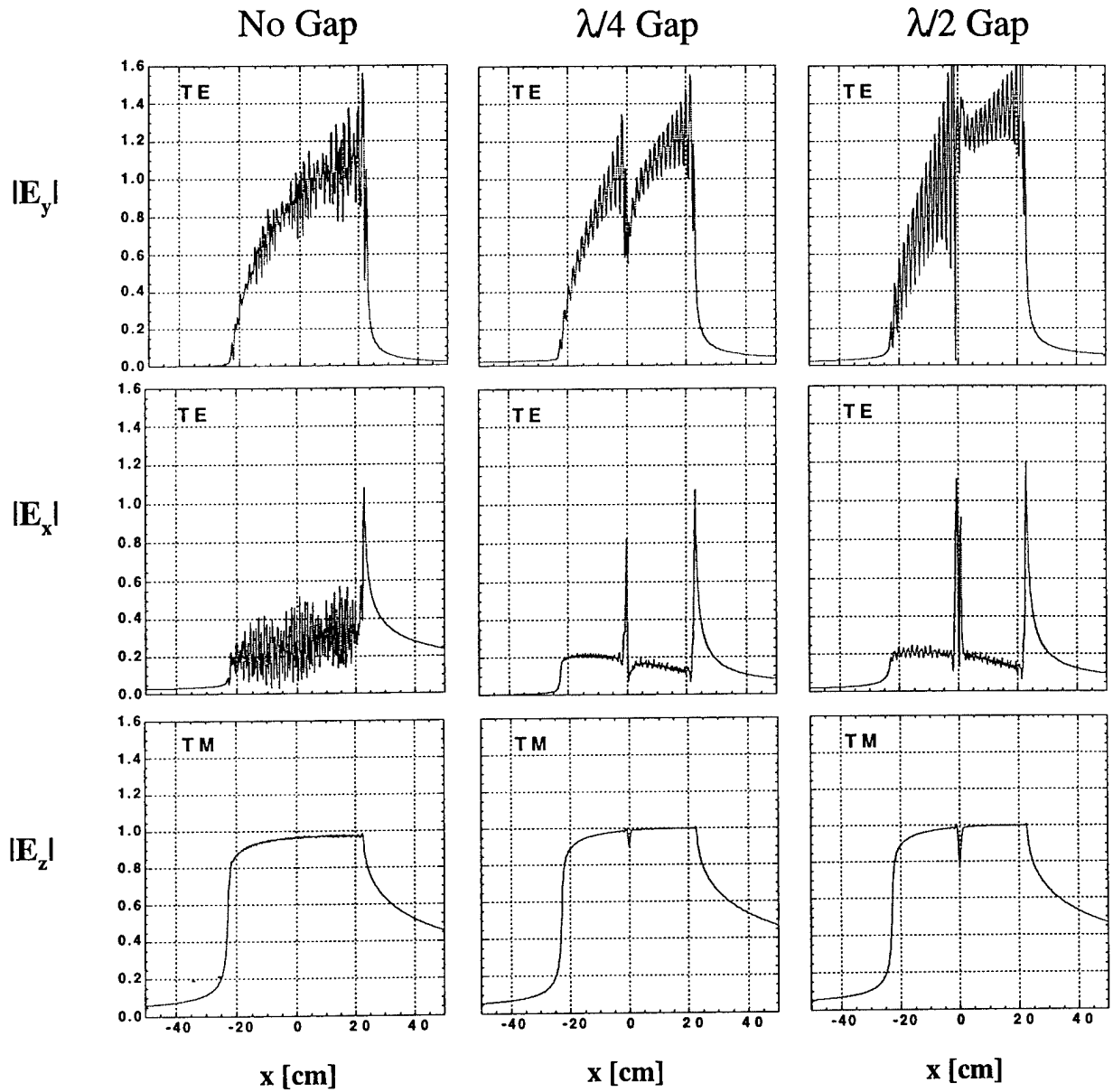


Figure 14: Computed ultra-near fields from a p.e.c. strip with and without gaps illuminated at  $\phi_1 = 167^\circ$ . The strip width ( $w$ ) is 18 in. (45.72 cm). The gap width ( $g$ ) is referenced to 10 GHz. The fields are sampled along  $y = 0.1$  in. (0.254 cm) from the strip surface.

from the x-axis. This angle approximates the Peter's lobe angle, i.e.  $\phi := \sqrt{(w/\lambda)}$  at 10 GHz where the maximum traveling wave scattering occurs for slender electrically extended bodies. [18] The corresponding  $\omega$ - $\kappa$  maps for these cases are given in Figure 15. For the y- and z- polarized fields, these maps show a prominent V-shaped feature. The region within the V constitutes the propagating region. The region outside is the evanescent region. The line sloping to the right denotes the forward scattered field intensities. Since this line is approximately coincident with the "light" line having a slope of  $c/2\pi$  ( $c$  = speed of light) the forward scattered fields are propagating with a velocity nearly  $c$ . The line sloping to the left is the mirror image of the former. It is associated with the back-scattered fields propagating in the negative  $x$  direction with a velocity nearly  $c$ . The back-scattered fields are shown to be much weaker. Notably the gap in the strip suppresses additional secondary propagating fields within the V region. For the x-polarized fields, the backscattered fields are vanishingly small.

To correlate with the strip results, near field measurements were carried out using the metal plate described earlier. These are depicted in Figure 16. As before, the forward scattered field intensities are coincident with the light line. The variation in the forward scattered field intensity along the light line is an experimental artifact. It arises from quasi-resonant probe interactions with the plate. Similarly, the line in the evanescent region with a slope of approximately  $c/\pi$  is a probe induced effect. As noted with the computed results in Figure 14, the backscattered fields are much weaker. Consequently, these were difficult to resolve experimentally.

Furthermore, the depolarization of the fields evident in the case of the plate, but not present in the strip, also tends to mask the detailed structure of the backscattered fields. The same comments apply to the fine details seen in the computed secondary propagating and evanescent fields for the strip but missing in the measured results for the plate.

Figure 17 shows the corresponding computed results for a strip without gaps, illuminated at broadside and oblique angles. For the x- and z-polarized cases, the dominant field intensities occur at  $k_x = 0$ , indicative of broadside backscattering. For the y- and z-polarized cases the finite width of the strip also results in weak forward and backscattered fields even at broadside. Finally, we note that for  $\phi = 135^\circ$ , the dominant forward scattered (reflected) field intensity occurs at  $k_x = k \cos(\phi - 135^\circ)$  in conformance with Snell's law of reflection. Because of the finiteness of the strip width, the intensities are spread over a number of  $k_x$  values corresponding to edge diffraction from the strip.

Figure 18 compares the computed  $\omega$ - $\kappa$  maps for a dihedral where one of its sides has a bisecting gap. Two cases are shown. In one, the gap is in the illuminated region; in the other it is shadowed. For the latter case, there appears to be a band of destructive interference in both the forward and backscattered fields, centered approximately at 7 and 15 GHz. In both cases the dominant scattering occurs at the speed of light propagation velocity along the width of the strip.

Figure 19 compares the computed  $\omega$ - $\kappa$  maps for a right angle dihedrals with sharp and rounded corners. In both cases the gaps are in the shadowed region. There is destructive interference in both cases. This is most pronounced for the x-polarized fields propagating along the strip. In the case of the y-polarized fields, the major differences are observed in the backscattered evanescent fields near the target.

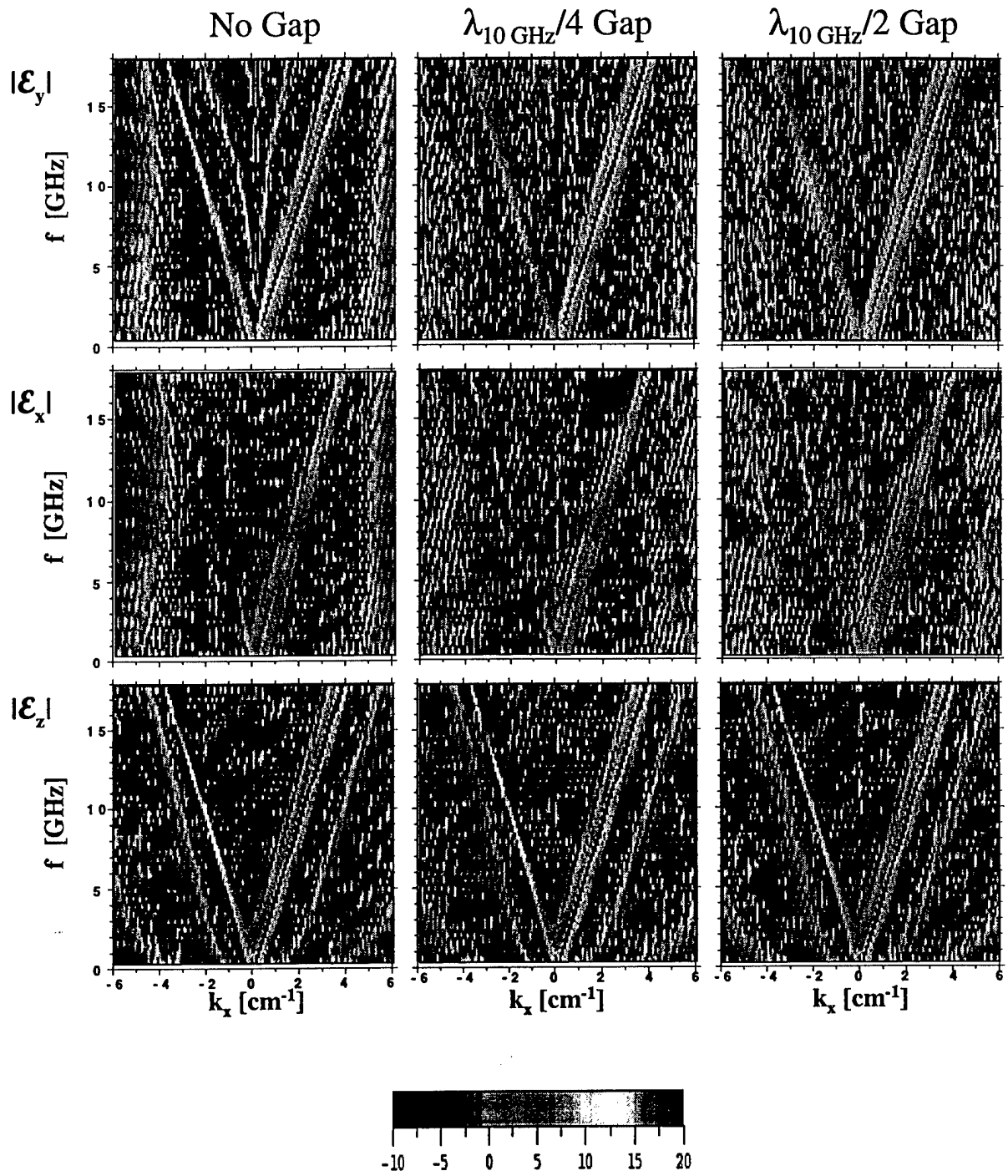


Figure 15: Computed  $\omega$ - $\kappa$  representations for a p.e.c. strip with and without gaps, illuminated at  $\phi_1 = 167^\circ$ . The gap widths are referenced to 10 GHz. The strip width and the field sampling are as in Figure 14.

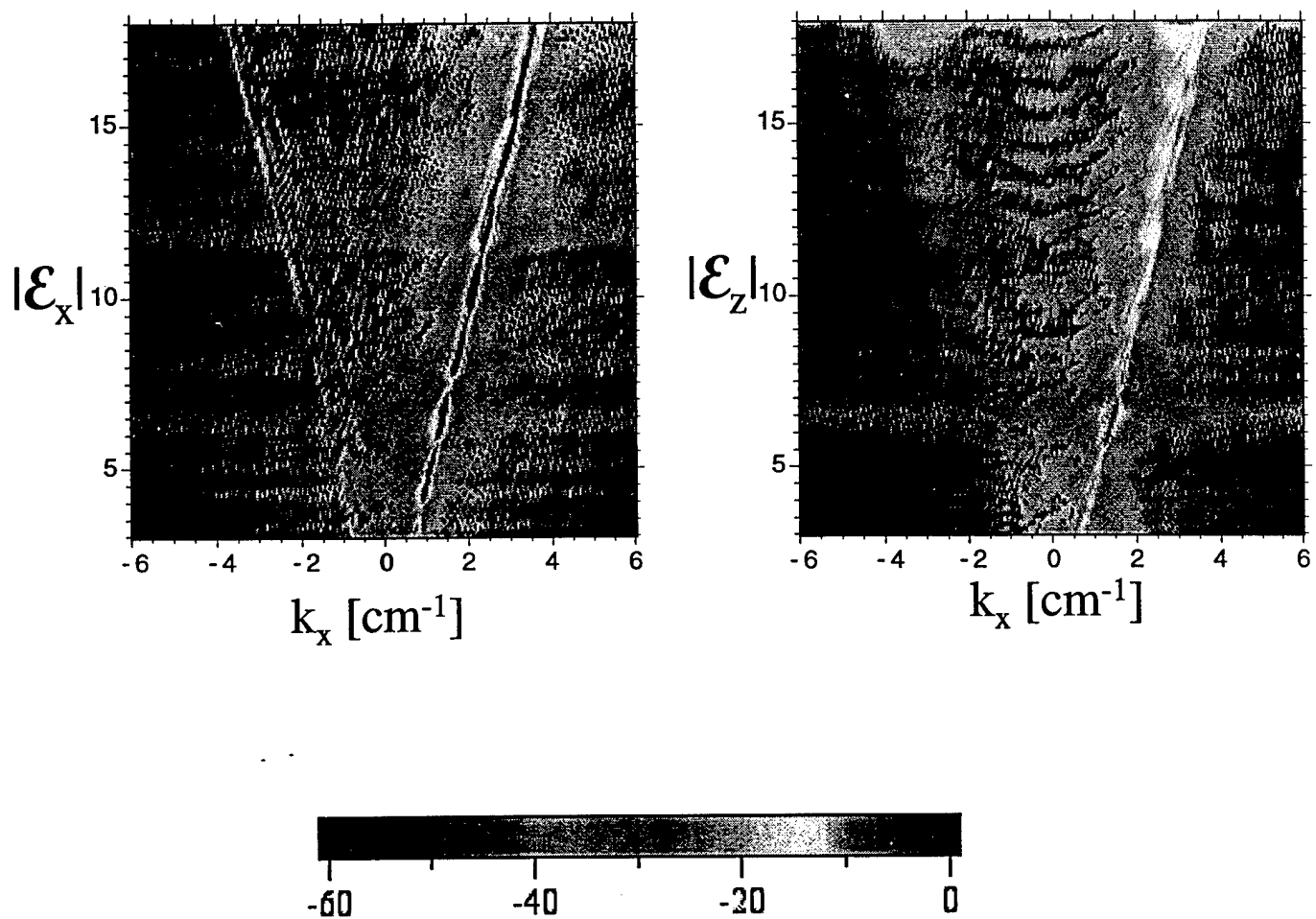


Figure 16: Measured  $\omega$ - $\kappa$  representations for a p.e.c. strip without a gap, illuminated at  $\phi_I = 167^\circ$ . The strip width and the field sampling are as in Figure 14.

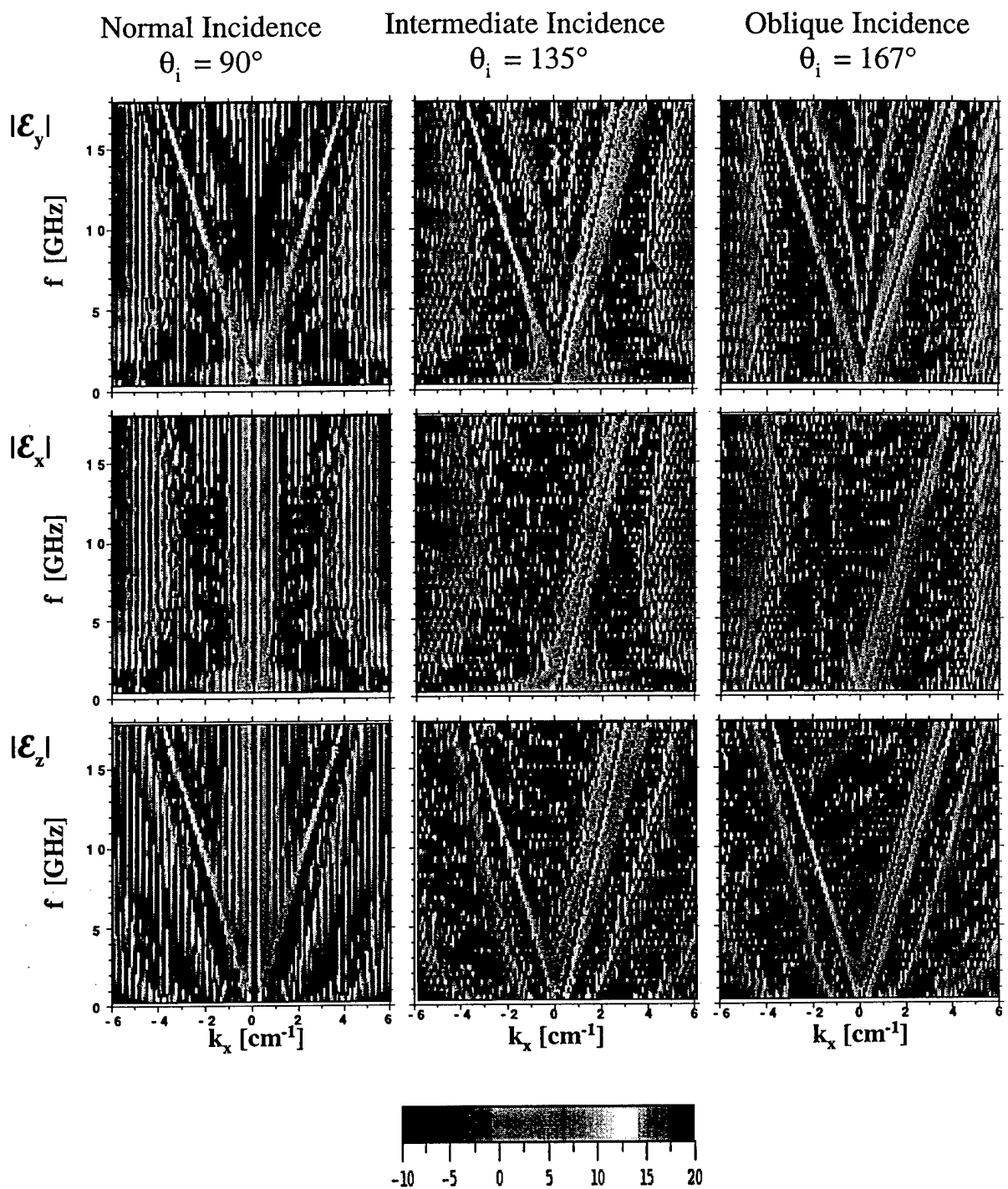


Figure 17: Comparison of computed  $\omega$ - $\kappa$  representations for a p.e.c. strip without a gap at broadside and oblique illumination. The strip width and the field sampling are as in Figure 14.

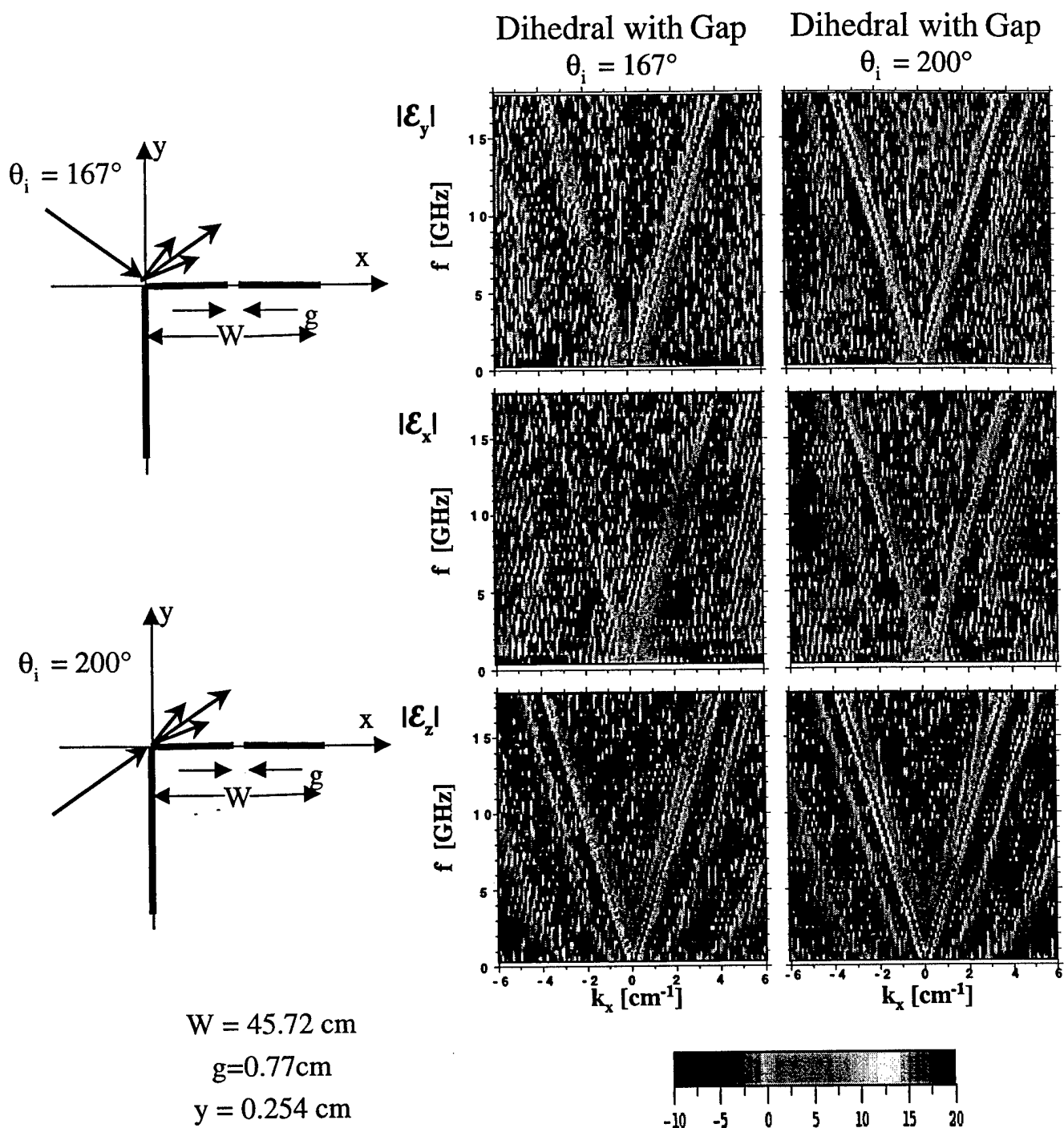


Figure 18: Comparison of computed  $\omega$ - $\kappa$  representations for a p.e.c. right angle dihedral where the gap is either in the shadow or illuminated region. The gap width is 0.3 in. (0.77 cm). The sides of the dihedral are 18 in. (45.72 cm) wide. The fields are sampled along  $y = 0.1$  in. (0.254 cm).

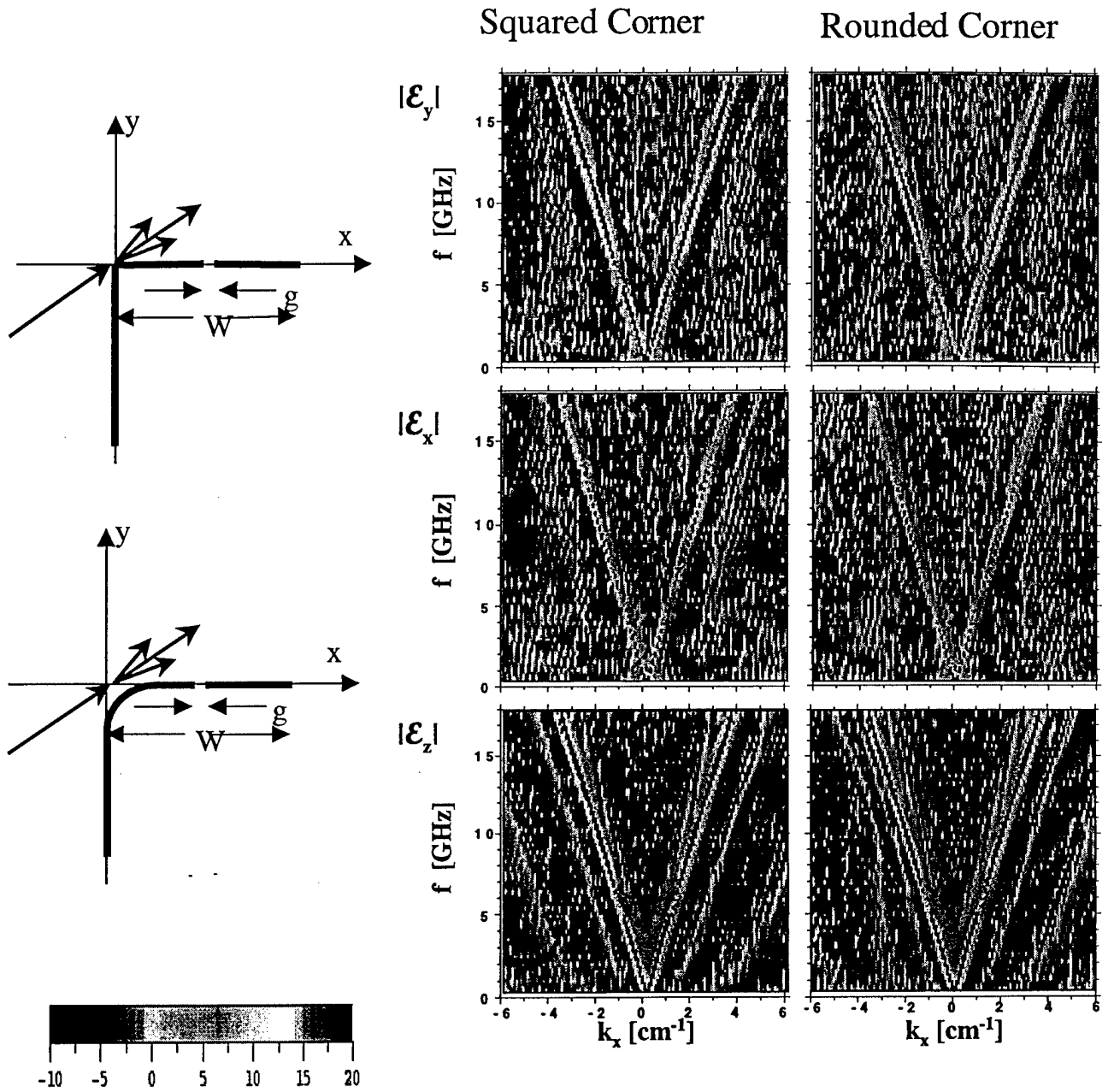


Figure 19: Comparison of computed  $\omega$ - $\kappa$  representations for p.e.c. dihedrals with right angle and rounded corners. The illumination is at  $\phi_1 = 200^\circ$ . The other parameters are as in Figure 18.



To illustrate the generality of the present formulation, the  $\omega$ - $\kappa$  maps were also generated for finite arrays of evenly spaced electrically narrow strips. Some representative examples of these cases are summarized below.

Figure 20 shows the measured and computed field intensities for a finite 14 element array of equally spaced narrow strips modeling the rods used in the experiments. The results show that the dominant fields are the forward propagating ones. The brightest line to the right has a slope equal to  $c/2\pi \cos (2\pi - \phi_i)$ , where  $\phi_i$  is the angle of the incident illumination. The parallel lines of lower intensity are the Bragg lobes, characteristic of a periodic structure. Since the present structure is finite, i.e. quasi-periodic, the lines are diffraction broadened by the width of the array. The Bragg lobes are separated along  $x$ -direction by  $\Delta k_x = 2\pi n/s$ , where  $s$  is the spacing of the array elements and  $n$  is the Bragg mode number. In the present case for  $n=1$ ,  $\Delta k_x = 2.74 \text{ cm}^{-1}$ . For frequencies above 7 GHz, this mode is propagating; for frequencies above 14 GHz, the next order mode is also propagating. The negative  $k_x$  in these cases indicates that the fields associated with these Bragg modes are moving in a direction opposite to the incident field. These are sometimes called side waves on gratings.

Figure 21 depicts comparable results for a finite 10 element array of elements having two different spacings. In the infinite case, this would correspond to a doubly periodic structure. The  $\omega$ - $\kappa$  map in this case shows a rich structure consisting of a set of intensities corresponding to the two spacings. The experimental results in Figures 20 and 21, are again characterized by a variation of the intensity lines with frequency. As in the case of the experimental results for the plate (Fig. 16), these variations arise from the frequency dependent character of the probe coupling with the target.

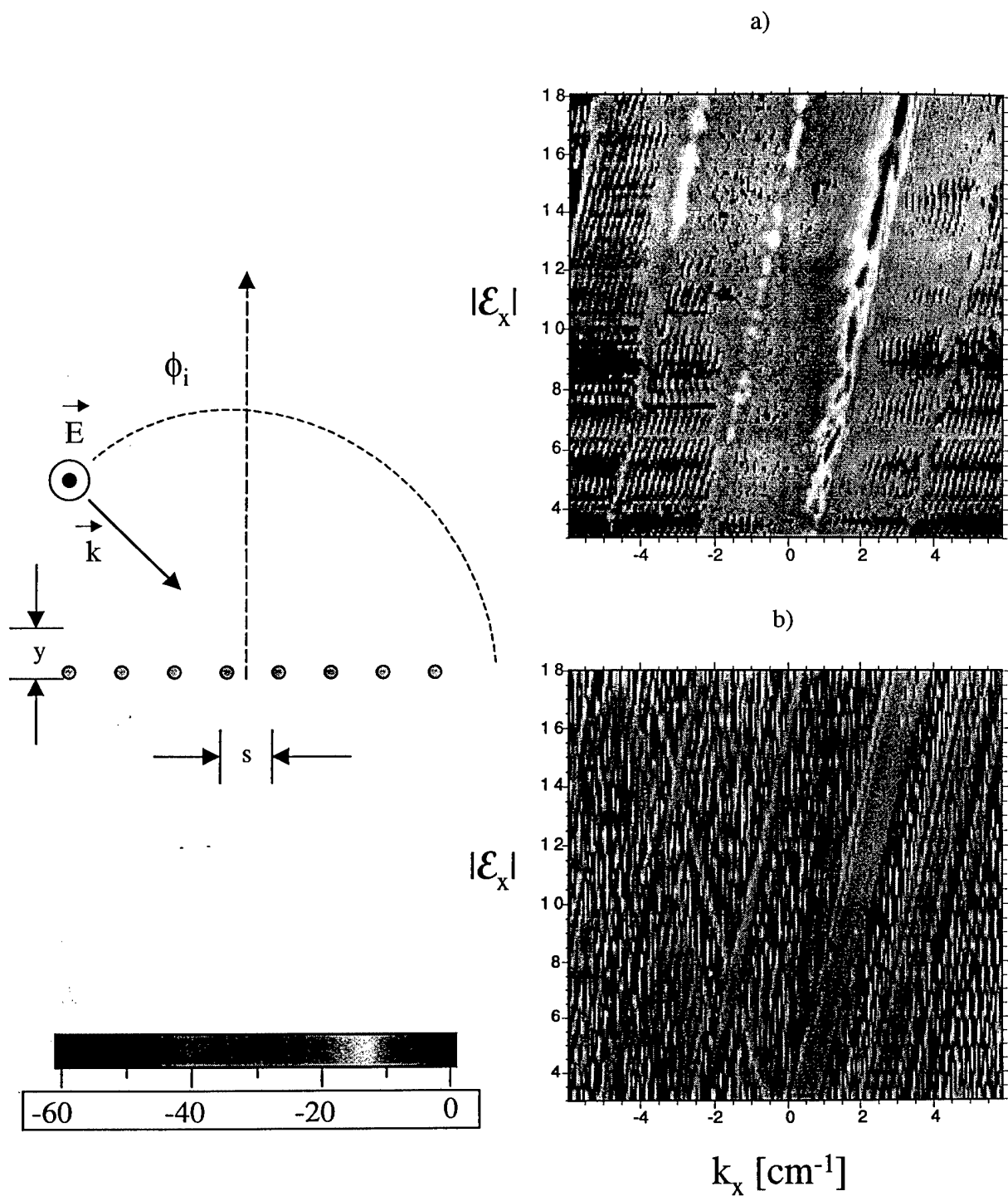


Figure 20.  $\omega$ - $\kappa$  representations for a 14 element evenly spaced array of elements. (a) measured, (b) computed. The incident field is TM polarized and  $\phi_i = 145^\circ$ ,  $s = 2.29$  cm. The fields are sampled along  $y = 0.254$  cm above the array.

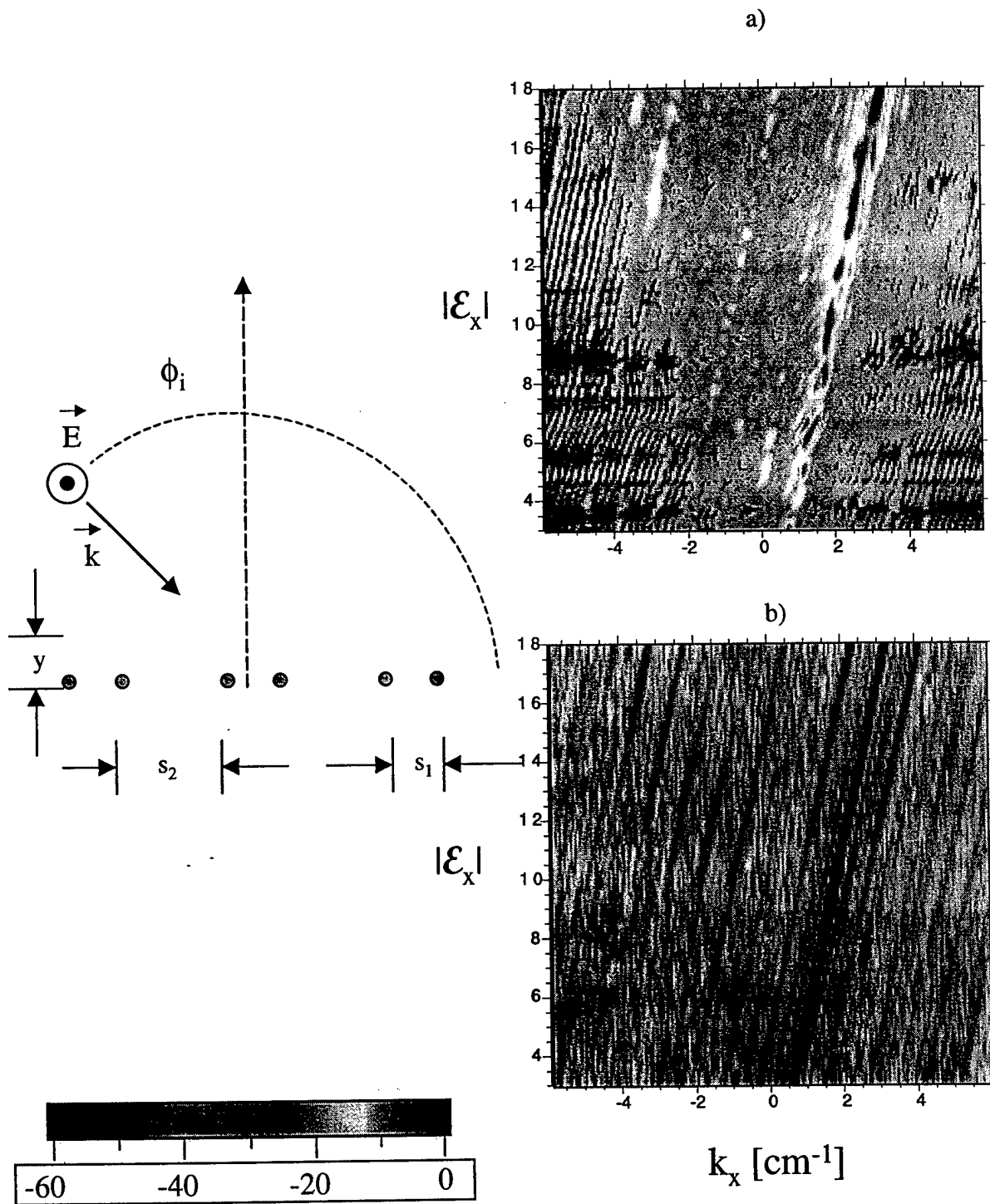


Figure 21.  $\omega$ - $\kappa$  representations for a 14 element evenly spaced array of elements. (a) measured, (b) computed. The incident field is TM polarized and  $\phi_i = 145^\circ$ ,  $s_1 = 2.29$  cm and  $s_2 = 4.57$  cm. The fields are sampled along  $y = 0.254$  cm above the array.

## 5. SUMMARY/CONCLUSIONS

This experimental and theoretical investigation explored the application of using ultra-near field techniques in the microwave region. The current study focused on the scattering from large planar structures, including dihedrals with surface gaps and rounded edges. An experimental facility for this purpose was designed and built at NRL. This Ultra-Near Field Facility was used to measure the scattered fields from a variety of targets under bistatic illumination.

The spatially resolved fields in the proximity of the targets were transformed into  $\omega$ - $\kappa$  maps that allowed delineation of detailed features of the propagated and evanescent fields. From these the forward- and back-scattered field components, the associated propagation constants, and the diffraction effects could be obtained over a band of frequencies as a function of surface and edge discontinuities.

The experimental studies were complemented with analytical studies of near and ultra-near fields in the proximity of targets. A formulation, implemented with modification of a special version of the method of moments based CARLOS code, was used to compute these fields. Extensive numerical simulations were carried out generating  $\omega$ - $\kappa$  maps for a variety of 2-D surfaces to characterize the effects of surface discontinuities on the propagated and evanescent fields.

From these investigations, we conclude:

- The  $\omega$ - $\kappa$  mapping of the ultra-near fields provides a unique diagnostic tool to visualize the structure of evanescent fields near targets. The results for the strips, plates, and dihedrals showed that the evanescent fields are associated principally with the edge diffraction from these surfaces.
- For quasi-periodic structures,  $\omega$ - $\kappa$  mapping provides a highly effective diagnostic and visualization tool for Bragg scattering. Spectral broadening can be observed.
- Measurement of ultra-near fields require specially designed probes. An electrically small dipole probe with a balun gave the best performance with respect to signal sensitivity and polarization discrimination.
- Probe/target interactions remain a significant problem in ultra-near field measurements. This limitation is not present in acoustic near field measurements. No satisfactory method was found for simultaneously calibrating electric and magnetic probes needed in cylindrical back-propagation.
- Ultra-near field measurements could become a new diagnostic tool to study material inhomogeneities. It could be a useful adjunct to conventional material measurement techniques, such as the NRL arch, transmission/reflection tunnels, and cavity techniques.
- Computer simulations using a direct formulation for obtaining the spectrally transformed ultra-near fields proved to be accurate and fast compared with conventional indirect methods using an FFT of the computed fields in the proximity of a target. A generalization of this technique was developed for arbitrary 2-D (body of translation) geometries.

## APPENDIX A:

### ANCILLARY EQUATIONS FOR FORMULATIONS IN SECTION 3

#### Method of Moments Formulation

The general expression for the impedance elements in Eq. 4a is given by:

$$Z_{ij}^{\alpha\alpha} = \int \int_{C_i C_j} dt dt' \left\{ j\omega\mu_0 \vec{W}_i^\alpha \cdot \vec{J}_j^\alpha + \frac{j}{\omega\epsilon_0} (\nabla \cdot \vec{W}_j^\alpha) (\nabla \cdot \vec{J}_i^\alpha) \right\} \Phi(kR) \quad (A-1)$$

where  $\alpha = t$  or  $z$ . Explicit expressions for the impedance elements  $Z_{ij}^{\alpha\alpha}$  in Eq. 4 can be derived from the finite BOT results in [9] as follows. Since in the present case the BOT is infinite along the  $z$ -axis, the expansion and testing functions do not have any  $z$ -dependence, i.e. this corresponds to the  $n=0$  mode result in Eqs. 8 and 11 of [9]. Thus

$$Z_{ij}^{tt} = \int \int_{C_i C_j} dt dt' \left\{ j\omega\mu_0 \cos(v - v') f_i^t f_j^t + \frac{j}{\omega\epsilon_0} \dot{f}_i^t \dot{f}_j^t \right\} \Phi(kR) \quad (A-2)$$

$$Z_{ij}^{zz} = \int \int_{C_i C_j} dt dt' j\omega\mu_0 f_i^z f_j^z \Phi(kR) \quad (A-3)$$

where the divergence of a vector  $A$  on the BOT is

and where  $v$  and  $v'$  are the angles between the BOT generating curve  $C(t)$  and  $x$ -axis at the points  $(x, y)$  and  $(x', y')$ , respectively. Since in the present case the BOT is infinite along the  $z$ -axis, there are no  $t$ -directed edges on the surface and thus there are no impedance elements cross-coupling the  $t$ - and  $z$ -directed currents, i.e. terms corresponding to Eqs. 9 and 10 in [9] are zero.

It is customary when using overlapping triangle functions as basis and testing functions to approximate these  $f_j$  and their derivatives  $df_j/dt$  as four pulses, denoted by  $T_p$  and  $\dot{T}_p$  respectively, i.e.  $T_p = \{1/4, 3/4, 3/4, 1/4\}$  and  $\dot{T}_p = \{1, 1, -1, -1\}$ . Thus each segment of  $C(t)$  is approximated by 4 straight line segments associated with these pulses. Using a centroid approximation for the integrations over  $t$  and  $t'$ , yields

$$Z_{ij}^{tt} \cong jk\eta \sum_{p,q=1}^4 \left\{ T_p^t T_q^t \cos(v_p - v_q) - \frac{1}{k^2} \dot{T}_p^t \dot{T}_q^t \right\} \Delta t_p \Delta t_q \Phi(kR_{pq}) \quad (A-4)$$

$$Z_{ij}^{zz} \cong jk\eta \sum_{p,q=1}^4 T_p^z T_q^z \Delta t_p \Delta t_q \Phi(kR_{pq}) \quad (A-5)$$

where  $\eta$  is the free space wave impedance. The expression for the excitation vector in Eq. 4 is given by

$$V_i^\alpha = \int_{C_i} dt (\vec{u}_\alpha \cdot \vec{E}^i) f_i^\alpha(t) \quad (\text{A-6})$$

where for TE and TM the respective expressions are

$$V_i^t = \sum_{p=1}^4 \Delta t_p T_p^t \sin(v_p - \phi_0) e^{jk\psi_p} \quad (\text{A-6a})$$

$$V_i^z = \sum_{p=1}^4 \Delta t_p T_p^z e^{jk\psi_p} \quad (\text{A-6b})$$

### $\omega$ - $\kappa$ Transformation of L Operator

The transform of the L operator is given by

$$\tilde{L}\vec{X}(t) = j\omega\mu_1 \int_{C(t)} dt' \vec{X}(t') A + \frac{j}{\omega\epsilon} \int_{C(t)} dt' (\nabla' \cdot \vec{X}(t')) \vec{B} \quad (\text{A-7})$$

where

$$A = \frac{1}{2j} \int_0^\infty H_0^{(2)}(kR) \cos k_x x dx \quad (\text{A-8})$$

$$\vec{B} = \nabla A \quad (\text{A-9})$$

The interchange of the order of integration in Eq. (A-1) does not affect the convergence of the integral. Letting  $\bar{x} = x - x'$  and  $\bar{y} = y - y'$  and  $R = \sqrt{(x^2 + y^2)}$ , and noting that the integrand is even, using the integral identities in [13], yields

$$A = \frac{1}{2j} e^{jk_x x'} \begin{cases} \frac{1}{K_1} e^{-jK_1 \bar{y}} & 0 < k_x < k_1 \\ \frac{j}{K_x} e^{-K_x \bar{y}} & 0 < k_1 < k_x \end{cases} \quad (\text{A-10})$$

where  $y > 0$  and  $K_1 = \{k_1^2 - k_x^2\}^{1/2}$  and  $K_x = \{k_x^2 - k_1^2\}^{1/2}$ . Carrying out the gradient operation on  $\vec{B}$  and shifting the coordinates as before yields

$$\vec{B} = \vec{u}_x \frac{1}{4j} e^{jk_x x'} \int_{-\infty}^{\infty} \frac{\partial H_0^{(2)}(k\bar{R})}{\partial \bar{x}} e^{jk_x \bar{x}} d\bar{x} + \vec{u}_y \frac{\partial A}{\partial y} \quad (\text{A-11})$$

The first term can be evaluated in terms of the results from Eq. (A-8), using a theorem on Fourier transform given in [14]. Thus for  $y > 0$

$$\vec{B} = -\frac{1}{2}e^{jk_x x'} \begin{cases} \left( \vec{u}_x \frac{k_x}{K_1} + \vec{u}_y \right) e^{-jK_1 \bar{y}} & 0 < k_x < k \\ \left( \vec{u}_x j \frac{k_x}{K_x} + \vec{u}_y \right) e^{-K_x \bar{y}} & 0 < k_1 < k_x \end{cases} \quad (\text{A-12})$$

### $\omega$ - $\kappa$ Transformation of K Operator

The transform of the K operator is given by

$$\tilde{K}\vec{X}(t) = \int_{C(t)} dt' \vec{X}(t') \times \vec{B} = \int_{C(t)} dt' \begin{Bmatrix} X^z(t') B_1 \\ X^t(t') B_2 \end{Bmatrix} \quad (\text{A-13})$$

Noting  $\vec{u}_t = \vec{u}_x \cos v + \vec{u}_y \sin v$  where  $v$  is the angle subtended between  $C(t)$  and the  $x$ -axis, forming the cross-products in Eq. (A-7), yields

$$\vec{B}_1 \equiv \vec{u}_t \times \vec{B} = \frac{1}{2}e^{jk_x x'} \begin{cases} \left( \vec{u}_x - \vec{u}_y \frac{k_x}{K_1} \right) e^{-jK_1 \bar{y}} & 0 < k_x < k \\ \left( \vec{u}_x - \vec{u}_y j \frac{k_x}{K_x} \right) e^{-jK_x \bar{y}} & 0 < k_1 < k_x \end{cases} \quad (\text{A-14})$$

$$\vec{B}_2 \equiv \vec{u}_t \times \vec{B} = -\vec{u}_z \frac{1}{2}e^{jk_x x'} \begin{cases} \left( \cos v' - \frac{k_x}{K_1} \sin v' \right) e^{-jK_1 \bar{y}} & 0 < k_x < k_1 \\ \left( \cos v' - j \frac{k_x}{K_x} \sin v' \right) e^{-jK_x \bar{y}} & 0 < k_1 < k_x \end{cases} \quad (\text{A-15})$$

## APPENDIX B:

### MONO- AND BI-STATIC RCS CALCULATIONS FOR 2-D ANALOGS OF NSWCCD TARGETS

The results in this appendix summarize monostatic and bistatic RCS calculations for 2-D analogs of the NSWCCD target cubes. The RCS measurements for these targets were carried out so that the incident electric field was either perpendicular or parallel to the cube edges corresponding to a TE or TM polarization, respectively. In this discussion and in the body of the report, TE polarization refers to the incident electric field being in the plane of incidence. Conversely in the TM case, the incident field is parallel to the plane of incidence.

Since the RCS measurements were made so that the principal illuminated edges were either co-pole or perpendicular to the incident electric field, the primary EM scattering mechanisms are analogous to that from noncircular infinite cylinders. Such cylinders are a subclass of bodies of translation (BOTs) discussed in this report. Thus it is possible to simulate these NSWCCD target cubes as BOTs with the appropriate edge radii of the original targets.

The monostatic and bistatic RCS calculations were carried out using a version of the CARLOS code at two representative frequencies, namely 6 and 9 GHz. The results were computed for 5 edge radii, i.e.  $r = 0, 0.25, 0.5, 0.625$ , and 1.0 inches. The case with  $r = 0$  corresponds to a configuration where the edges are formed by the intersection of the cylinder walls at 90 degrees. In the report this was denoted as the cylinder with a "sharp" edge. It serves as a benchmark for comparing the edge effects on the RCS for other cylinders. In all cases the cylinders were 24 in. (60.96 cm) on a side.

The computed data is arranged as follows. The monostatic RCS results for 6 GHz are given first, followed by the bistatic results computed for incident illumination at  $\phi = 90, 135$ , and 150 degrees. These angles are measured from the x-axis where  $\phi$  is the polar angle. In addition, the bistatic RCS is also given for  $\phi = 166$  degrees. This is the angle where the primary traveling wave peak is excited, often called the Peters' lobe after Prof. Leon Peters' at OSU.[18] The results are given for both TE and TM polarization for each of the edge radii. The foregoing sequence of results is repeated for 9 GHz. In this case the traveling wave peak occurs at  $\phi = 168$  degrees.

First examining the data for the cylinders at 6 GHz, we note that the monostatic RCS for both polarizations coalesce in the vicinity of the specular angles, i.e. at  $\phi = 0, 90, 180$ , and 270 degrees. The TE and TM polarized results gradually diverge from each other as one approaches odd multiples of  $\phi = 45$  degrees. In general the TE curves are strongly oscillatory while the TM curves are smoother forming an approximate envelope for the former. The behavior of the TE curves is the result of traveling waves reflected from the edges, causing constructive and destructive interference away from the specular points.

Of particular interest is the monostatic RCS behavior in the region midway between the specular angles, i.e. at odd multiples of  $\phi = 45$  degrees. In TE polarization the RCS is affected by the radius of the cylinder edge. For  $r = 0.25$  in. there is a deep but narrow null due to cancellation of the surface waves. Similar behavior is seen for  $r = 0.5$  in. and to a lesser extent for  $r = 0.625$  in. It disappears altogether for  $r = 1.0$  in. By comparison the RCS for TM polarization is relatively insensitive to changes of the target edge radius. These conclusions were borne out in the earlier measurements and simulations by NSWCCD.



The bistatic RCS results are somewhat more complex. For example, consider the TE polarized bistatic returns for  $\phi = 135$  degrees at 6 GHz for the cylinder with the sharp edge ( $r = 0$ ). Three lobe structures are visible. The strongest is due to the forward scattered fields at  $\phi = 315$  degrees. Its envelope is given by the sinc function associated with diffraction phenomena from two equally shadowed faces of the cylinder, forming an "outside" 90 degree dihedral. The other two lobe structures, symmetric about the bistatic illumination angle, are at  $\phi = 45$  and 225 degrees. The form of these lobes shows that they result from traveling waves on two equally lit faces of the cylinder.

Considering the same cylinder but illuminated at  $\phi = 150$  degrees, the forward scattered field lobe is skewed and not symmetric. Similarly the two side lobes are dissimilar. This is due to the fact that for this bistatic angle, the pair of shadowed and lit sides of the cylinder are unequally shadowed or lit. Thus the path length of the traveling waves from these faces generate a different interference pattern than before.

As in the case of the monostatic RCS, the TM polarized bistatic returns prove to be relatively insensitive to edge radius variation. Similar conclusions hold for 9 GHz.

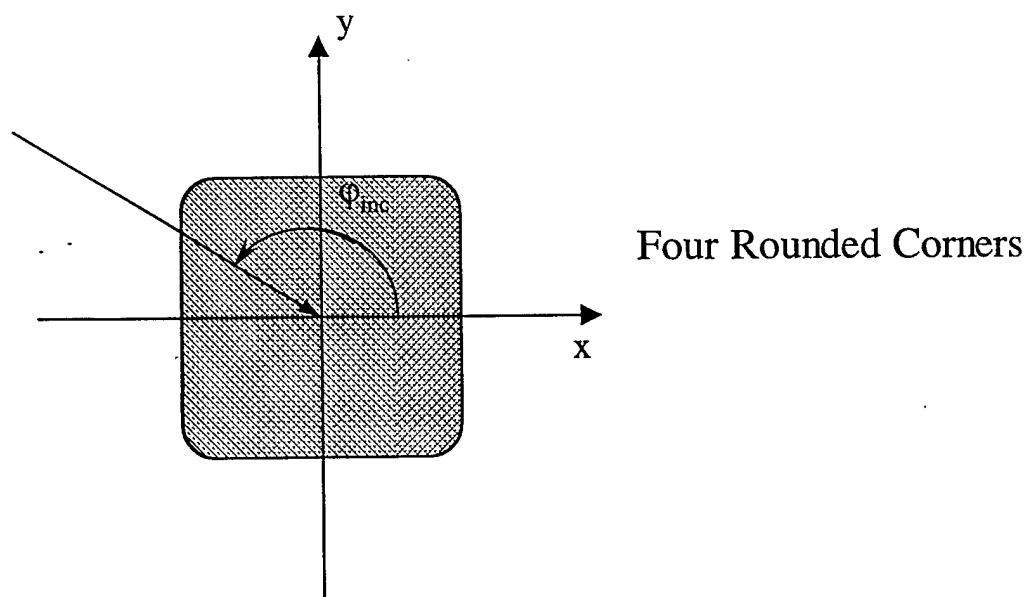
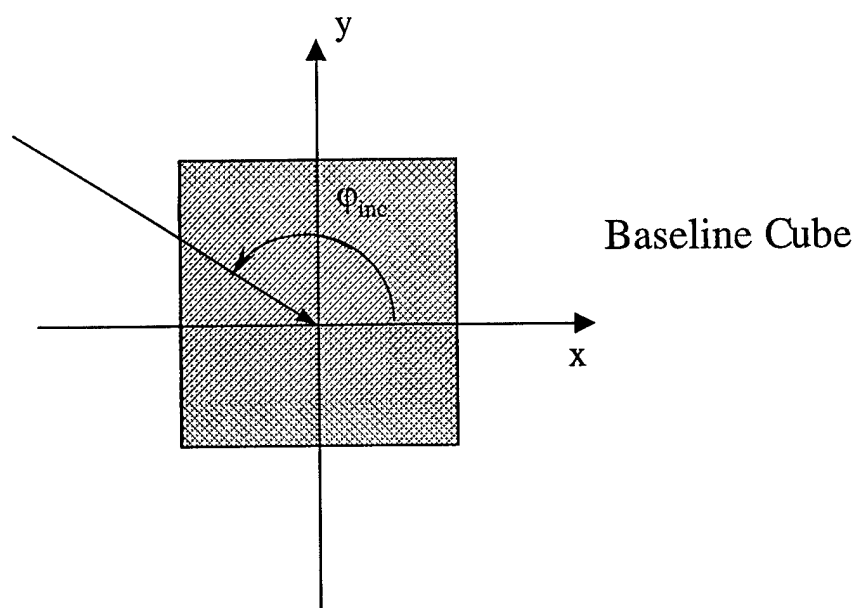


Figure B-1: Baseline Cylinder ( $r=0$ ) and cylinder with four rounded corners.

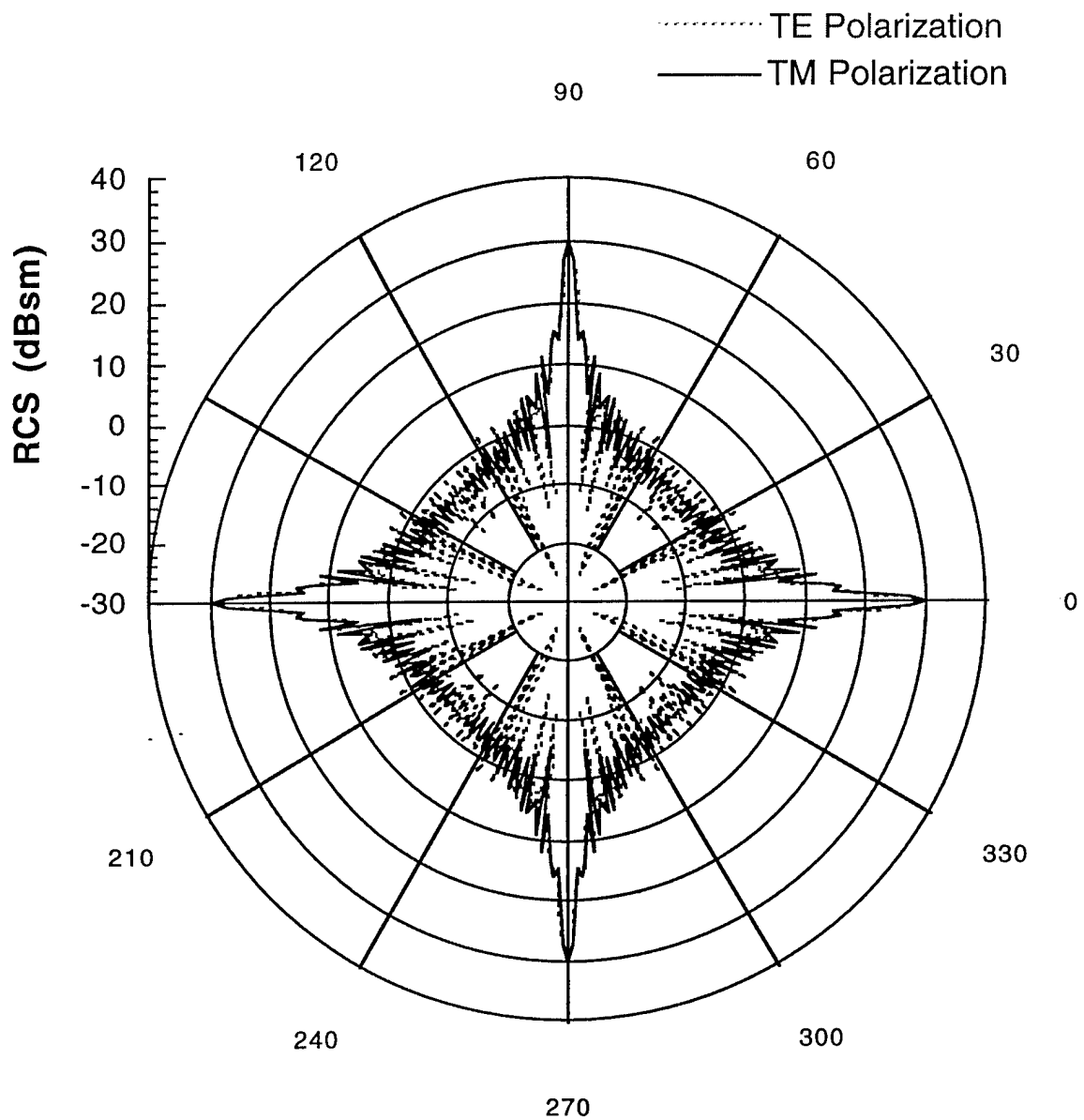


Figure B-2: Monostatic RCS of baseline cylinder at 6 GHz.

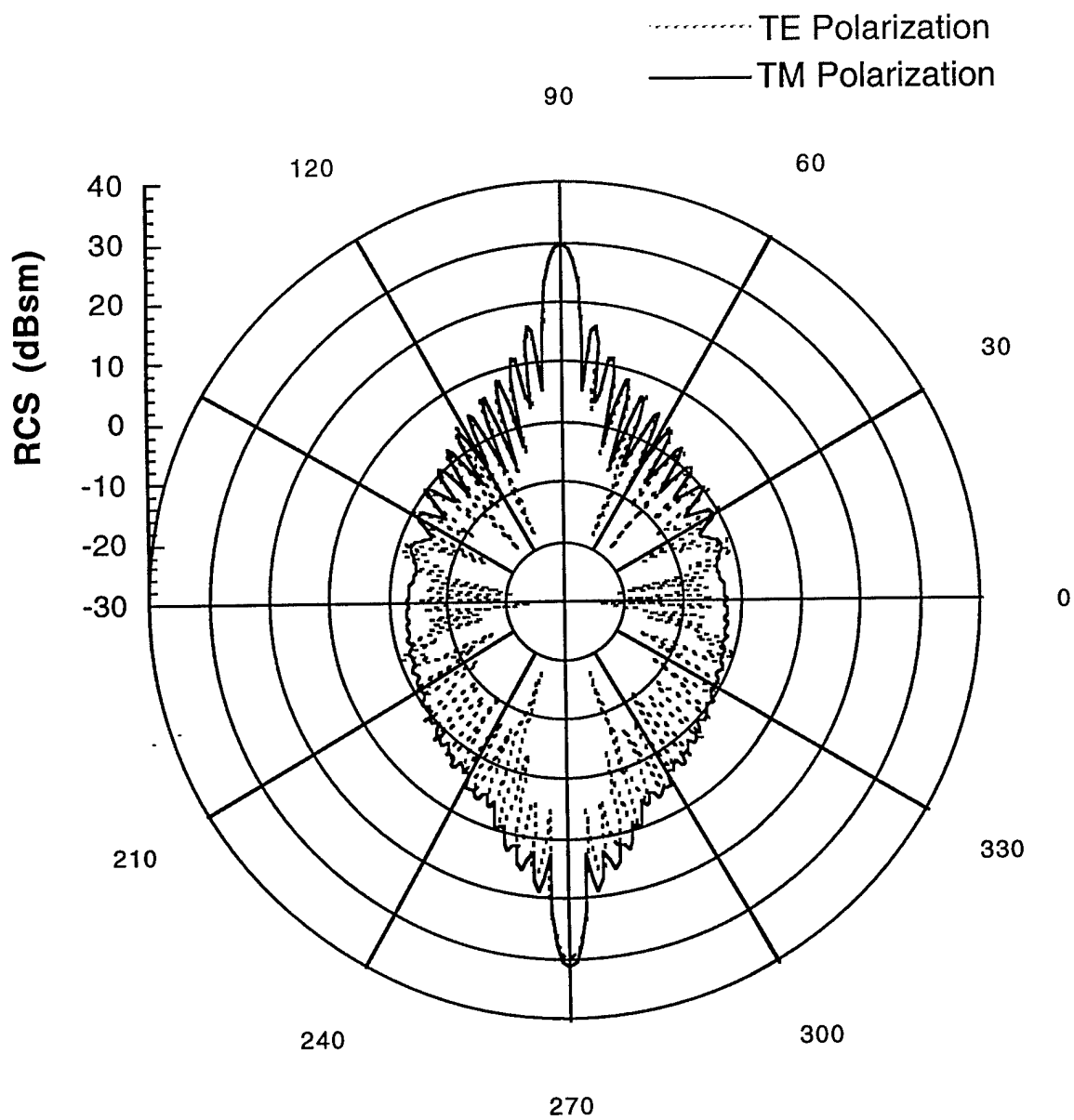


Figure B-3: Bistatic RCS of baseline cylinder at 6 GHz: Incident angle is 90 degrees.

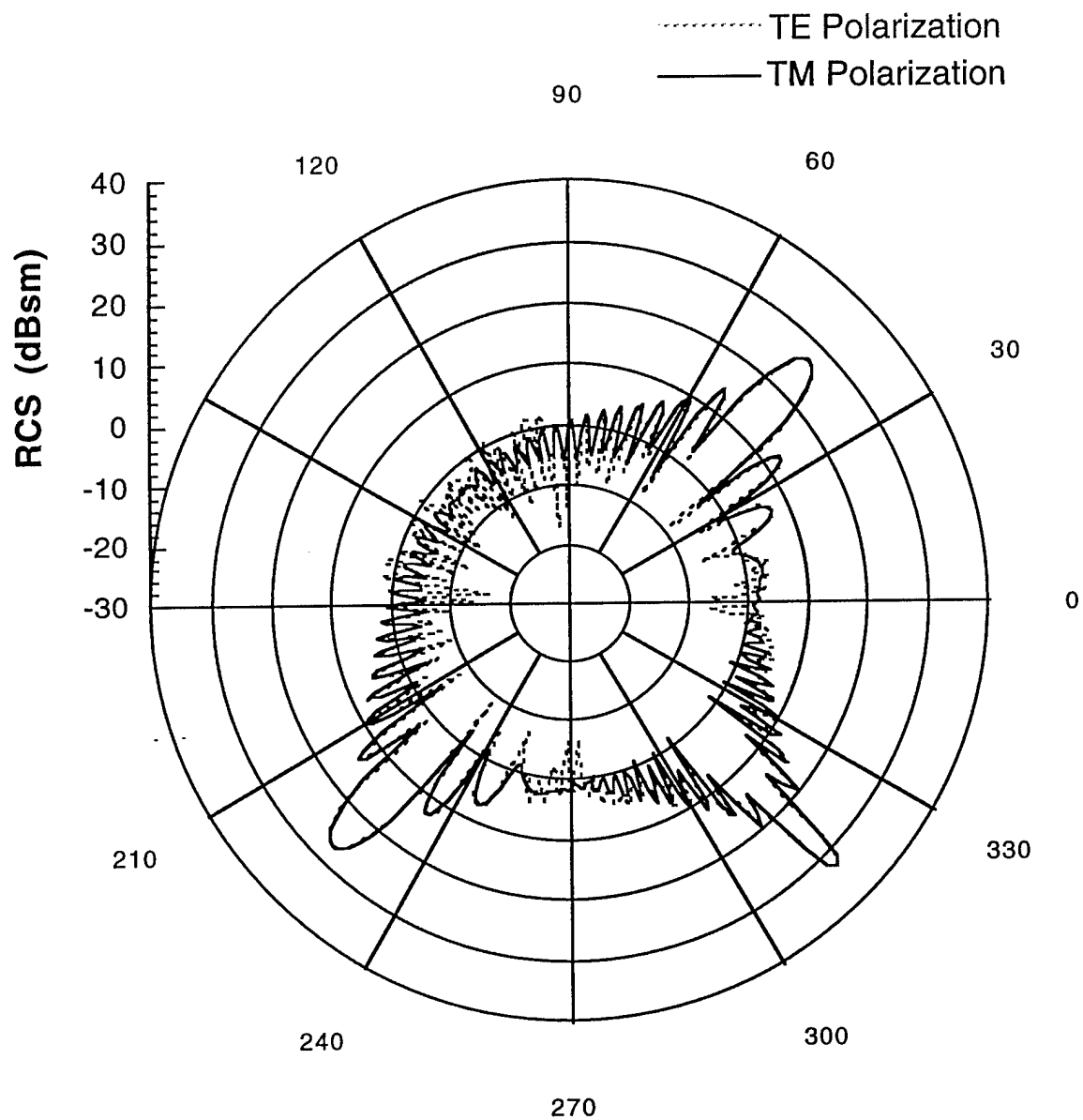


Figure B-4: Bistatic RCS of baseline cylinder at 6 GHz: Incident angle is 135 degrees.

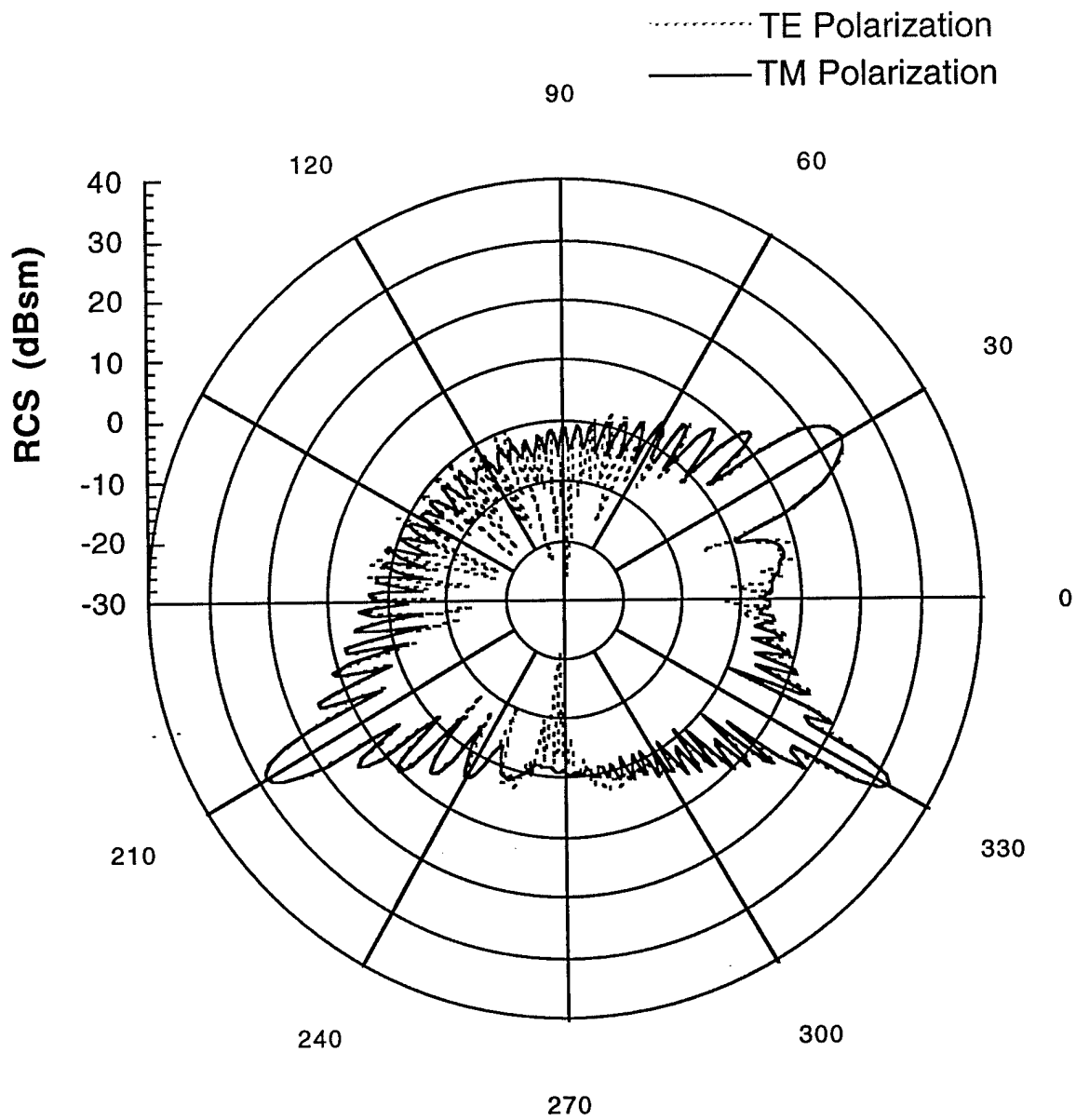


Figure B-5: Bistatic RCS of baseline cylinder at 6 GHz: Incident angle is 150 degrees.

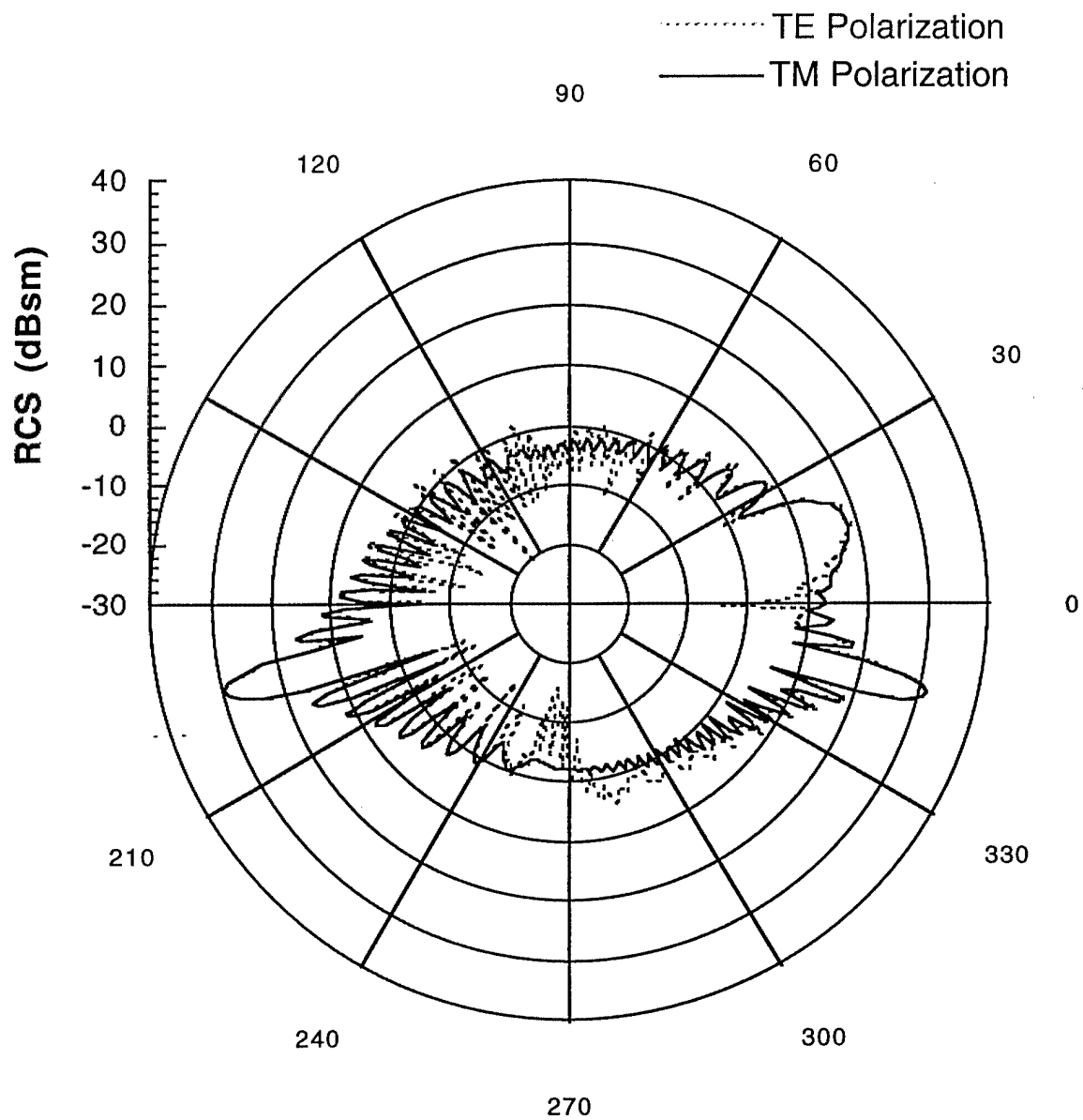


Figure B-6: Bistatic RCS of baseline cylinder at 6 GHz: Incident angle is 166 degrees (traveling wave angle).

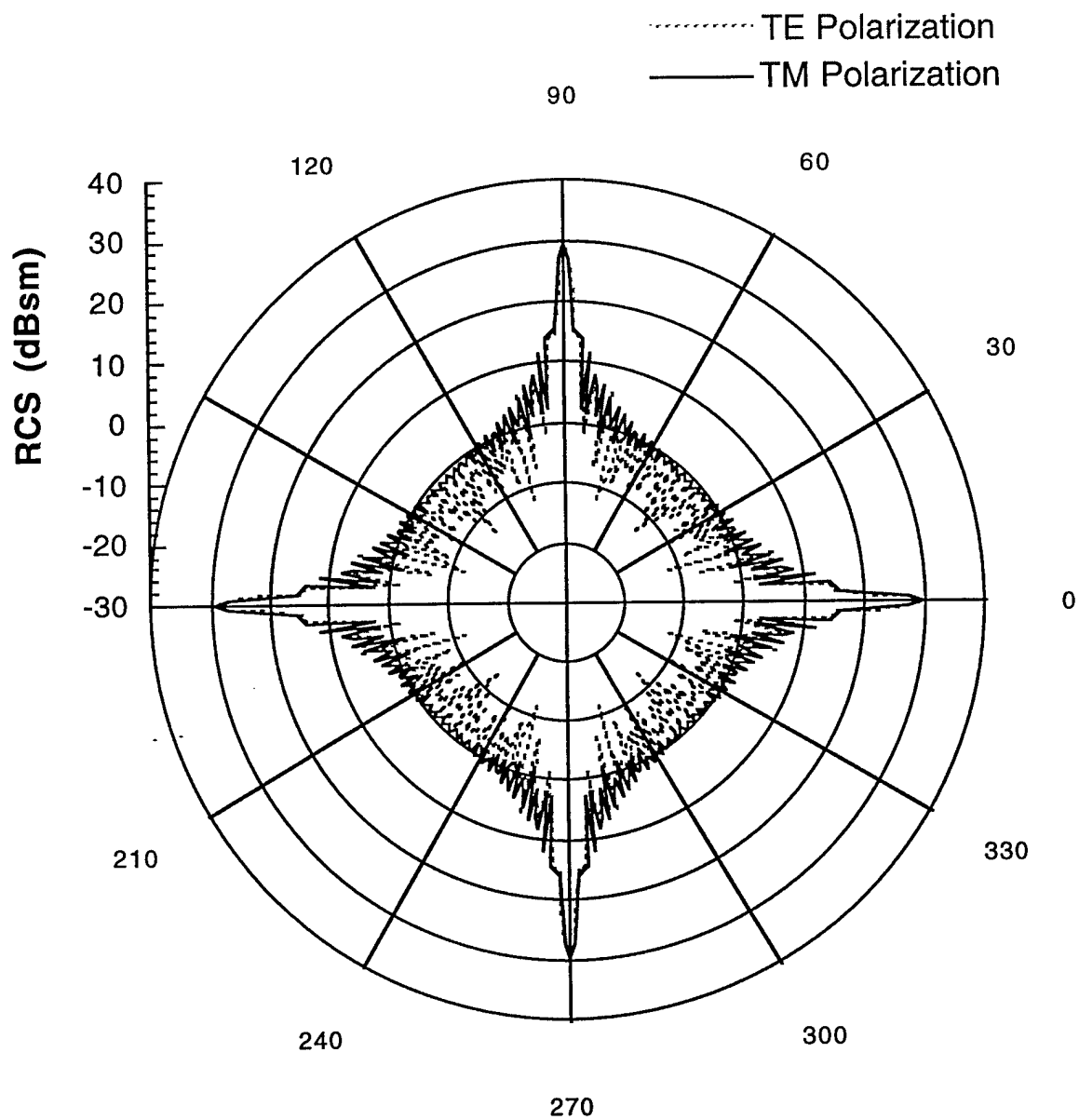


Figure B-7: Monostatic RCS of cylinder ( $r=0.25$  in.) at 6 GHz.



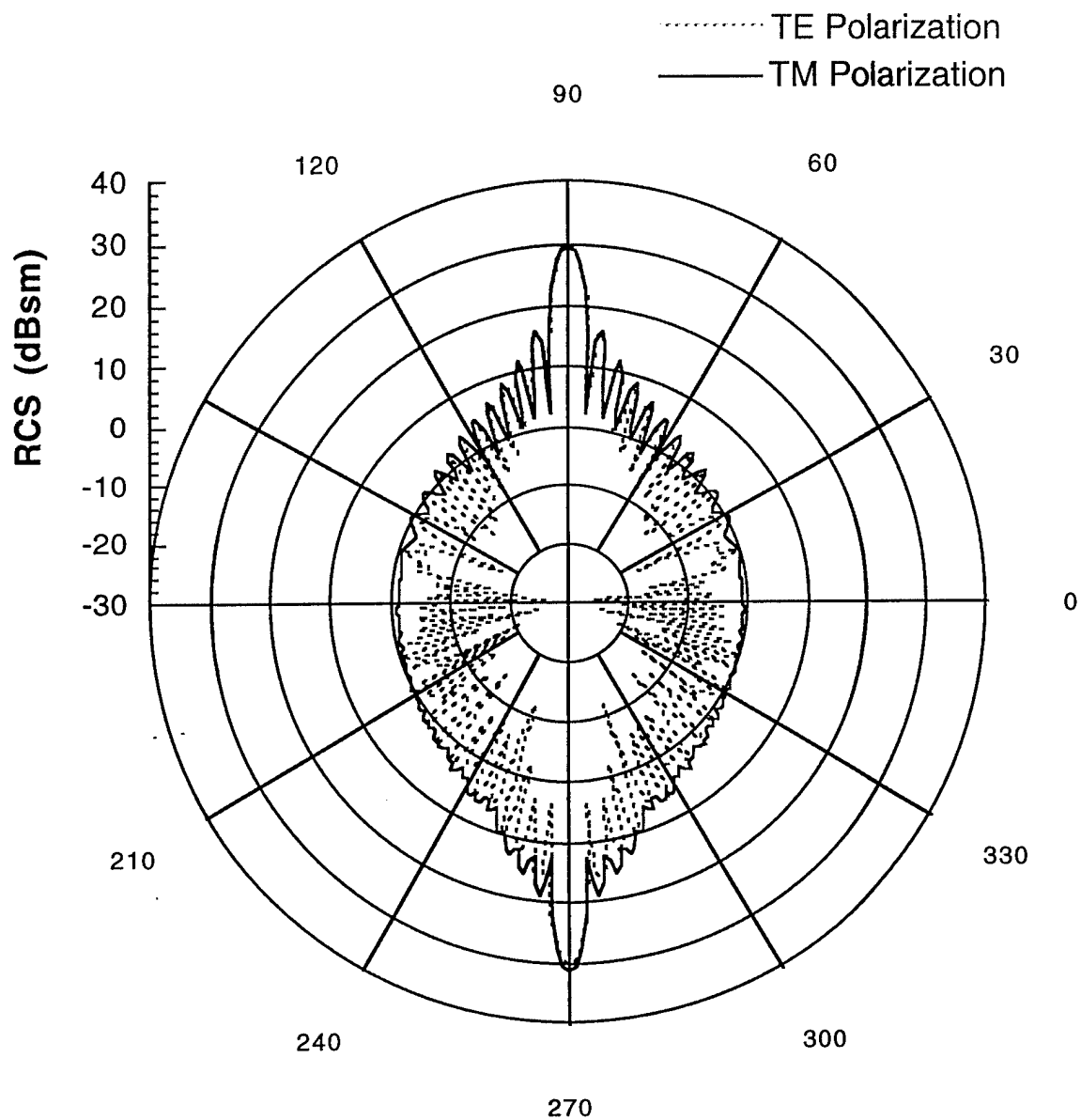


Figure B-8: Bistatic RCS of cylinder ( $r = 0.25$  in.) at 6 GHz: Incident angle is 90 degrees.

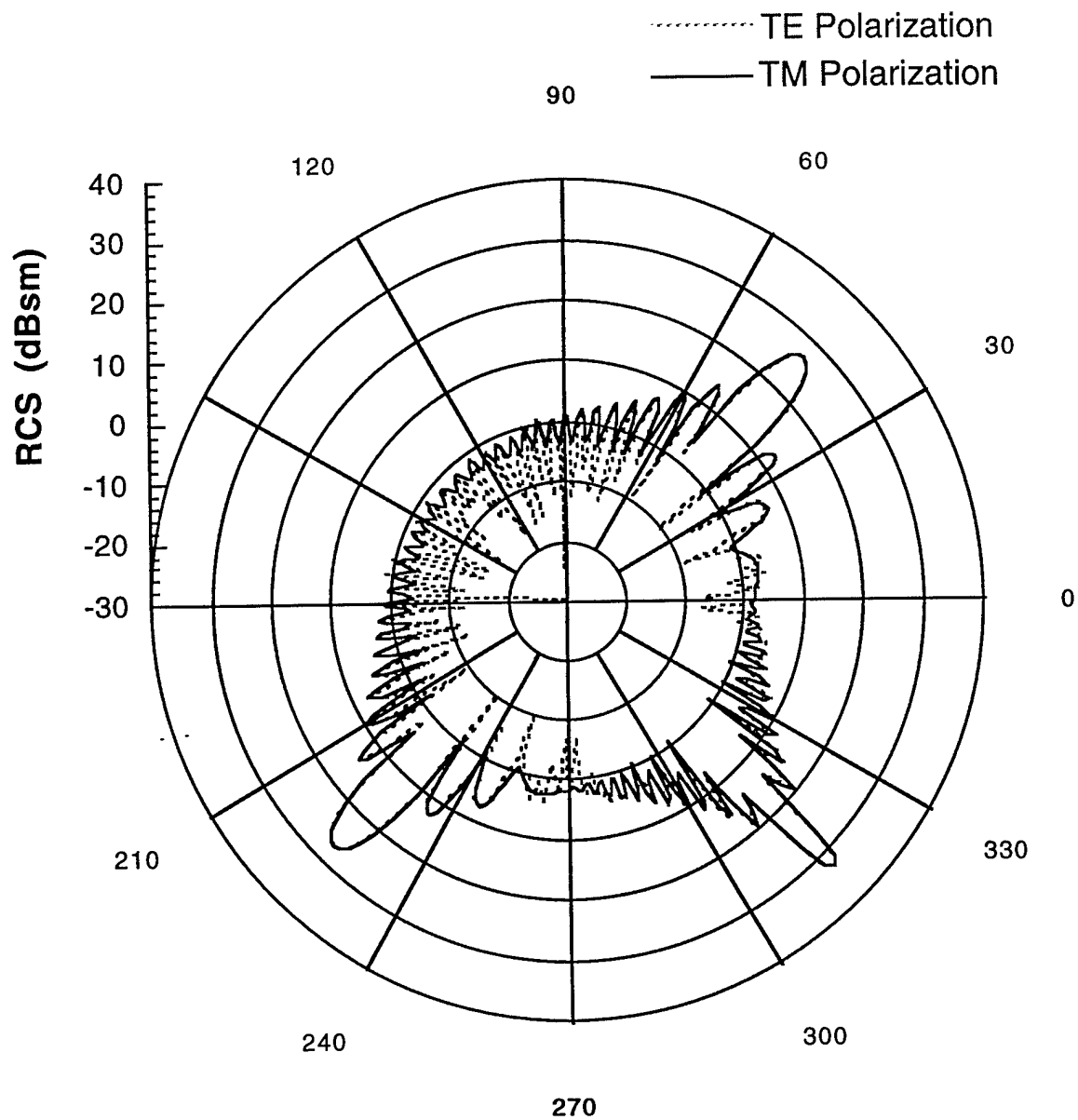


Figure B-9: Bistatic RCS of baseline cylinder ( $r = 0.25$  in.) at 6 GHz: Incident angle is 135 degrees.

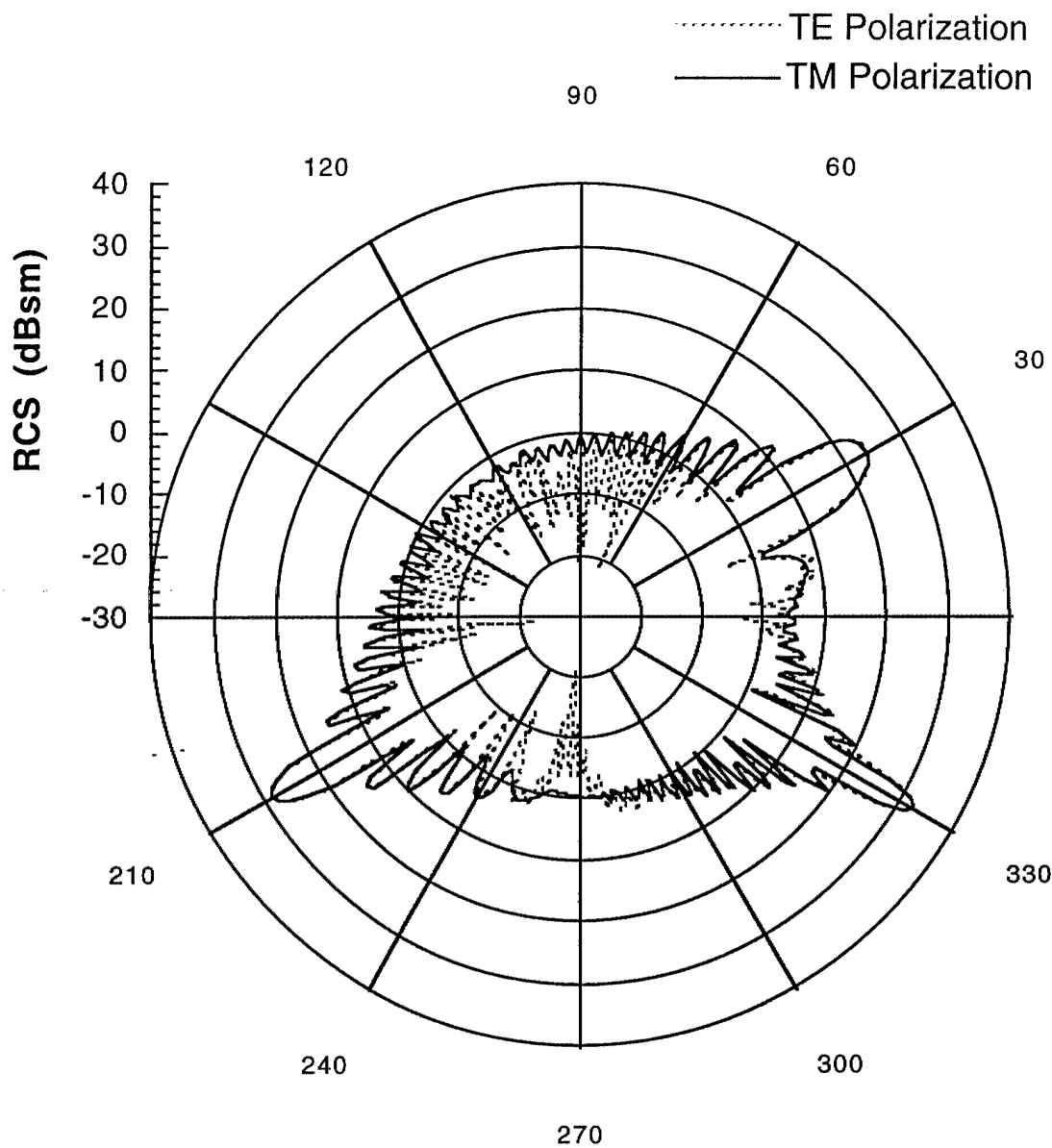


Figure B-10: Bistatic RCS of baseline cylinder ( $r = 0.25$  in.) at 6 GHz: Incident angle is 150 degrees.

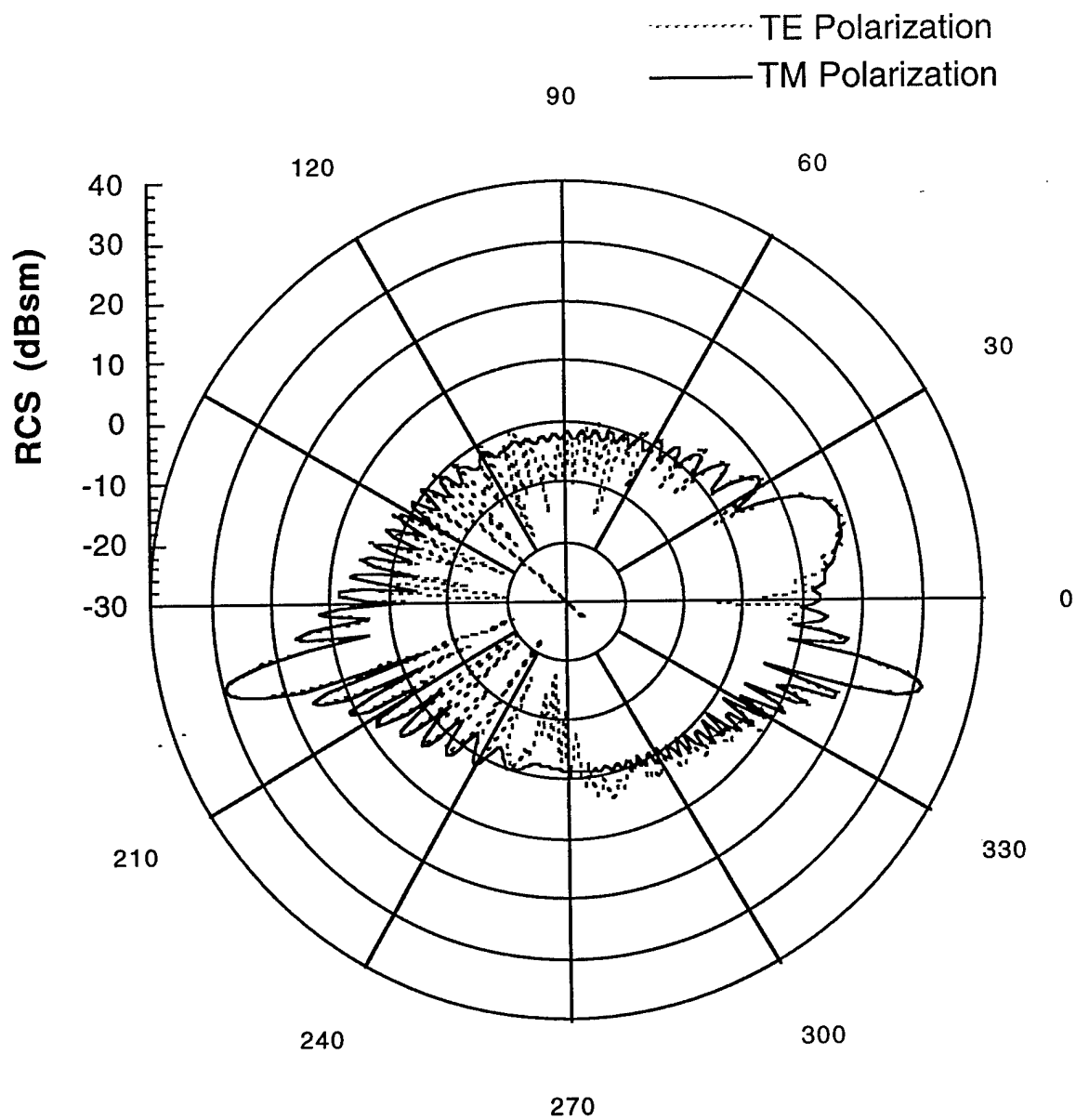


Figure B-11: Bistatic RCS of baseline cylinder ( $r = 0.25$  in.) at 6 GHz: Incident angle is 166 degrees (traveling wave angle).

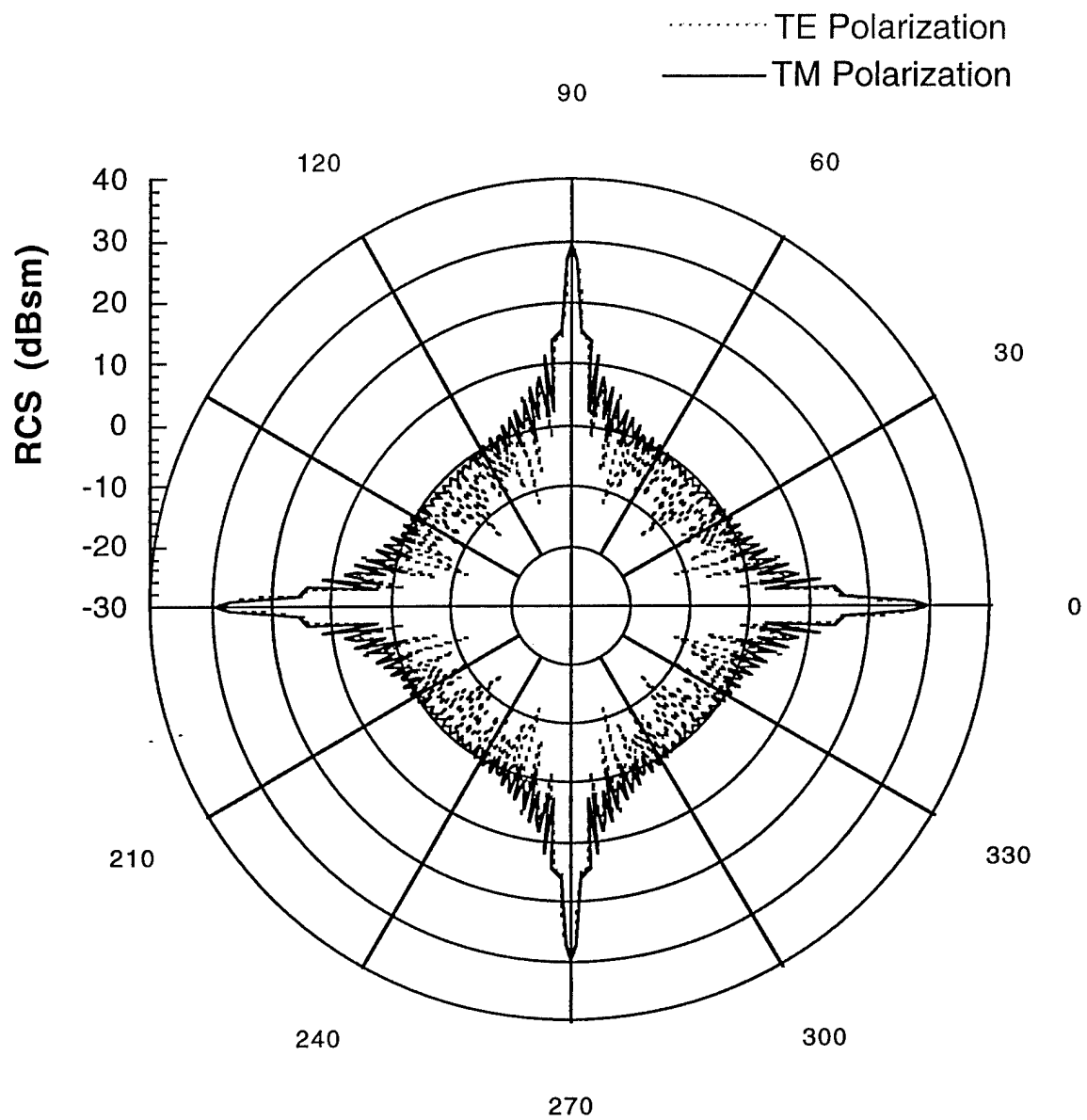


Figure B-12: Monostatic RCS of cylinder ( $r = 0.5$  in.) at 6 GHz.

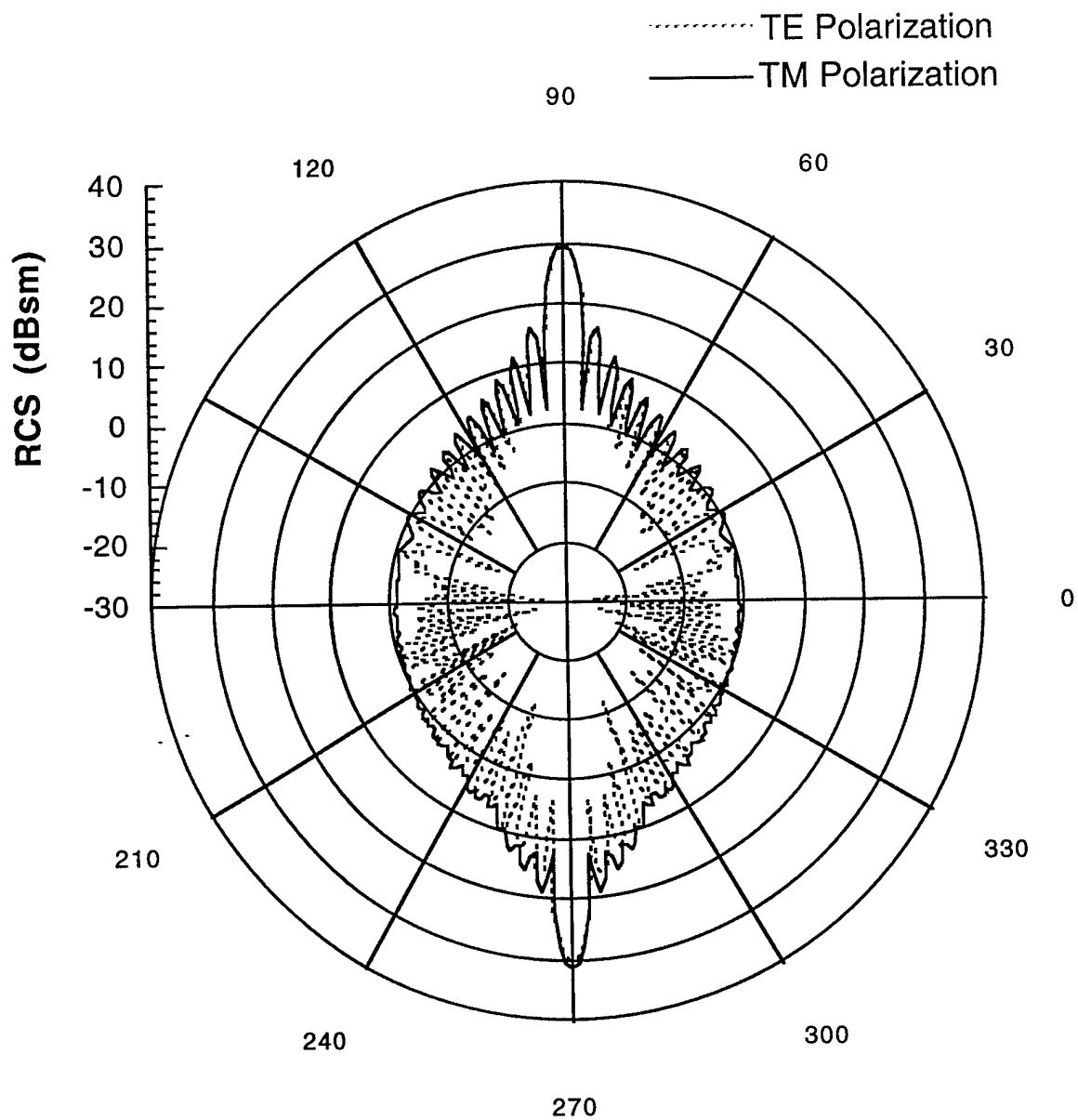


Figure B-13: Bistatic RCS of cylinder ( $r = 0.5$  in.) at 6 GHz: Incident angle is 90 degrees.

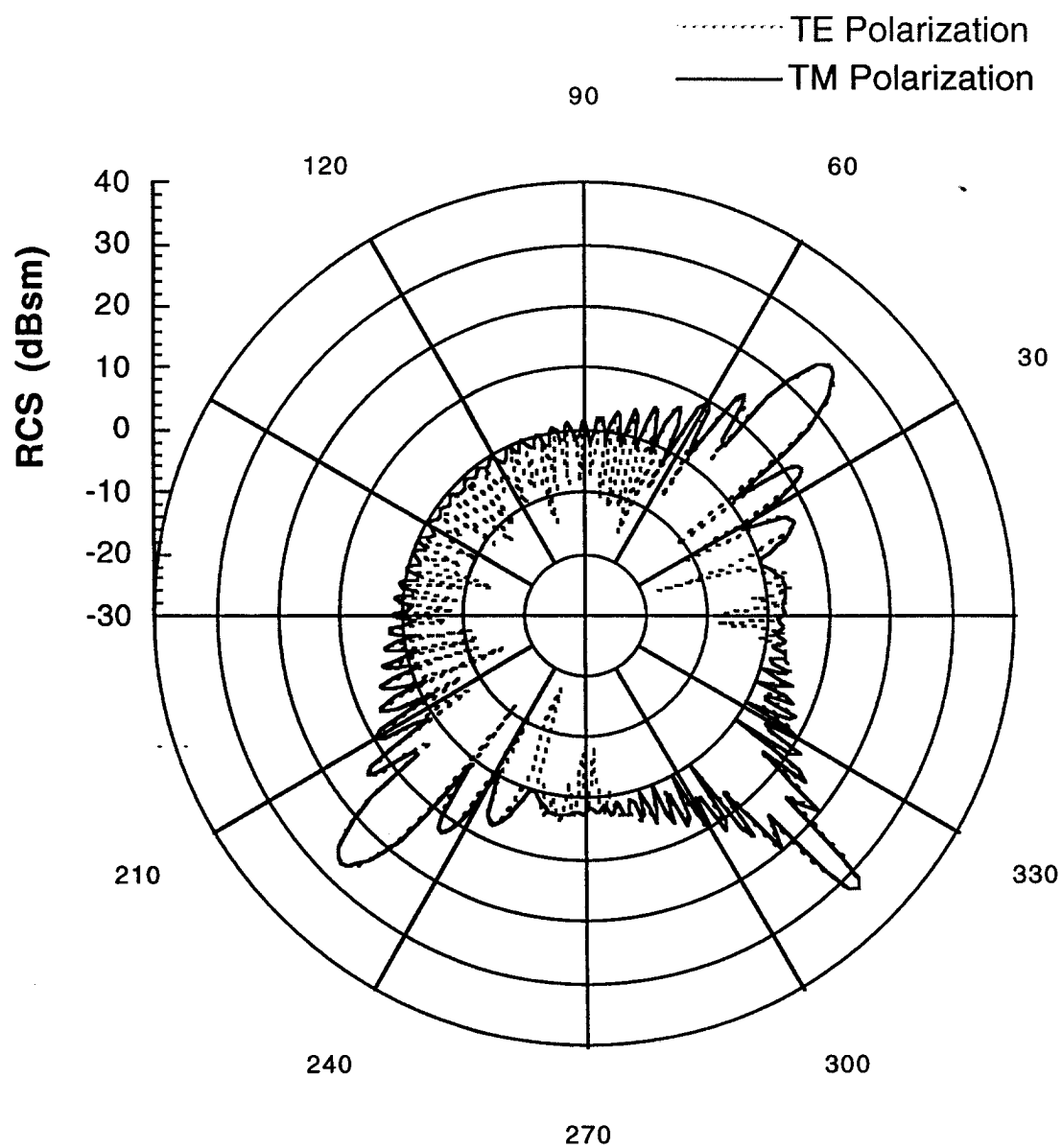


Figure B-14: Bistatic RCS of baseline cylinder ( $r = 0.5$  in.) at 6 GHz: Incident angle is 135 degrees.

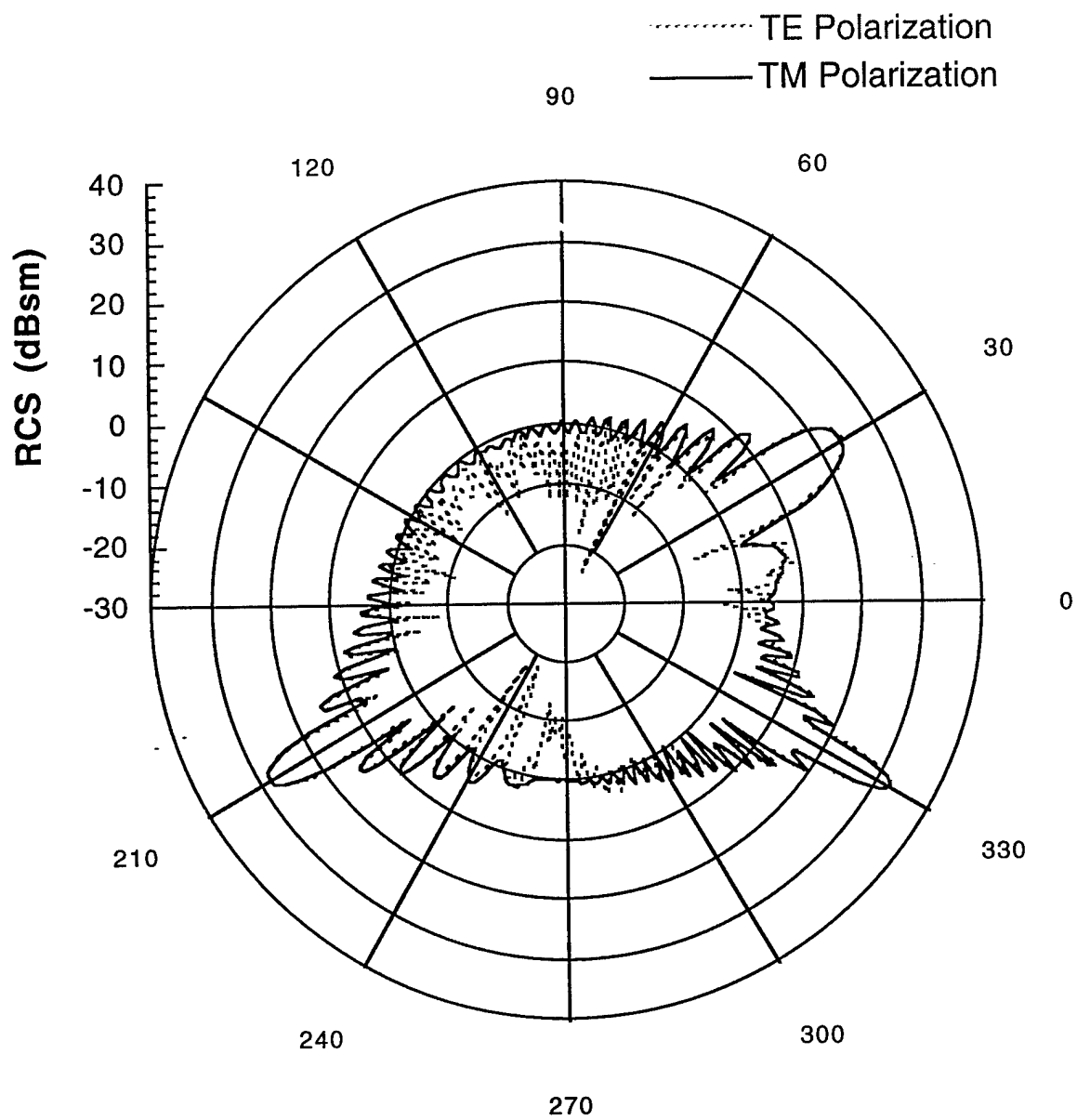


Figure B-15: Bistatic RCS of baseline cylinder ( $r = 0.5$  in.) at 6 GHz: Incident angle is 150 degrees.



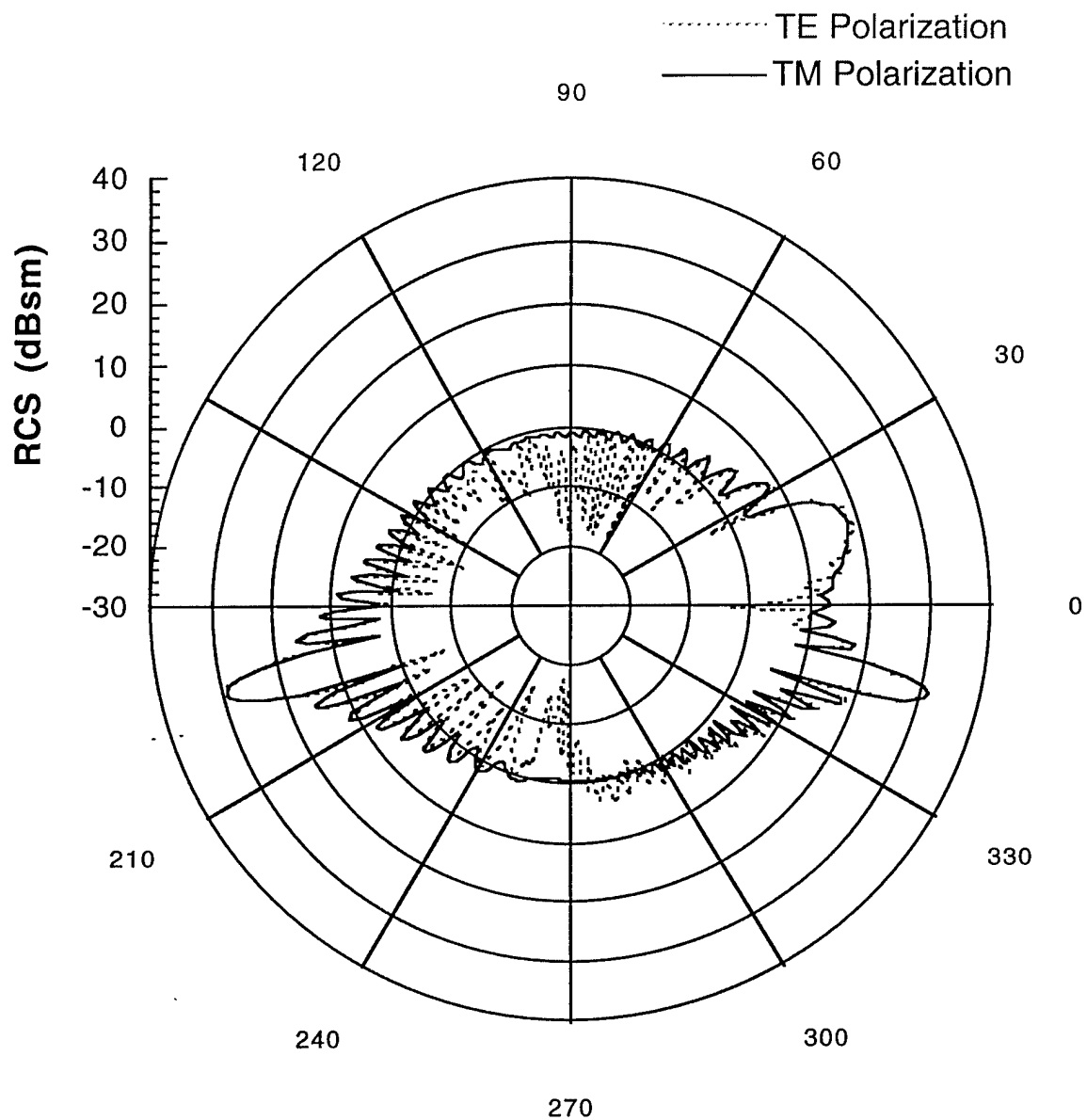


Figure B-16: Bistatic RCS of baseline cylinder ( $r = 0.5$  in.) at 6 GHz: Incident angle is 166 degrees (traveling wave angle).

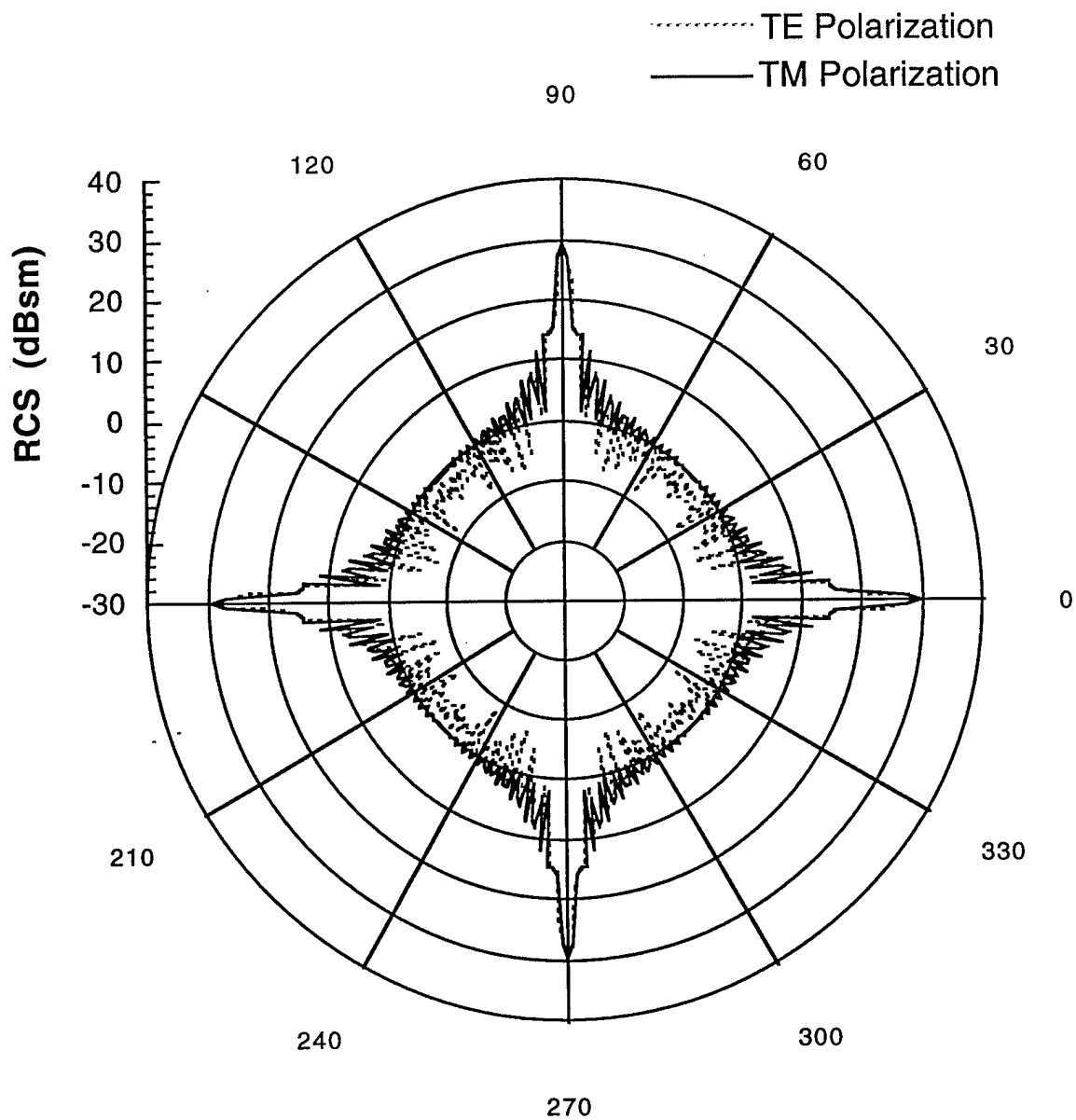


Figure B-17: Monostatic RCS of cylinder ( $r = 0.625$  in.) at 6 GHz.

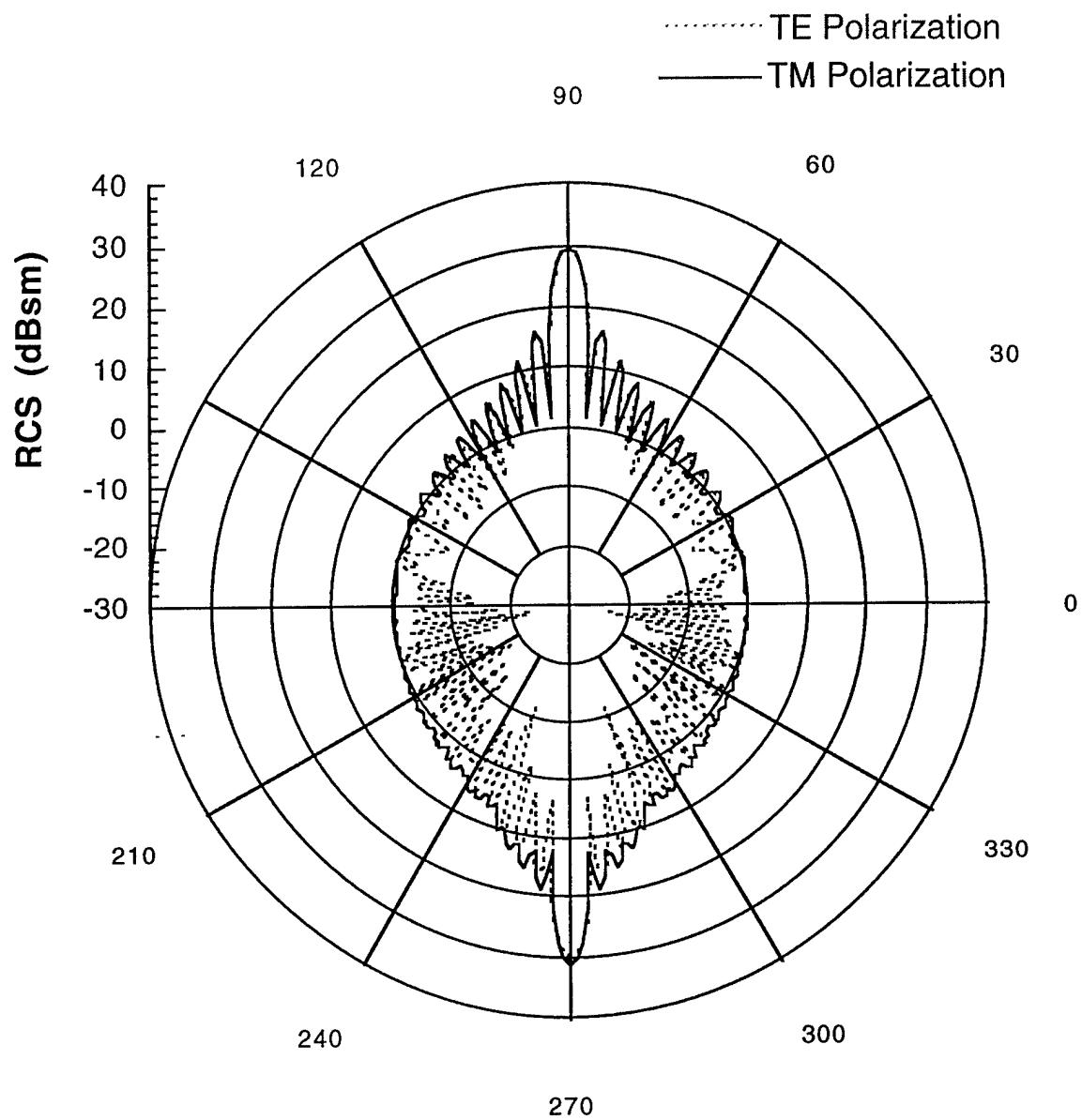


Figure B-18: Bistatic RCS of cylinder ( $r = 0.625$  in.) at 6 GHz: Incident angle is 90 degrees.

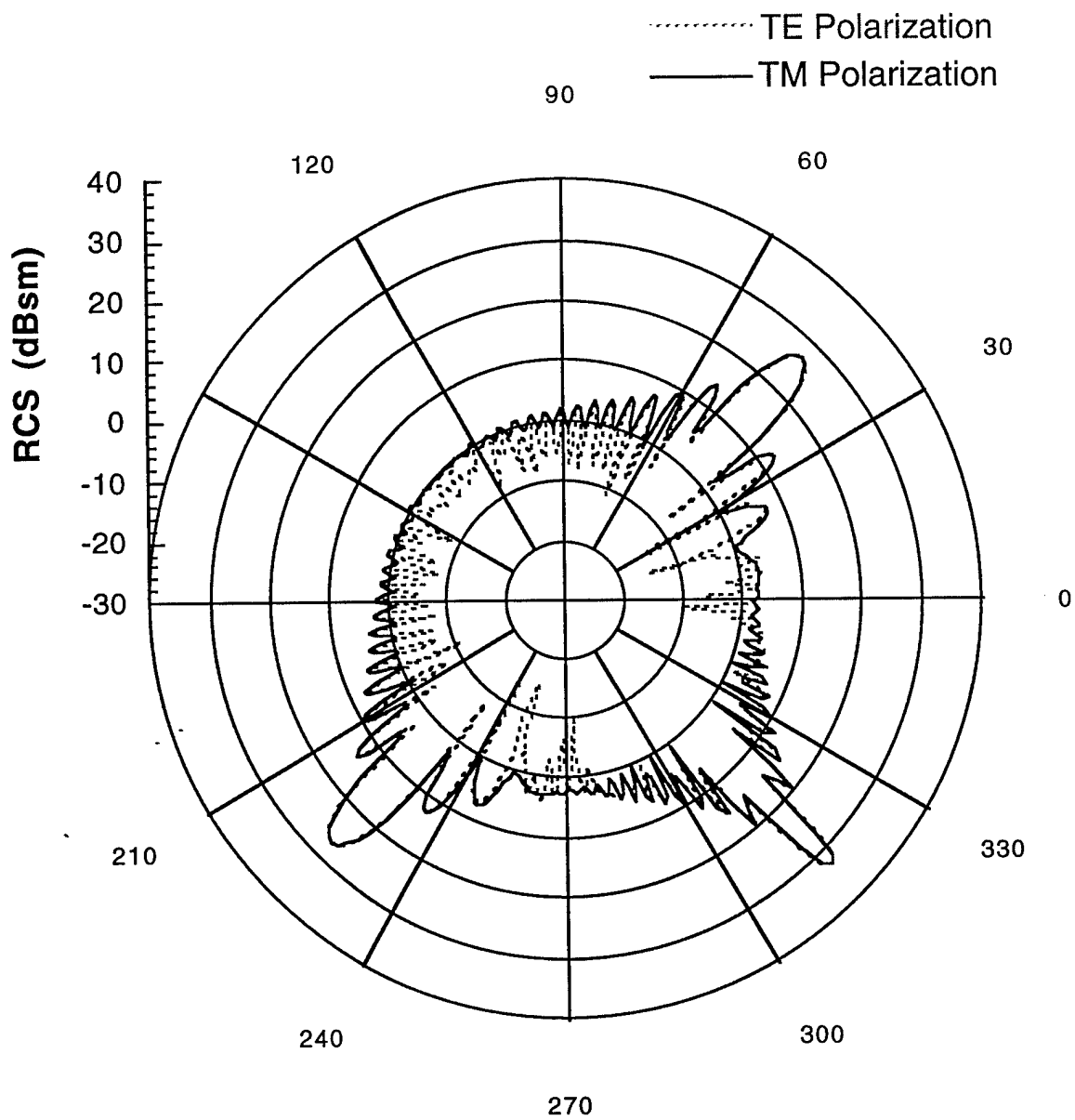


Figure B-19: Bistatic RCS of baseline cylinder ( $r = 0.625$  in.) at 6 GHz: Incident angle is 135 degrees.

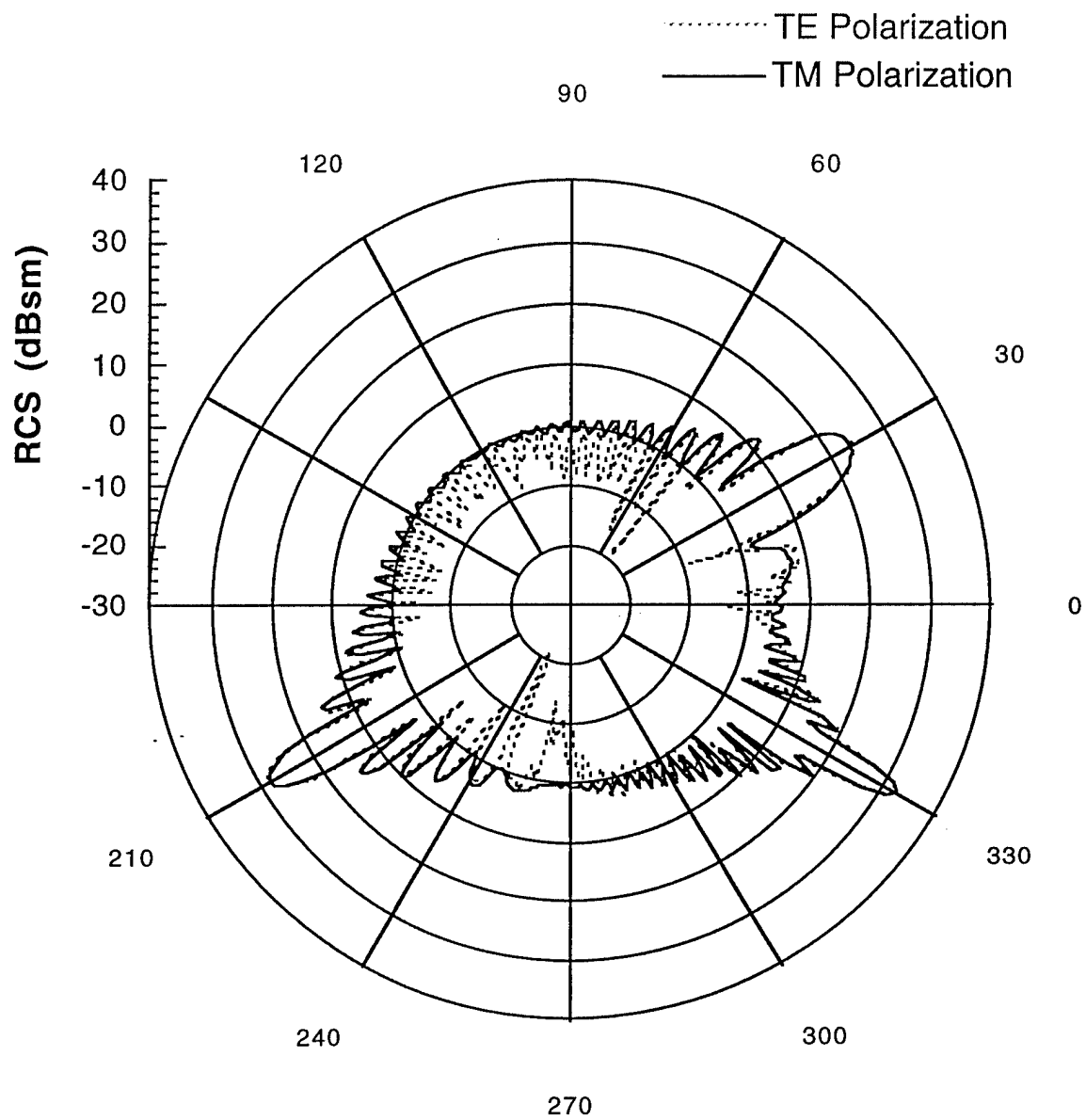


Figure B-20: Bistatic RCS of baseline cylinder ( $r = 0.625$  in.) at 6 GHz: Incident angle is 150 degrees.

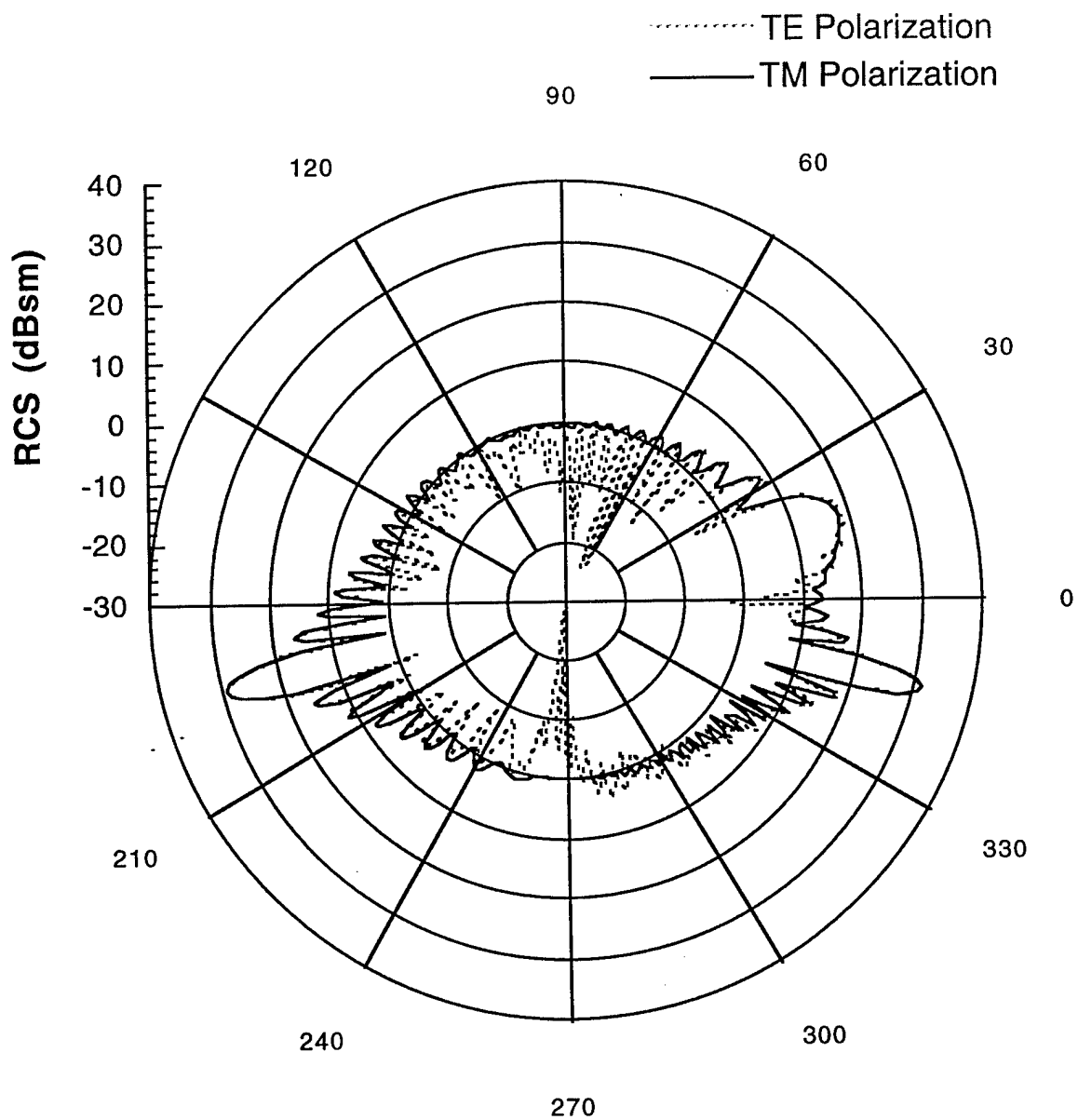


Figure B-21: Bistatic RCS of baseline cylinder ( $r = 0.625$  in.) at 6 GHz: Incident angle is 166 degrees (traveling wave angle).

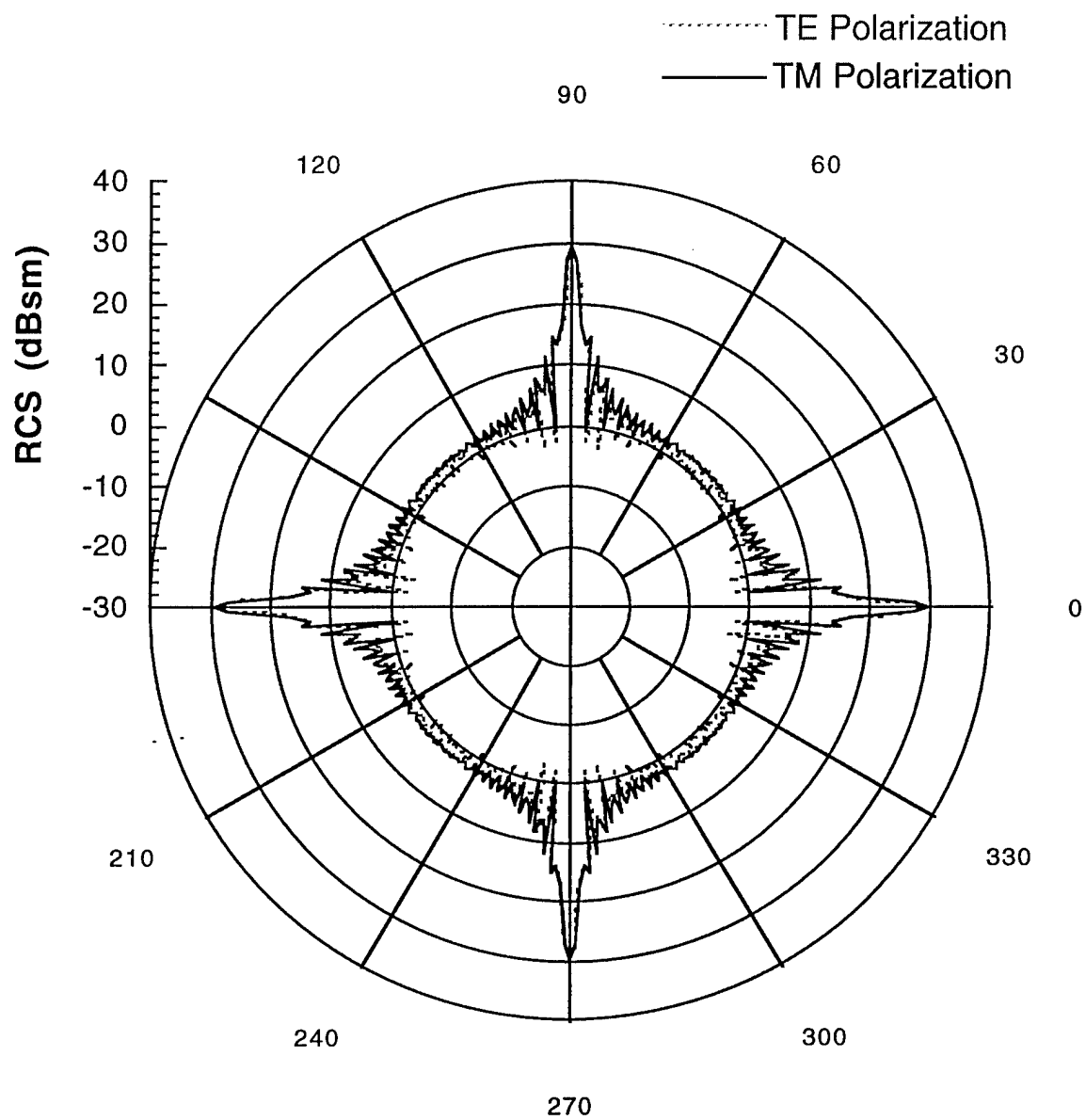


Figure B-22: Monostatic RCS of cylinder ( $r = 1.0$  in.) at 6 GHz

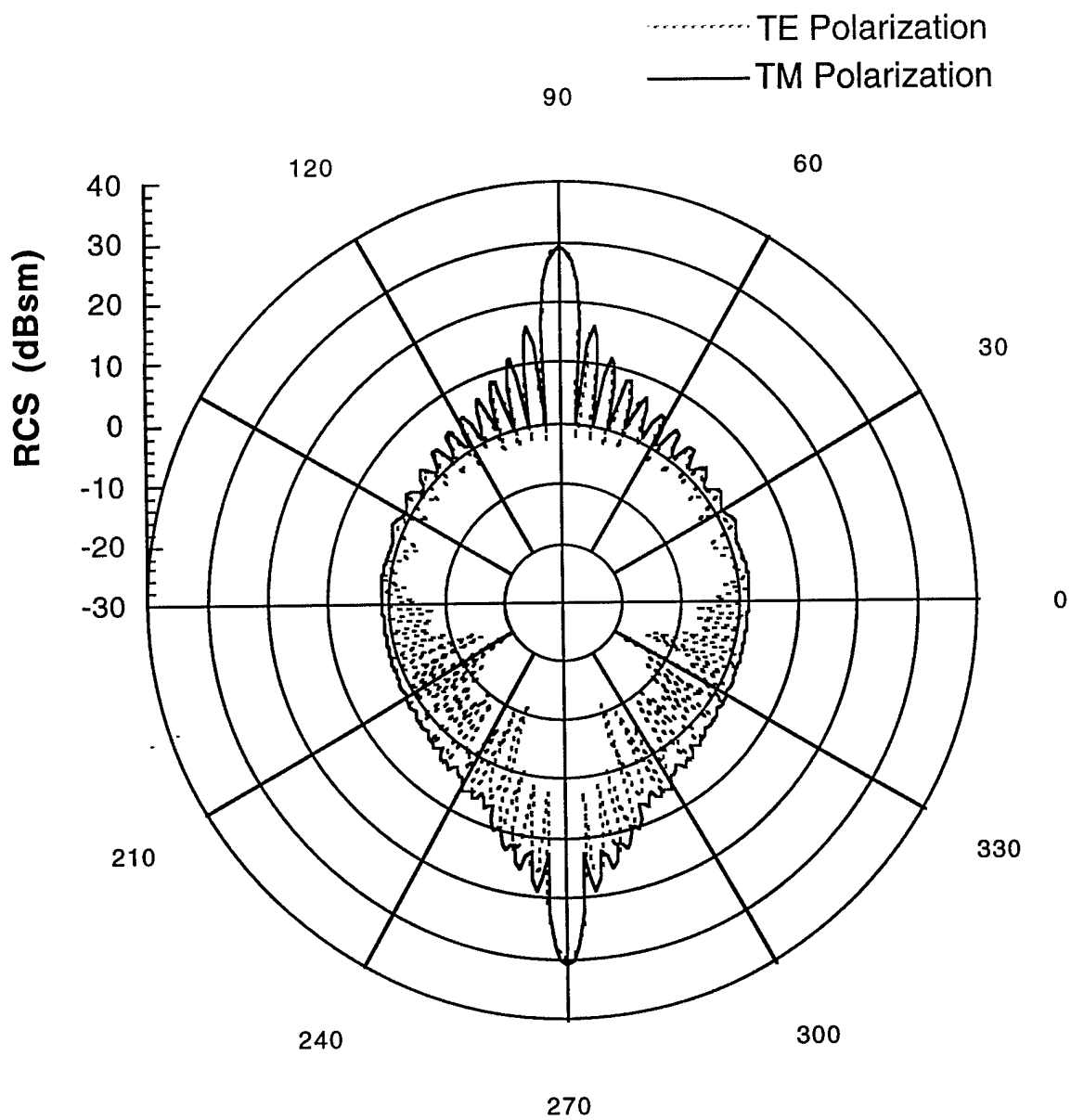


Figure B-23: Bistatic RCS of cylinder ( $r = 1.0$  in.) at 6 GHz: Incident angle is 90 degrees.



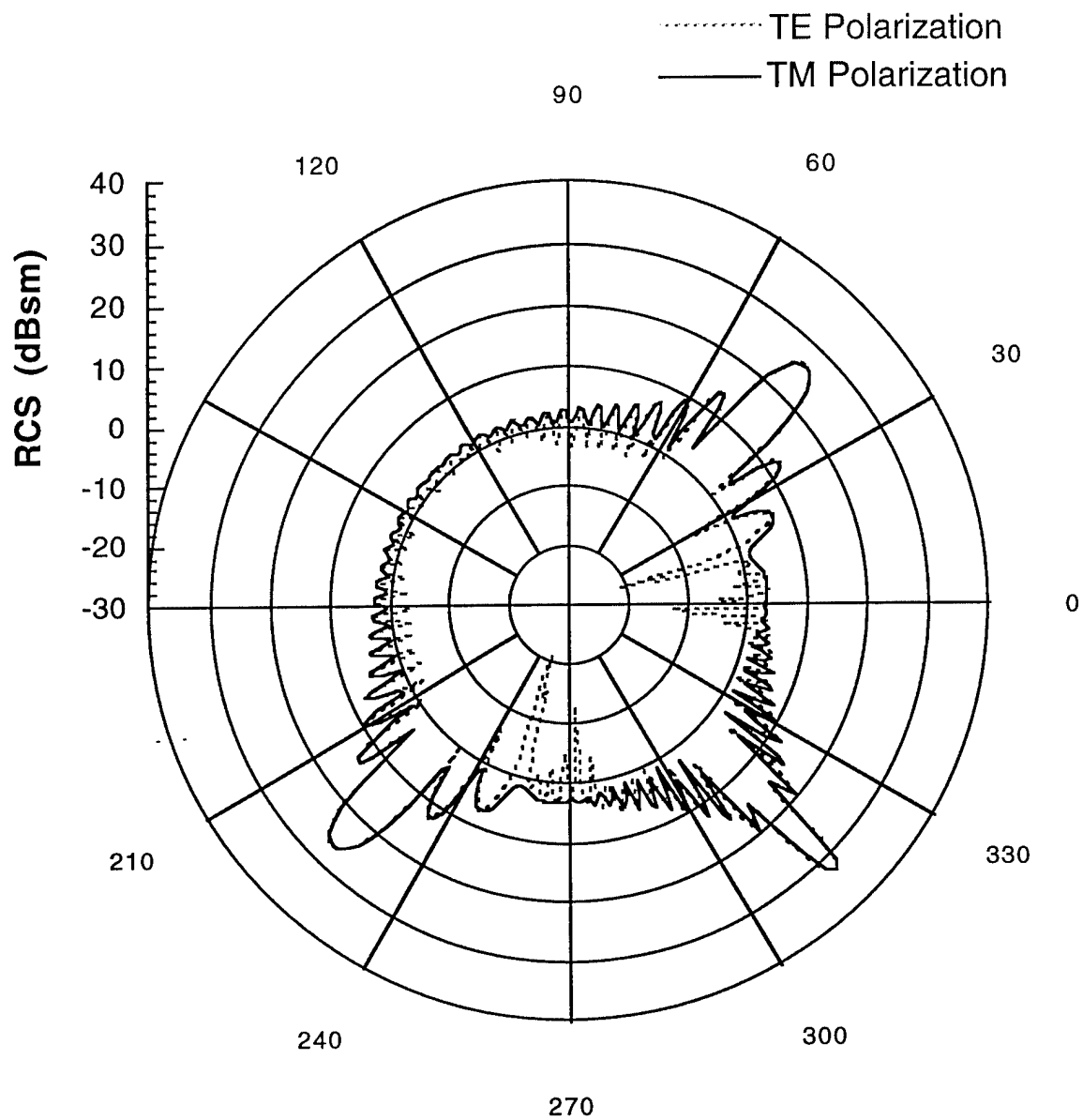


Figure B-24: Bistatic RCS of baseline cylinder ( $r = 1.0$  in.) at 6 GHz: Incident angle is 135 degrees.

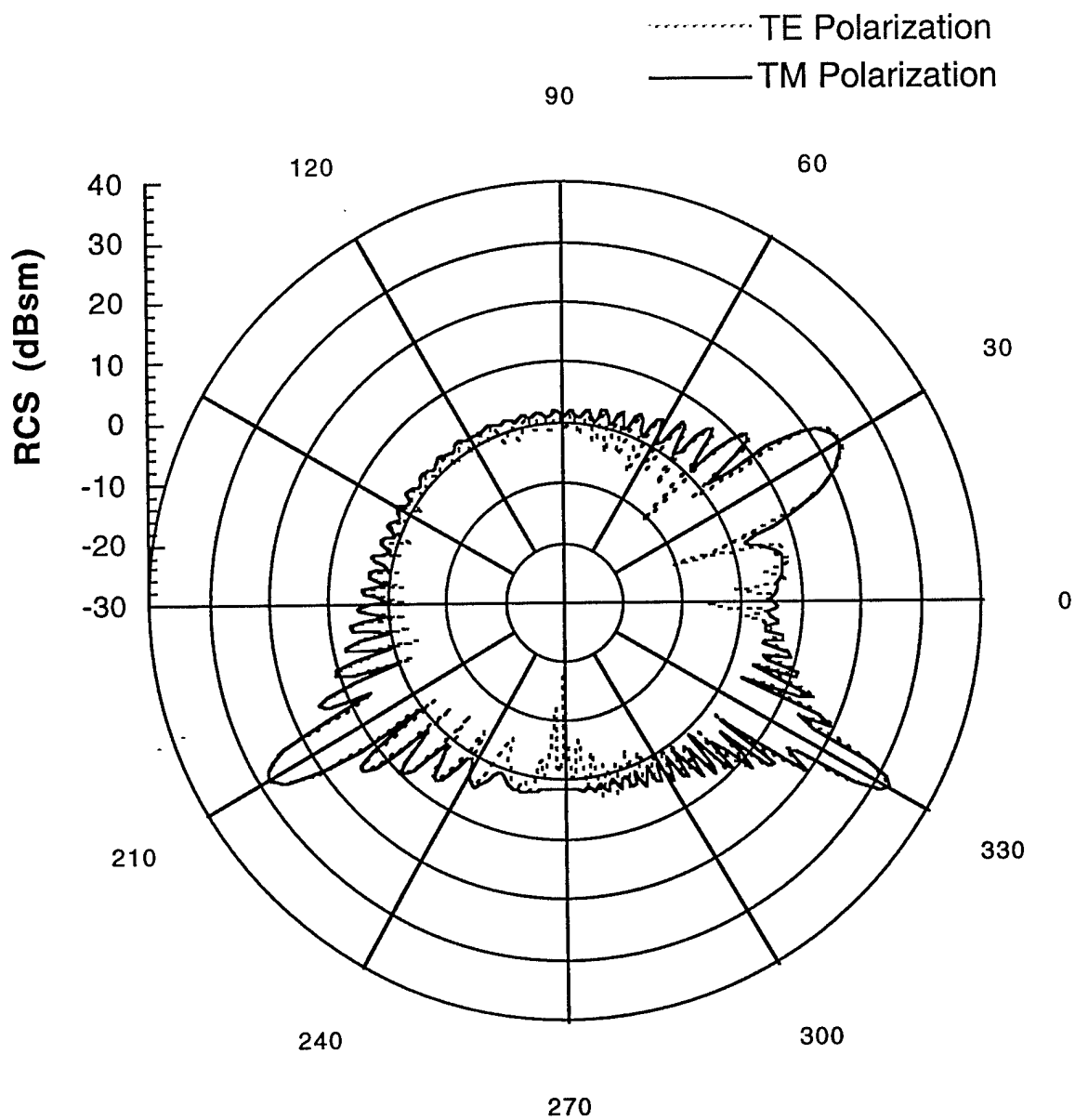


Figure B-25: Bistatic RCS of baseline cylinder ( $r = 1.0$  in.) at 6 GHz: Incident angle is 150 degrees.

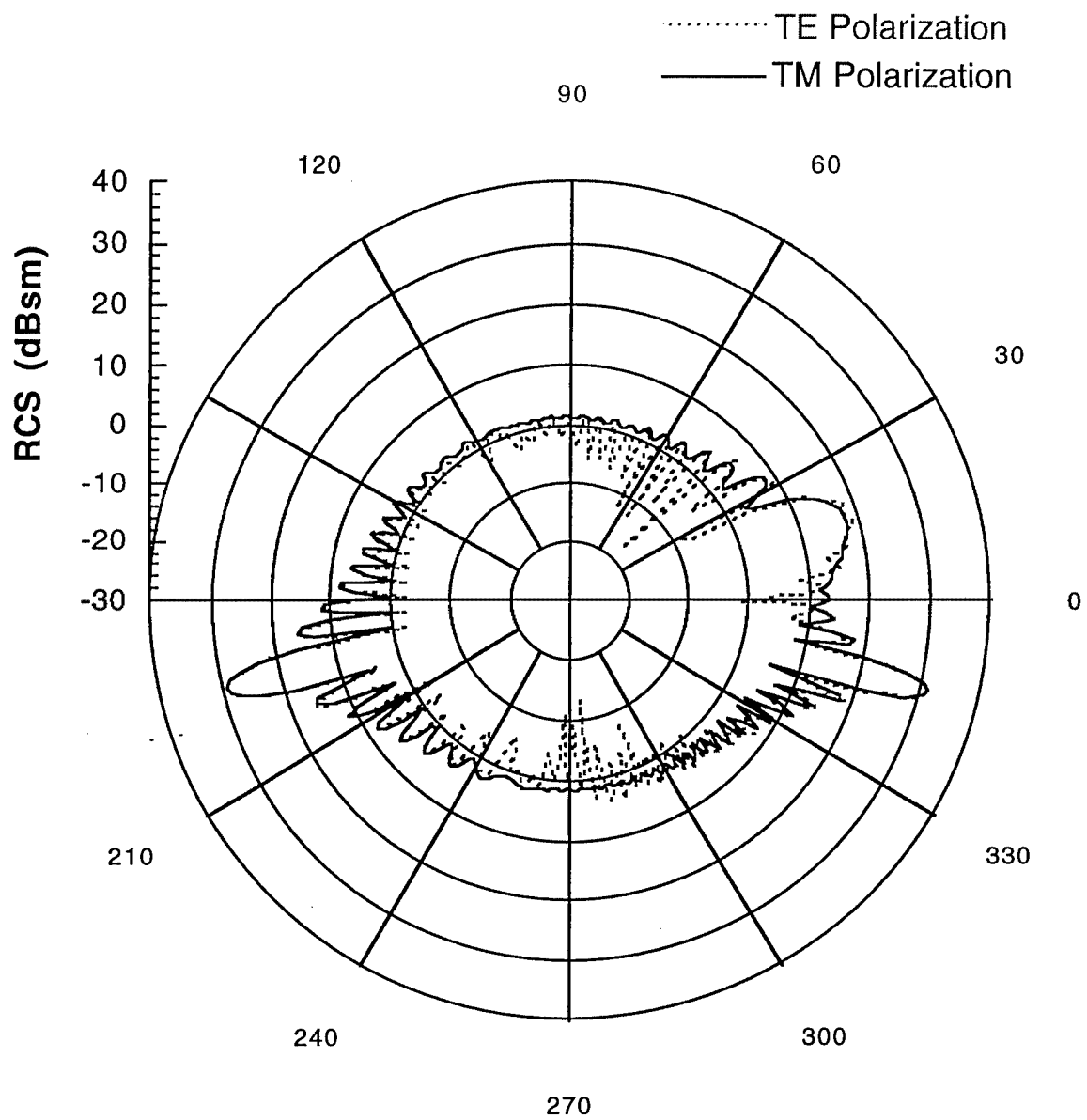


Figure B-26: Bistatic RCS of baseline cylinder ( $r = 1.0$  in.) at 6 GHz: Incident angle is 166 degrees (traveling wave angle).

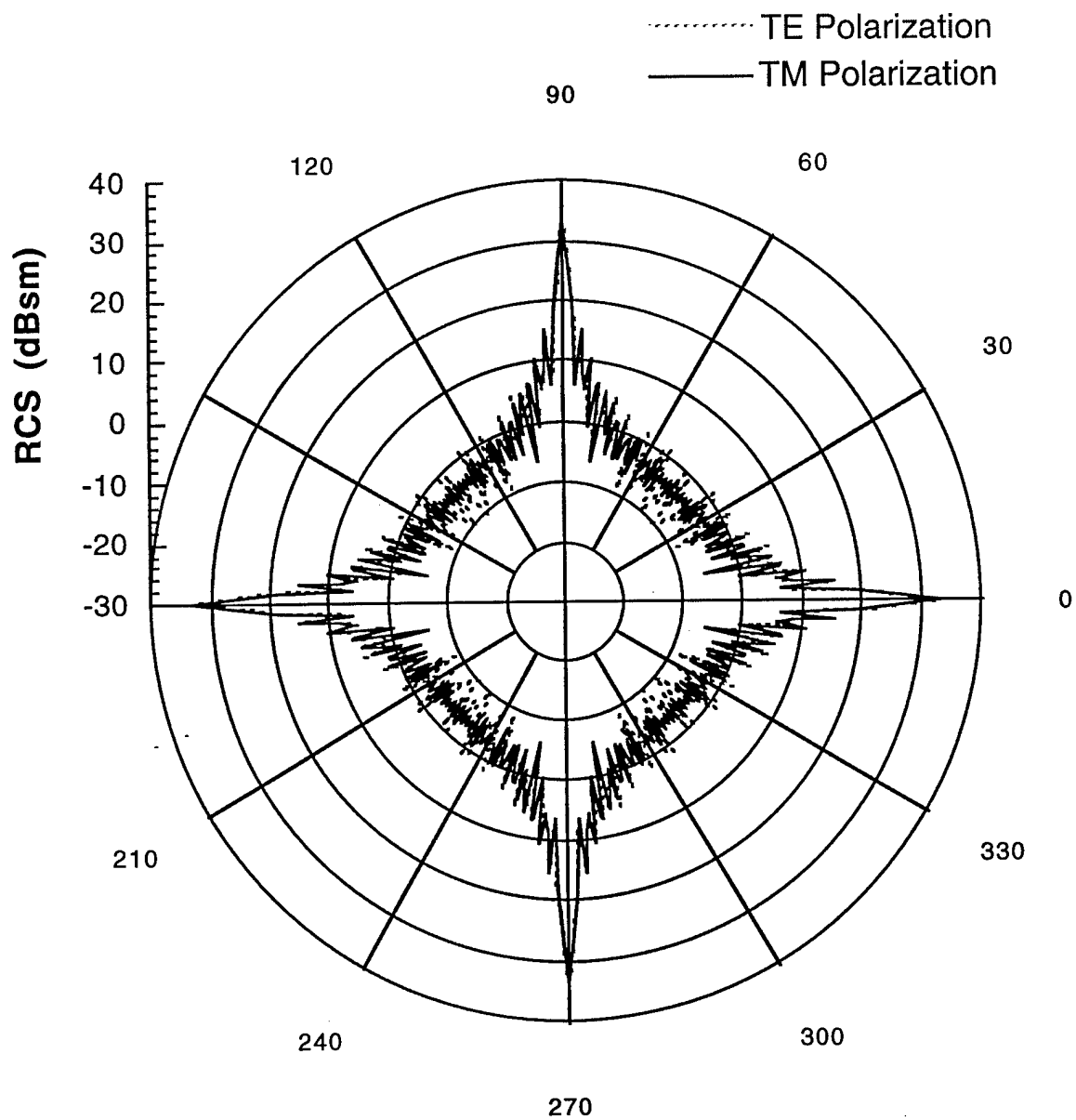


Figure B-27: Monostatic RCS of baseline cylinder at 9 GHz

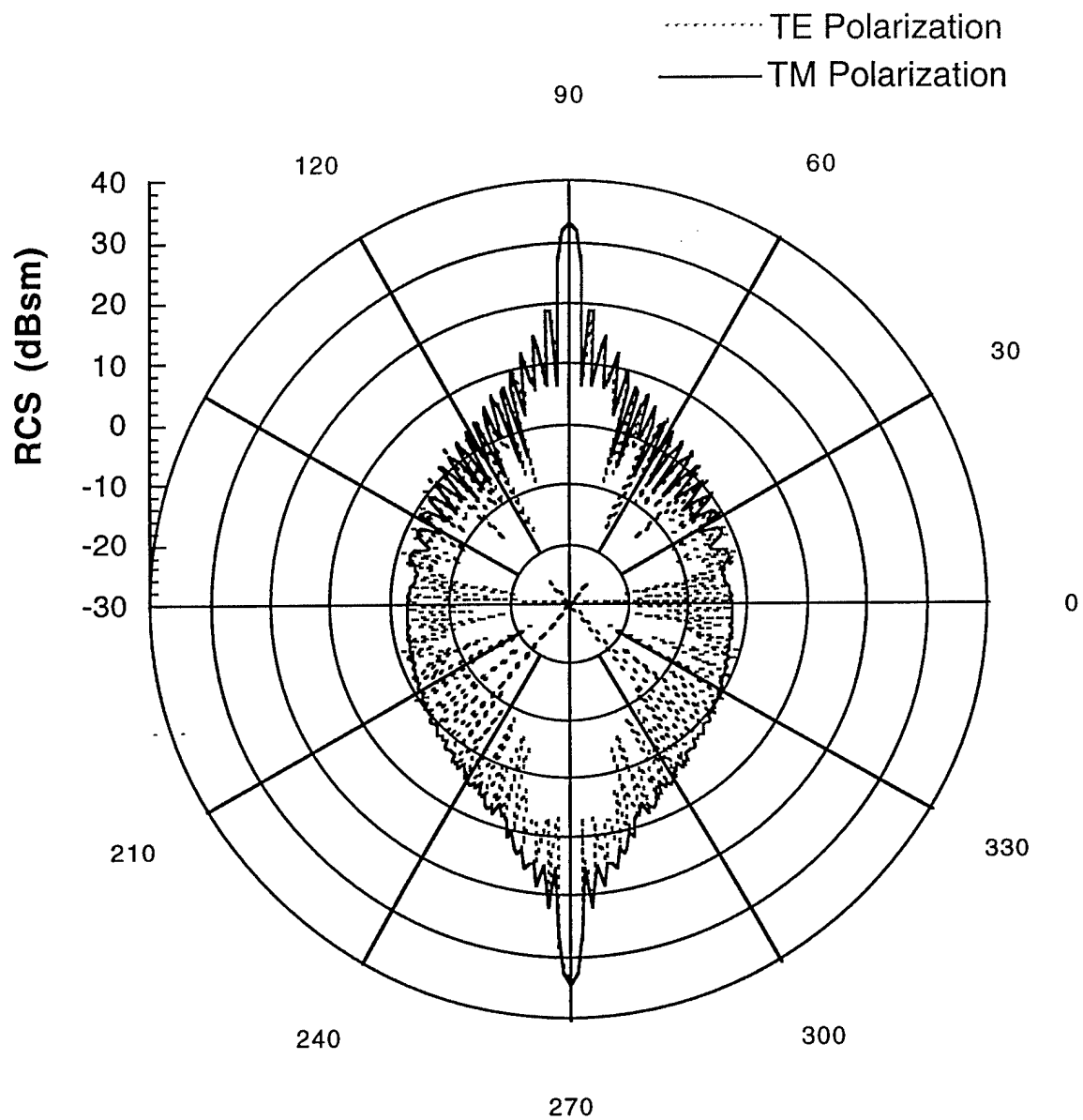


Figure B-28: Bistatic RCS of baseline cylinder at 9 GHz: Incident angle is 90 degrees.

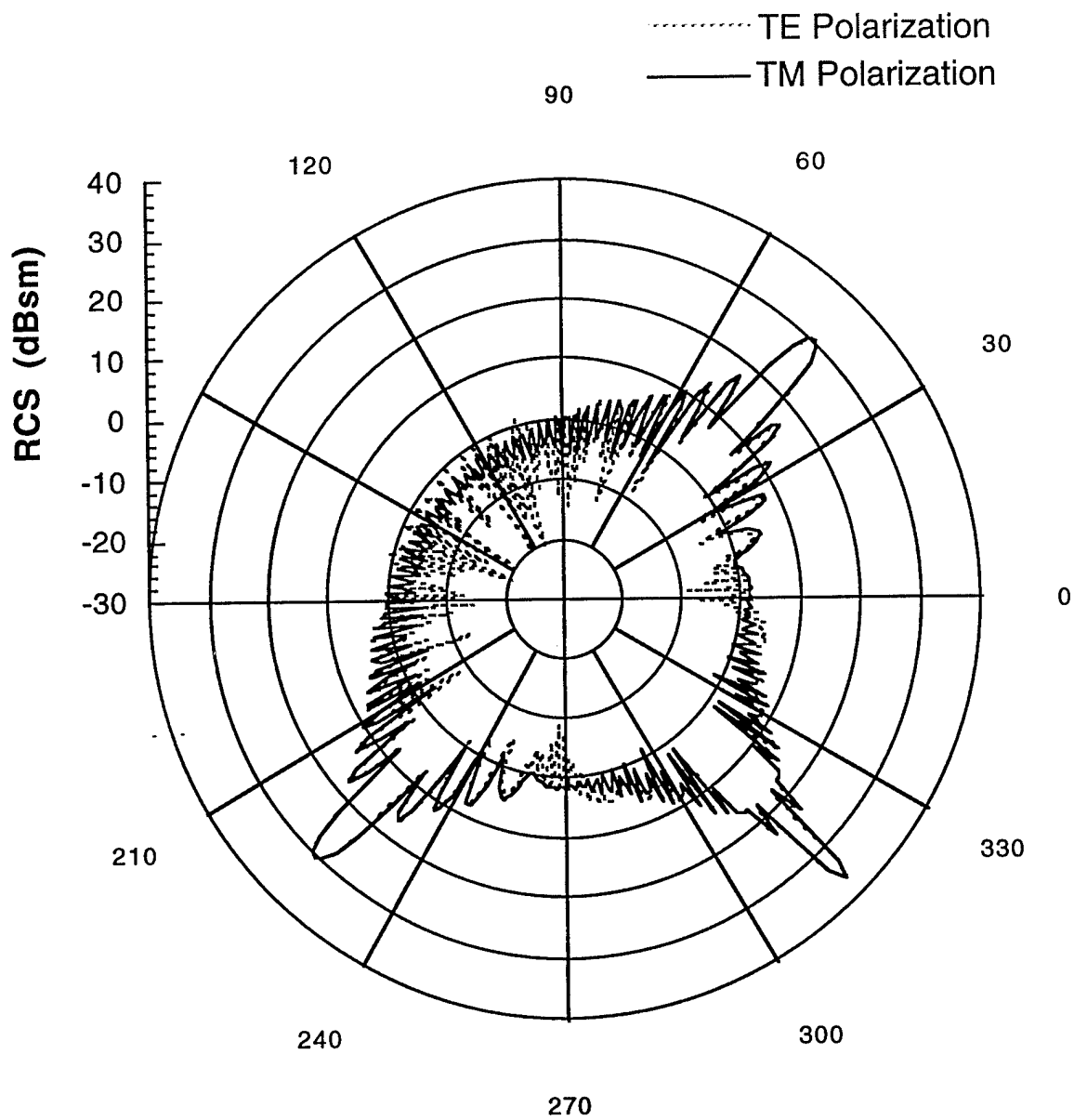


Figure B-29: Bistatic RCS of baseline cylinder at 9 GHz: Incident angle is 135 degrees.

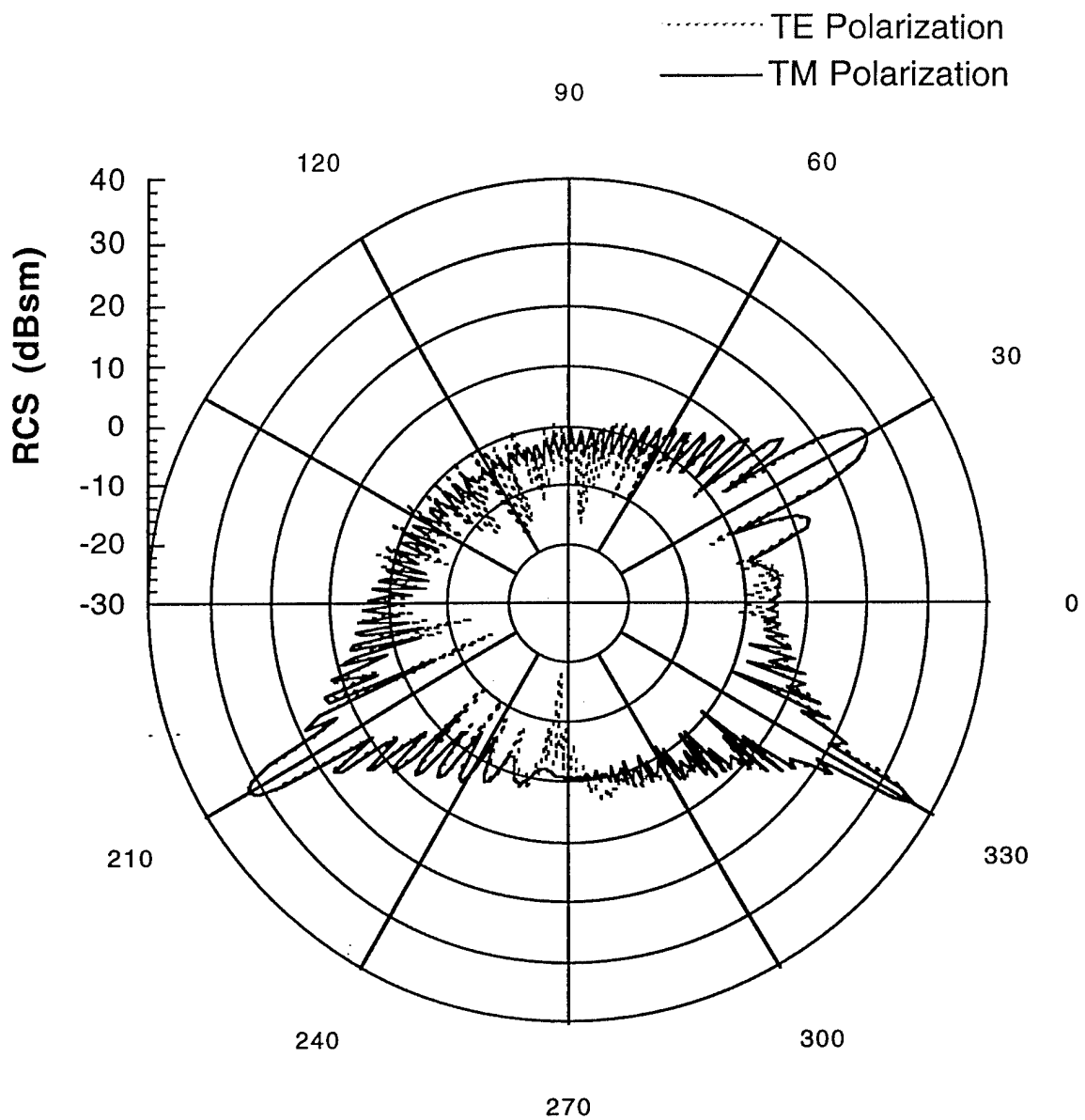


Figure B-30: Bistatic RCS of baseline cylinder at 9 GHz: Incident angle is 150 degrees.

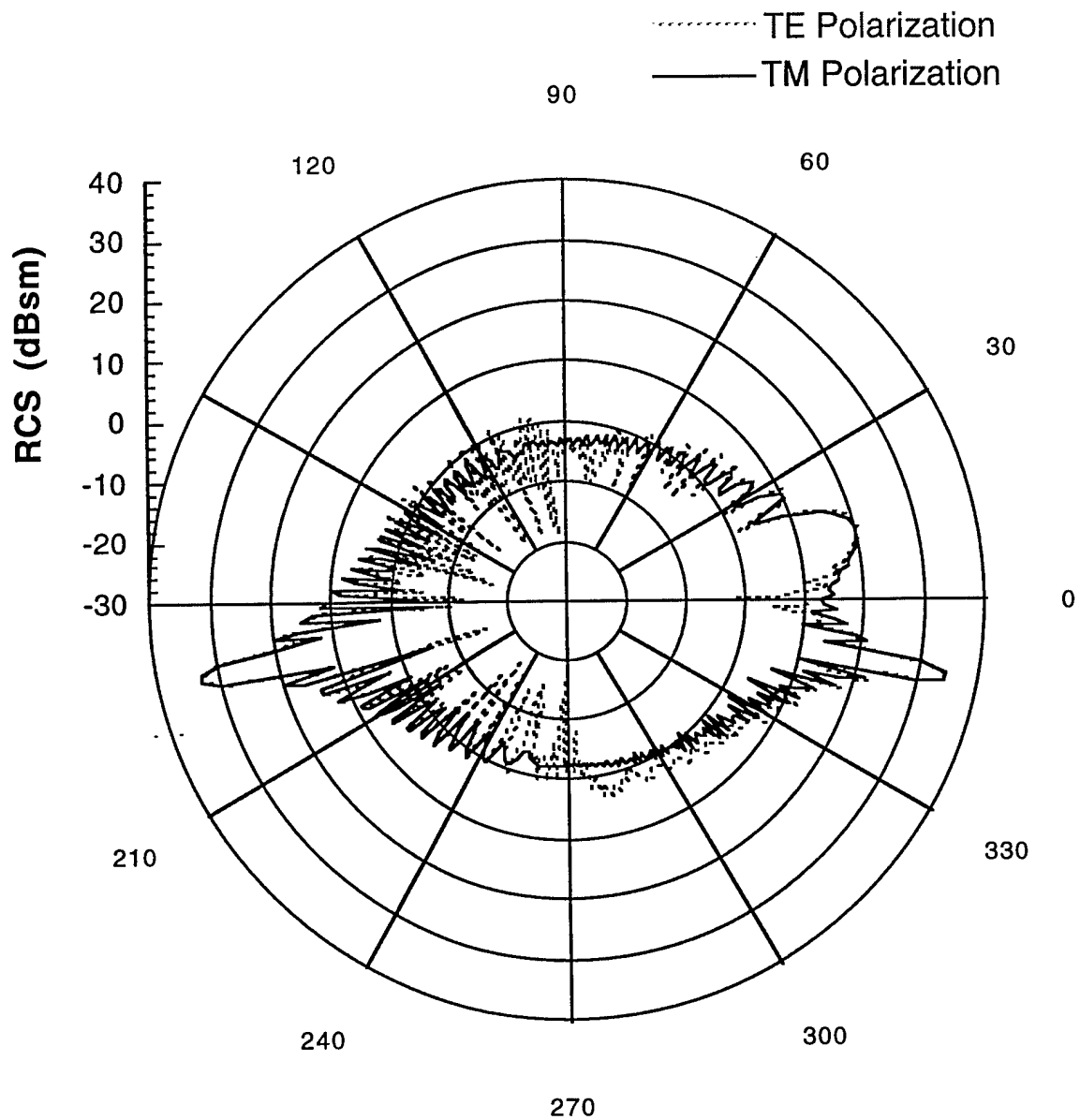


Figure B-31: Bistatic RCS of baseline cylinder at 9 GHz: Incident angle is 168 degrees (traveling wave angle).



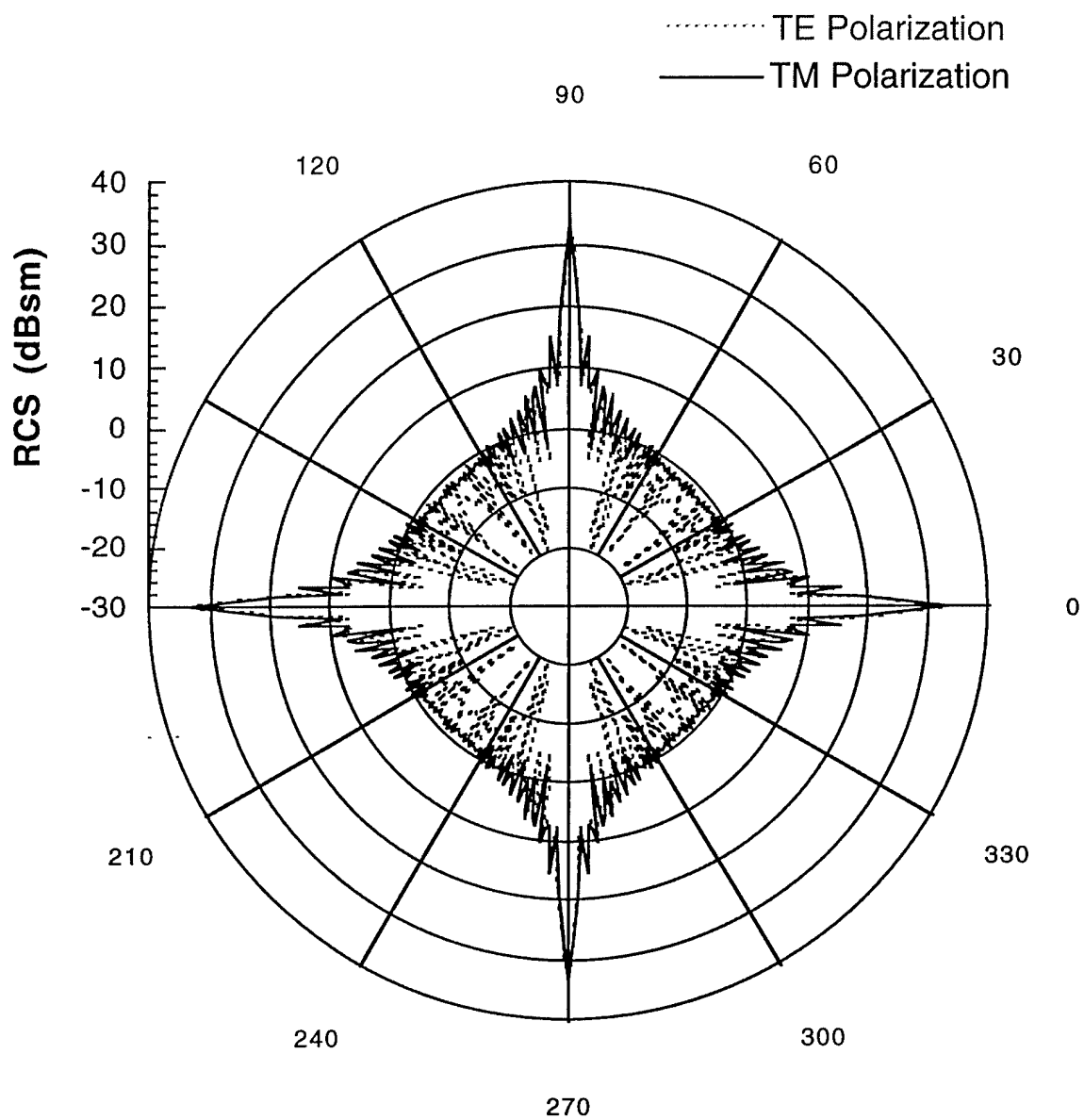


Figure B-32: Monostatic RCS of cylinder ( $r = 0.25$  in.) at 9 GHz

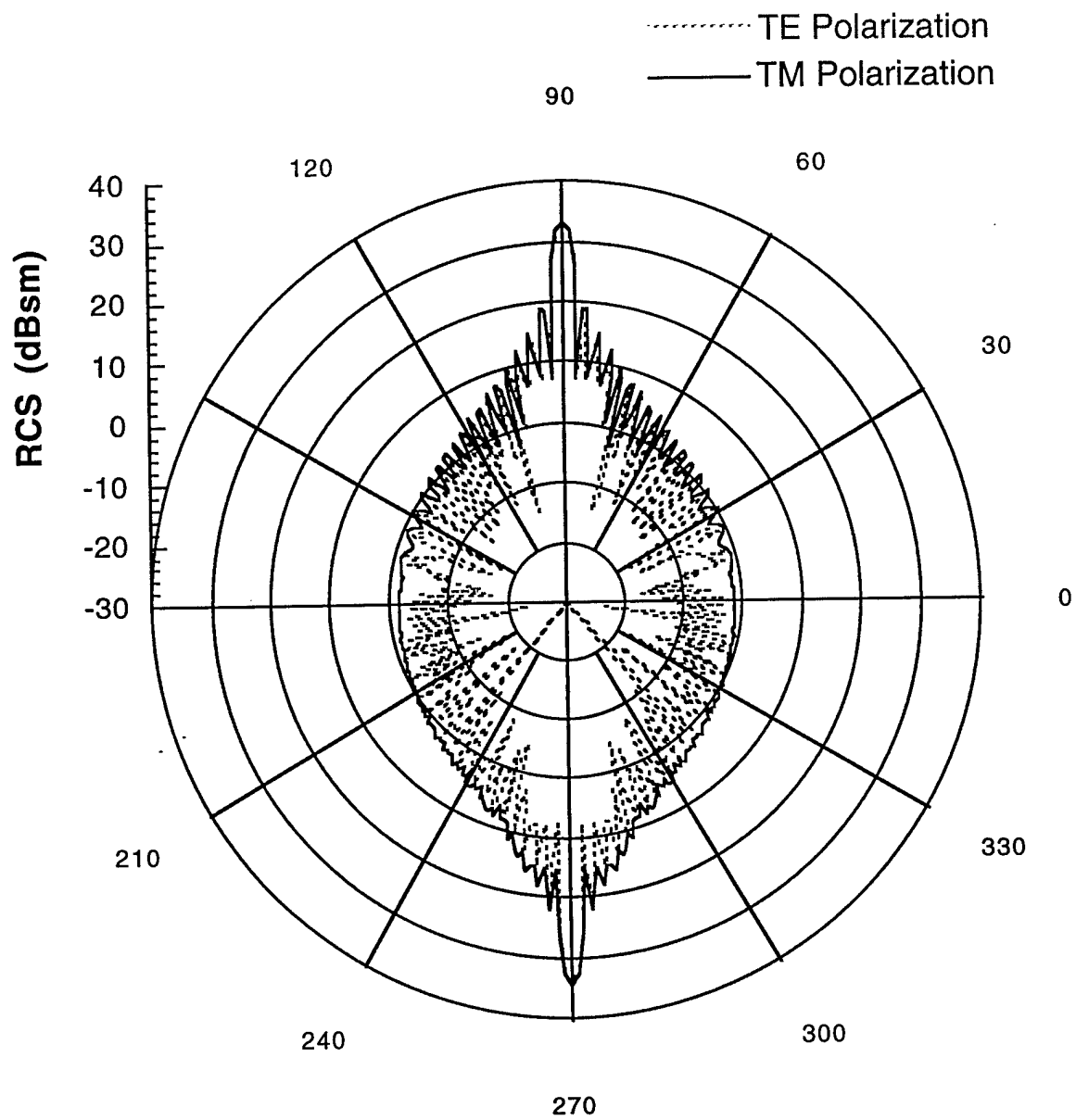


Figure B-33: Bistatic RCS of cylinder ( $r = 0.25$  in.) at 9 GHz: Incident angle is 90 degrees.

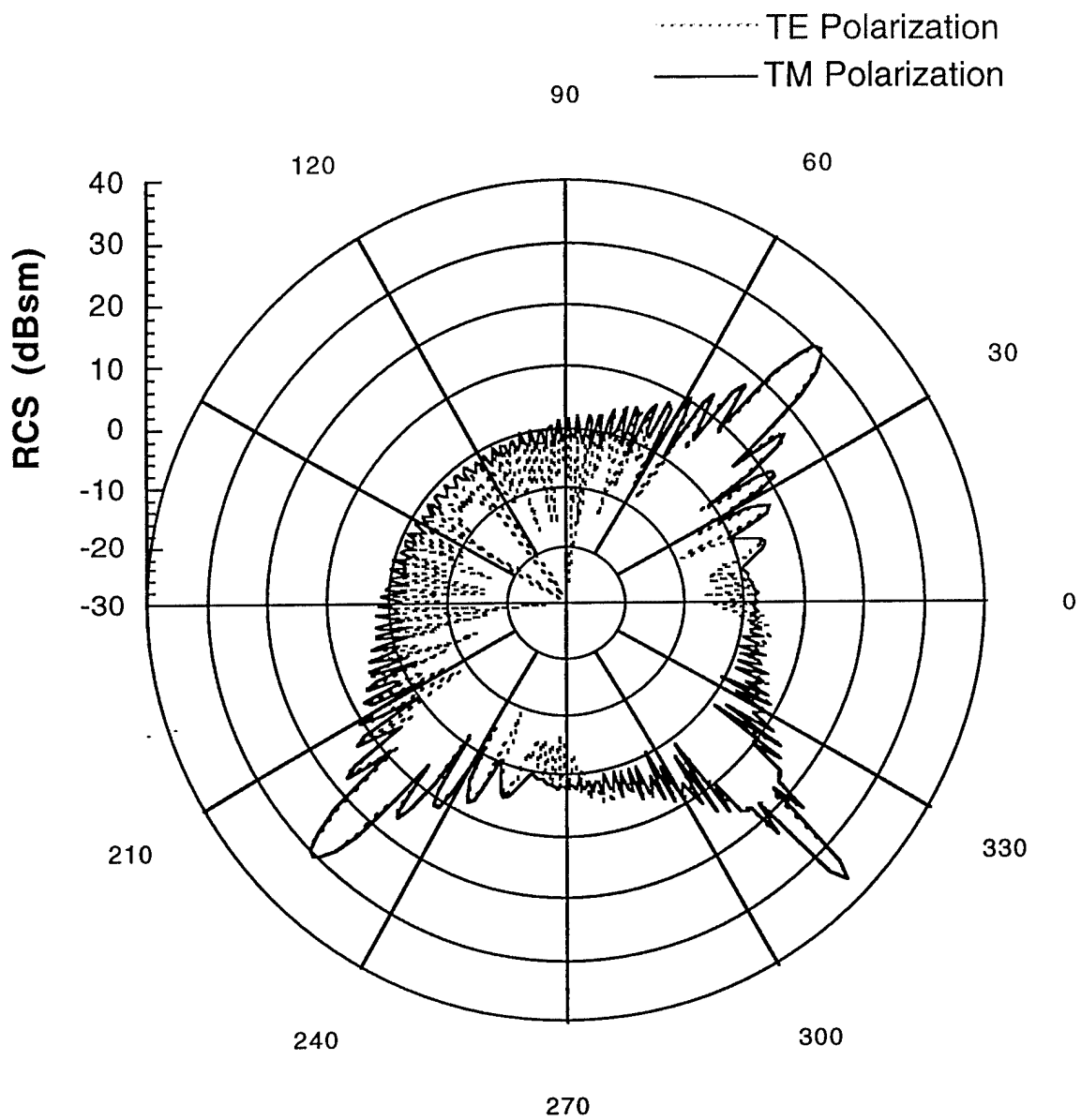


Figure B-34: Bistatic RCS of baseline cylinder ( $r = 0.25$  in.) at 9 GHz: Incident angle is 135 degrees.

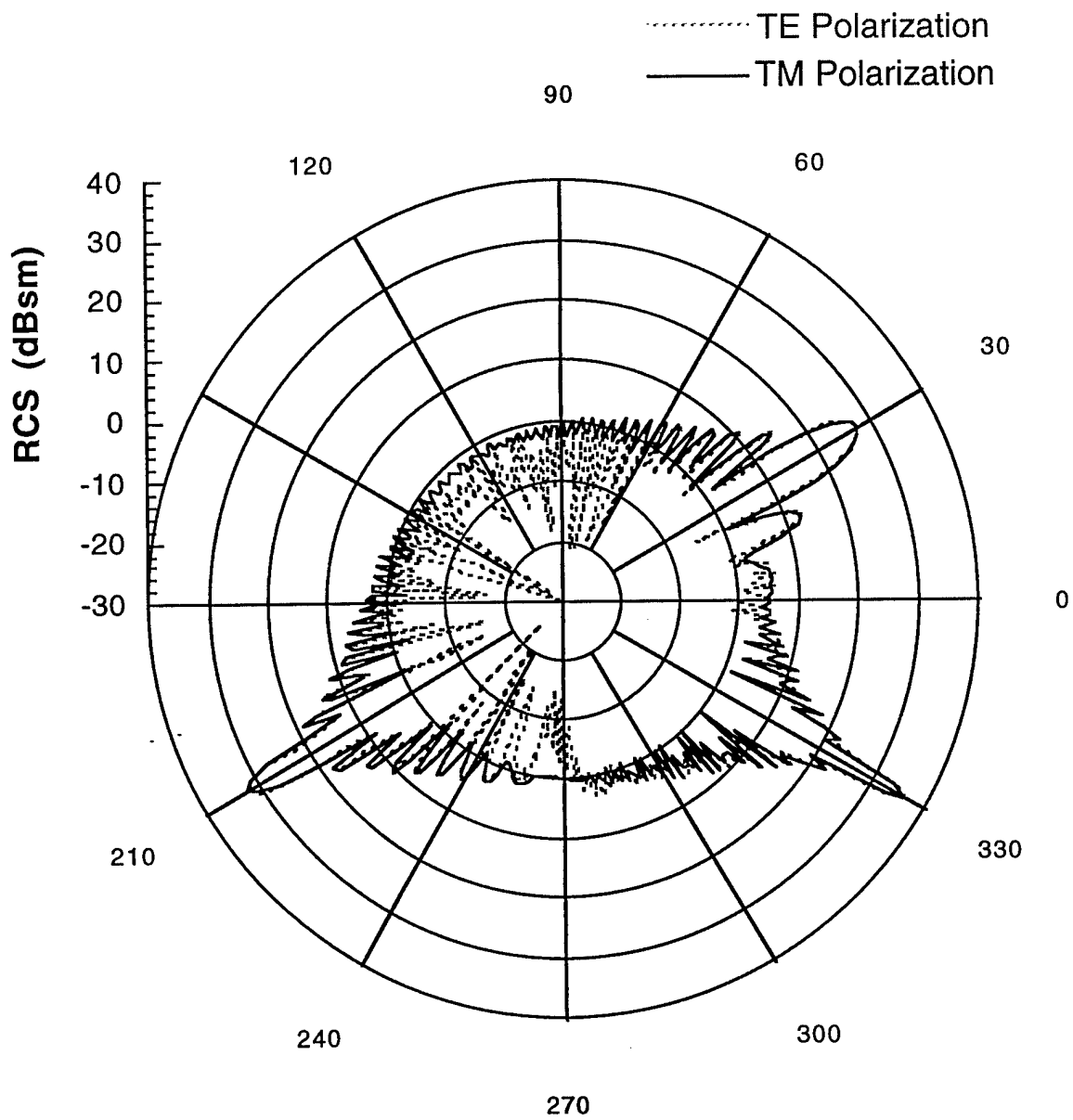


Figure B-35: Bistatic RCS of baseline cylinder ( $r = 0.25$  in.) at 9 GHz: Incident angle is 150 degrees.

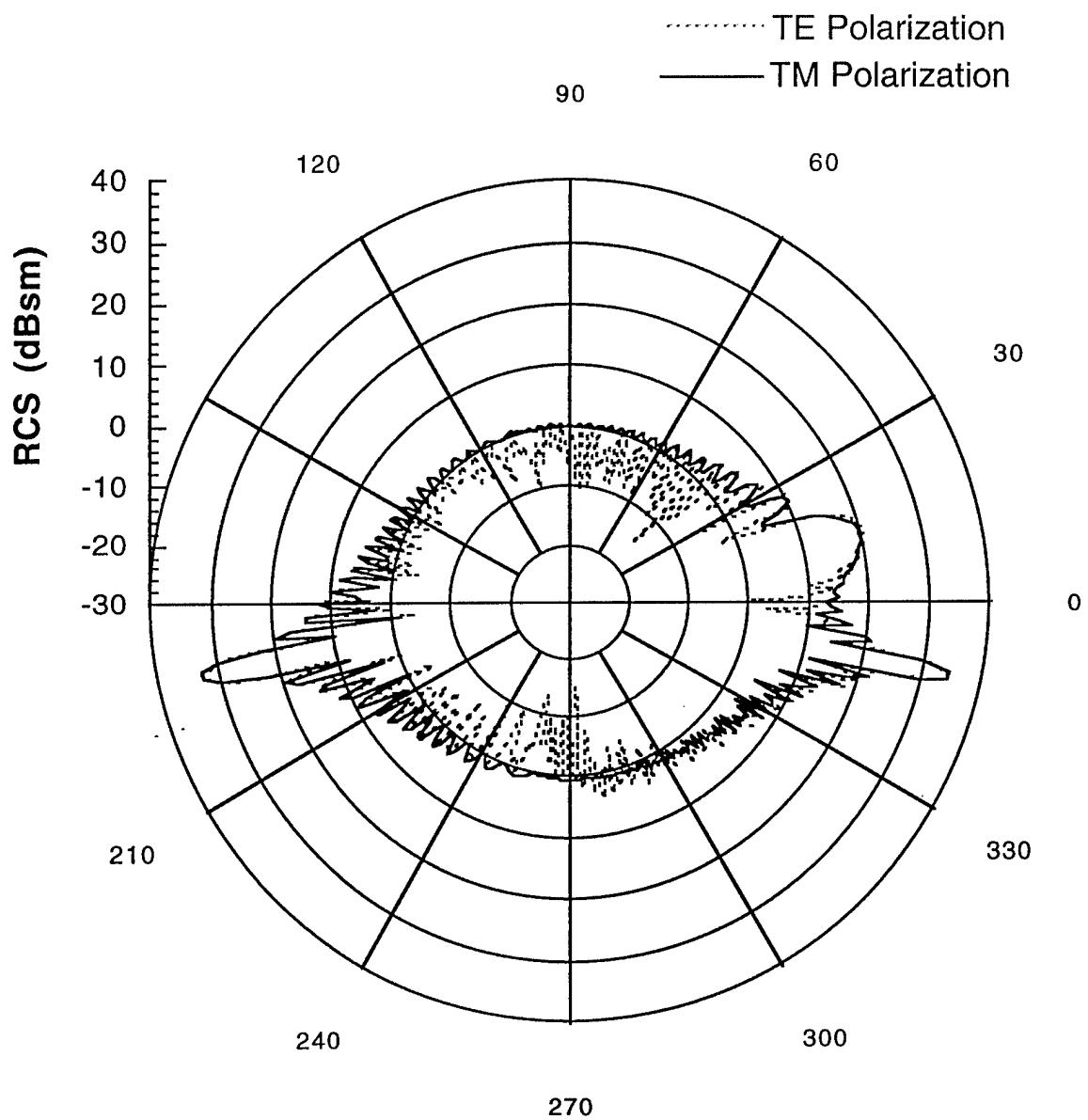


Figure B-36: Bistatic RCS of baseline cylinder ( $r = 0.25$  in.) at 9 GHz: Incident angle is 168 degrees (traveling wave angle).

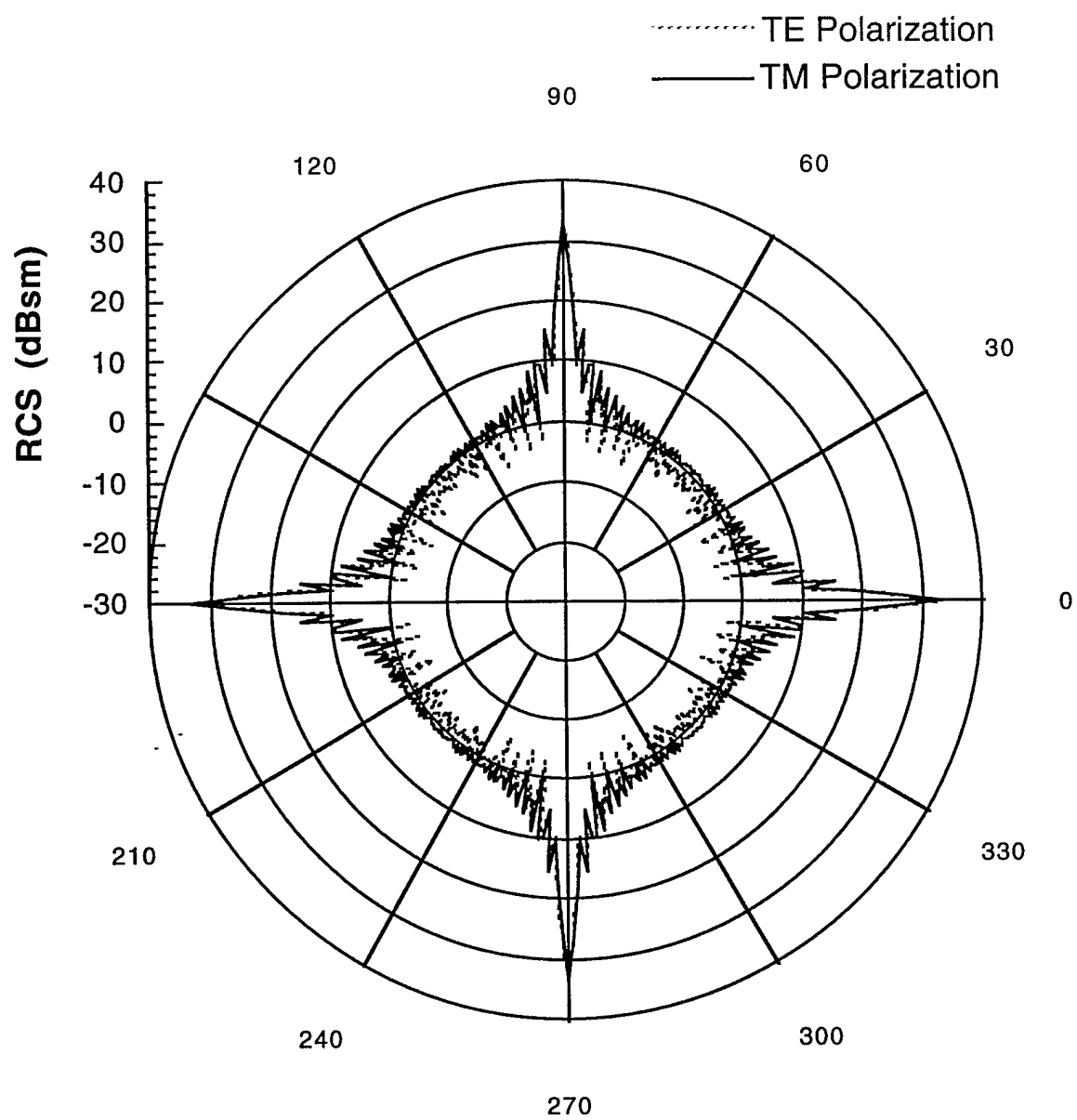


Figure B-37: Monostatic RCS of cylinder ( $r = 0.5$  in.) at 9 GHz

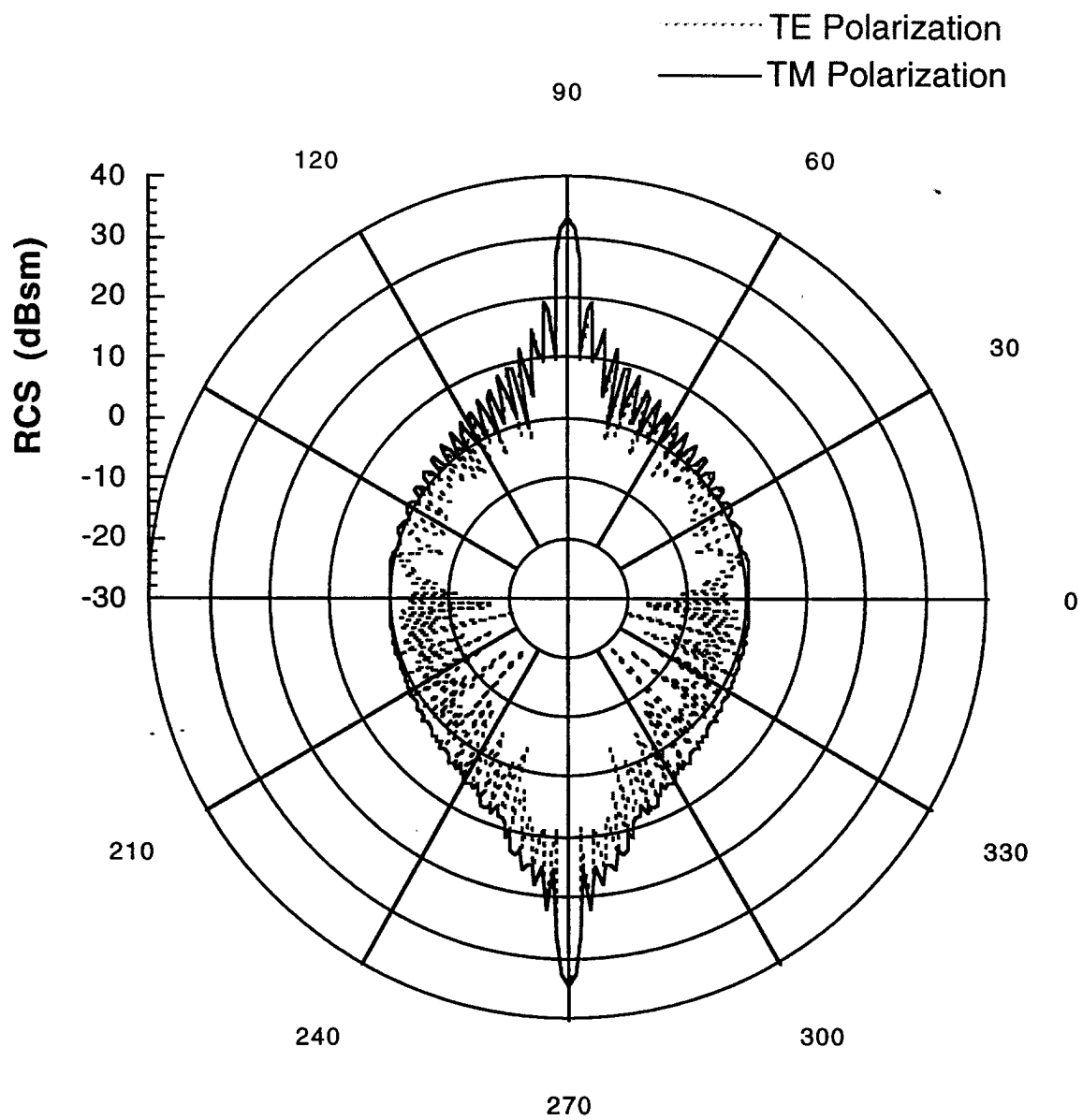


Figure B-38: Bistatic RCS of cylinder ( $r = 0.5$  in.) at 9 GHz: Incident angle is 90 degrees.

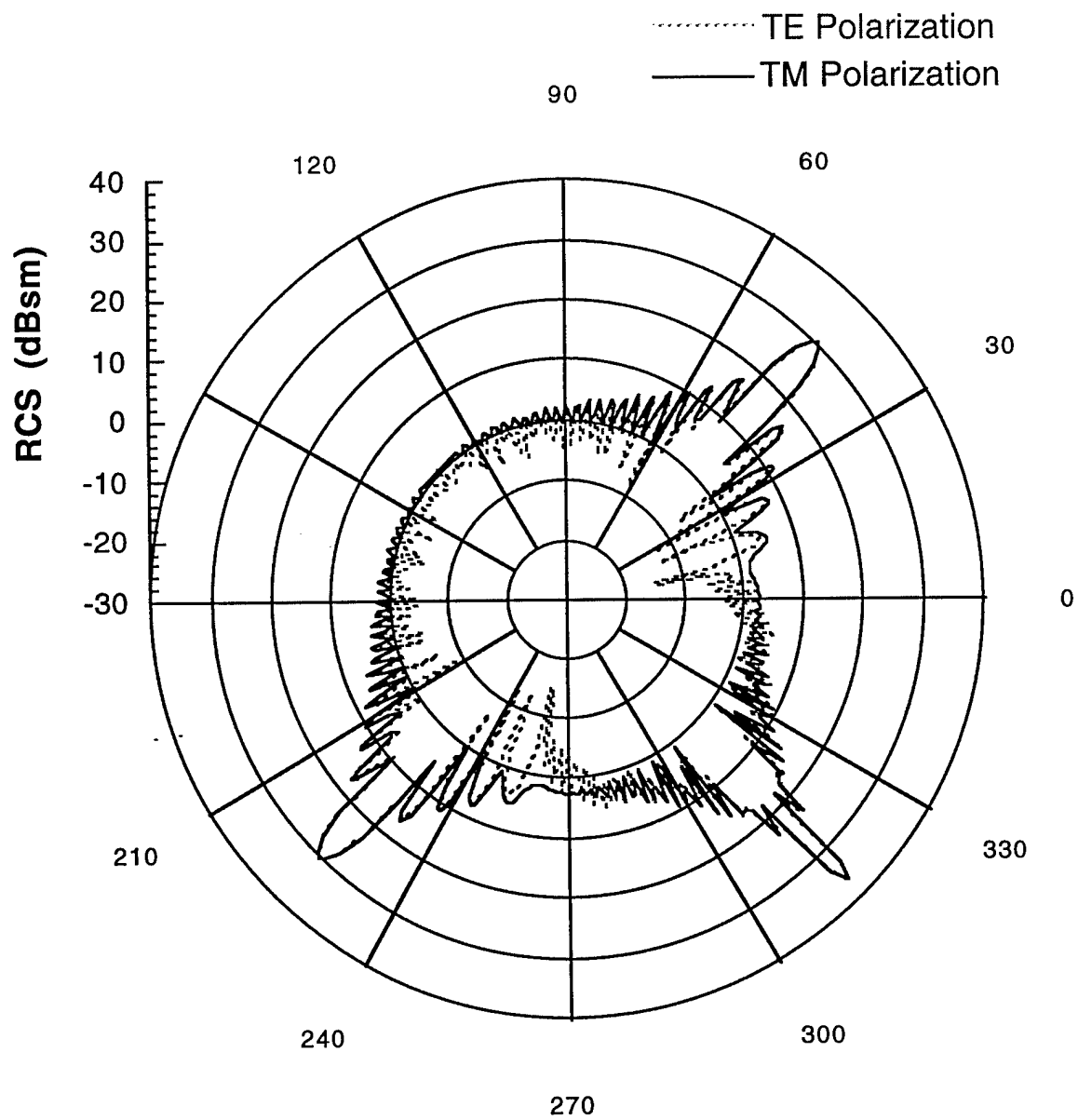


Figure B-39: Bistatic RCS of baseline cylinder ( $r = 0.5$  in.) at 9 GHz: Incident angle is 135 degrees.



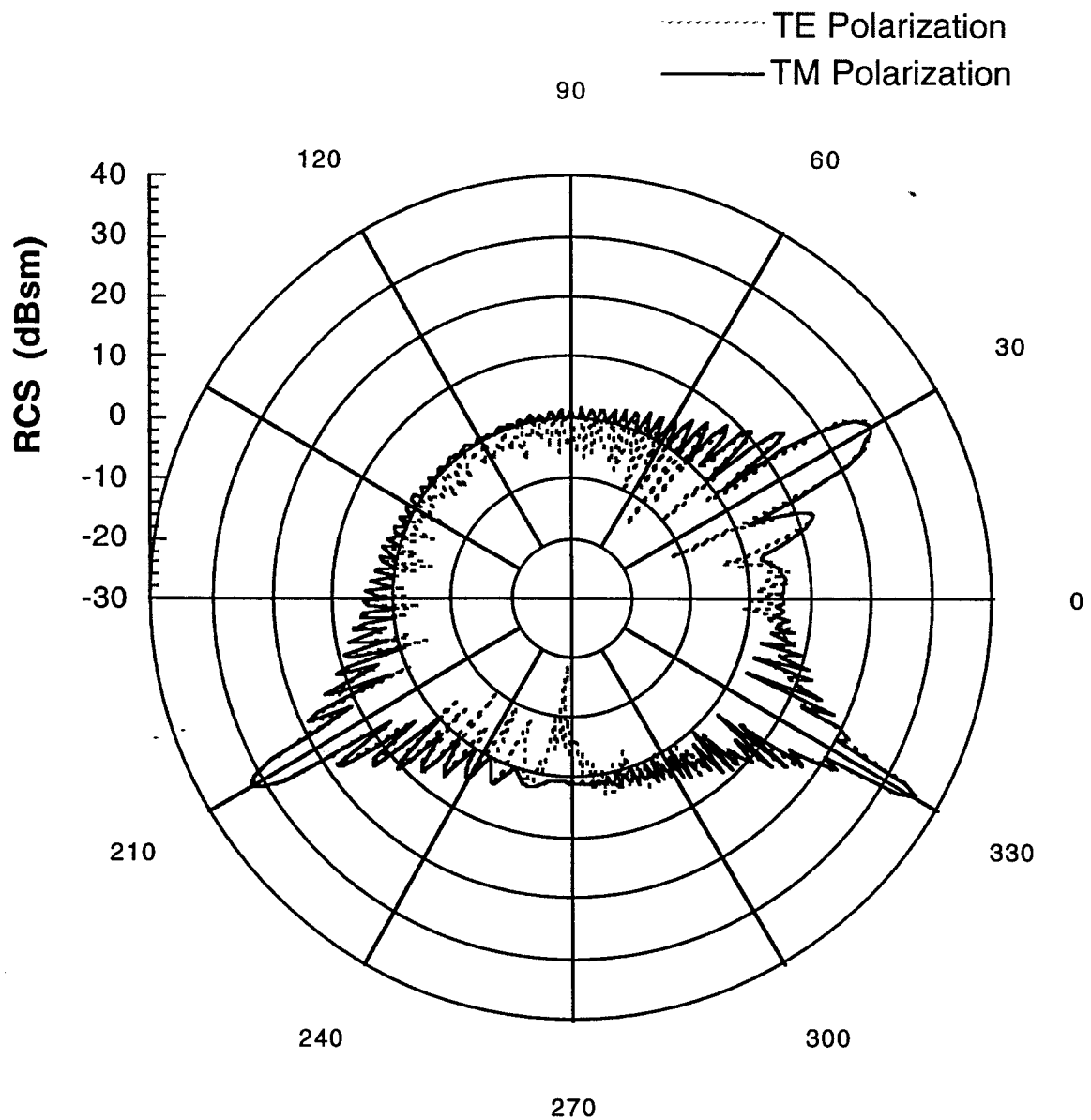


Figure B-40: Bistatic RCS of baseline cylinder ( $r = 0.5$  in.) at 9 GHz: Incident angle is 150 degrees.

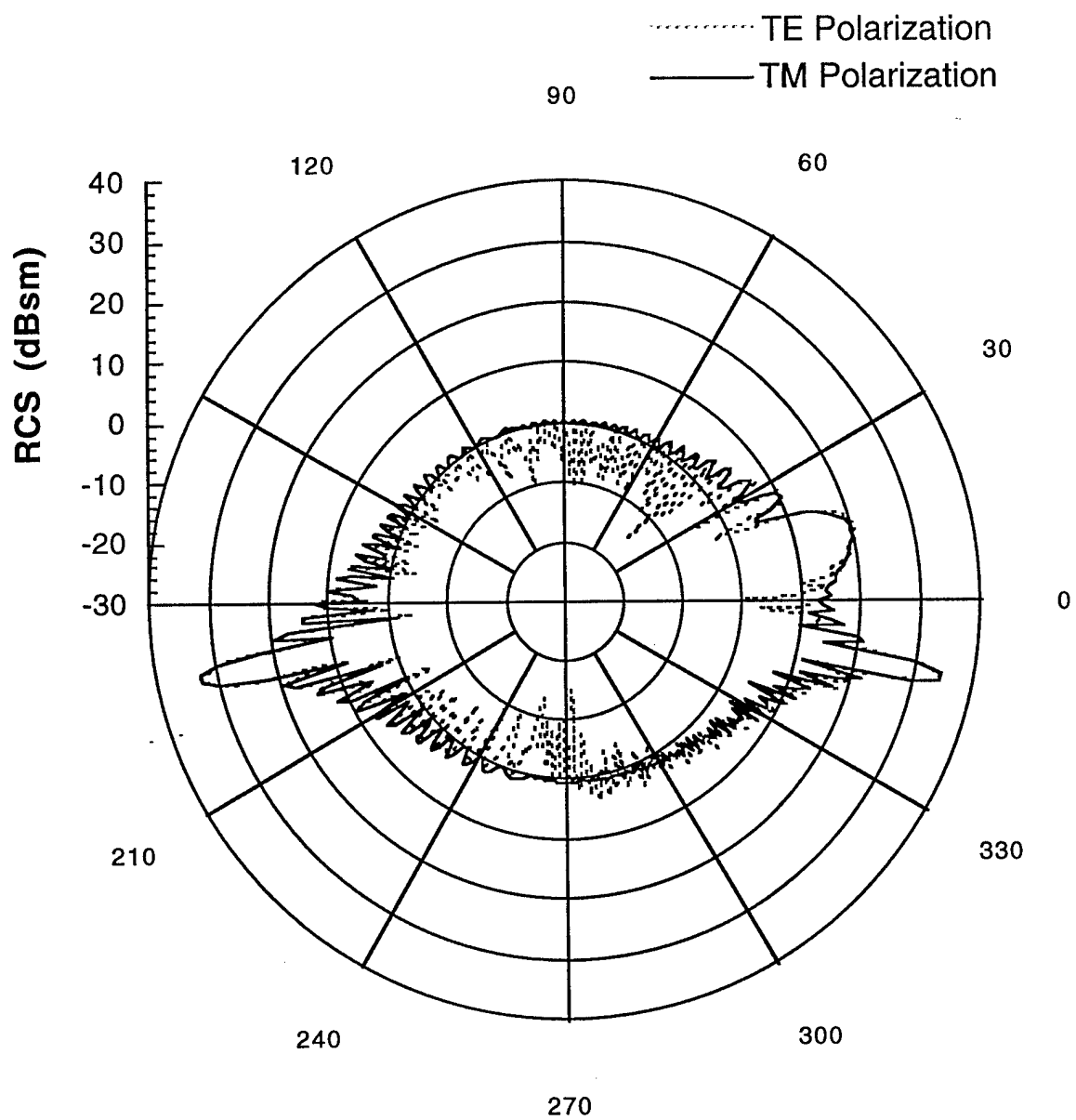


Figure B-41: Bistatic RCS of baseline cylinder ( $r = 0.5$  in.) at 9 GHz: Incident angle is 168 degrees (traveling wave angle).

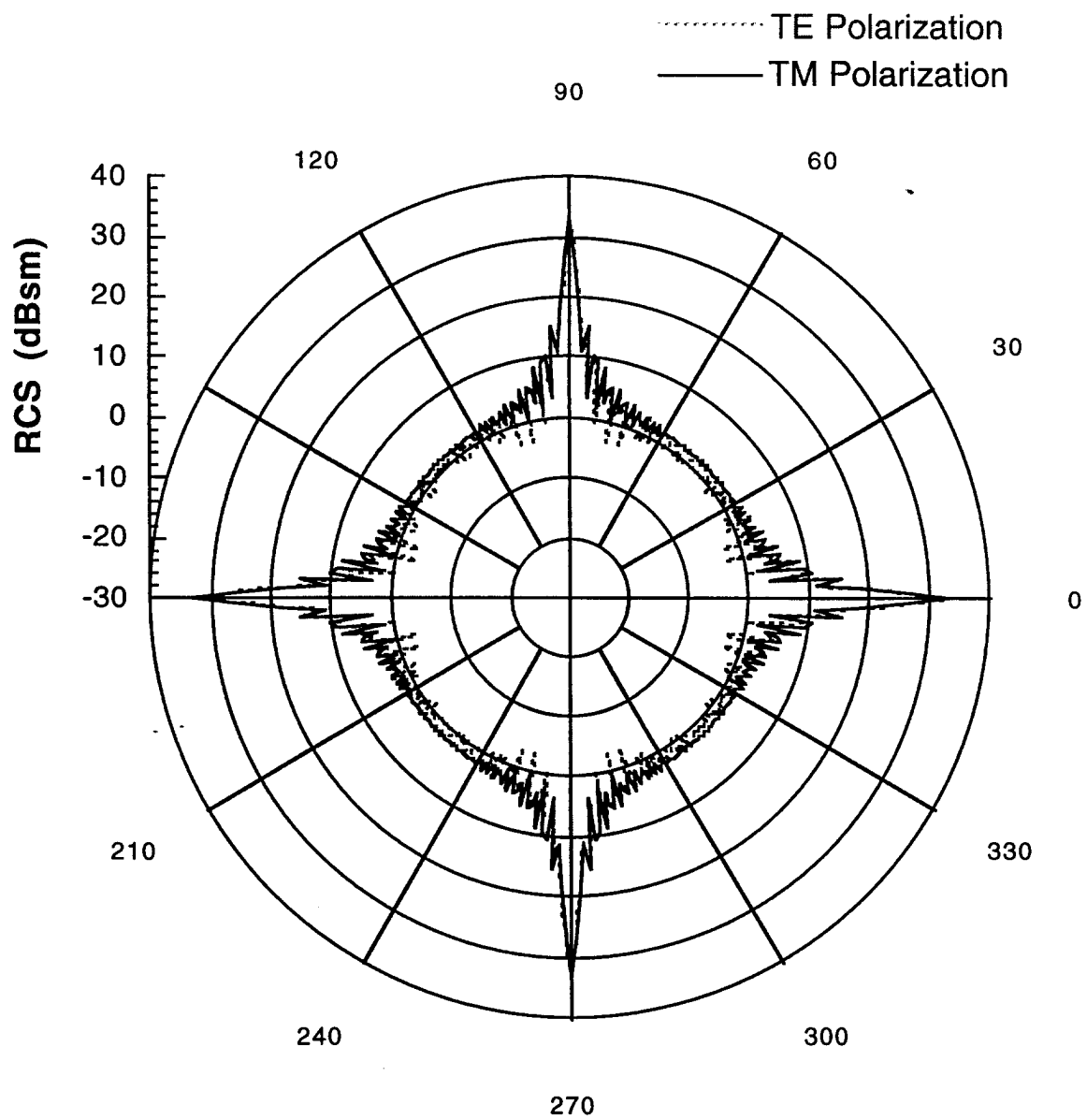


Figure B-42: Monostatic RCS of cylinder ( $r = 0.625$  in.) at 9 GHz

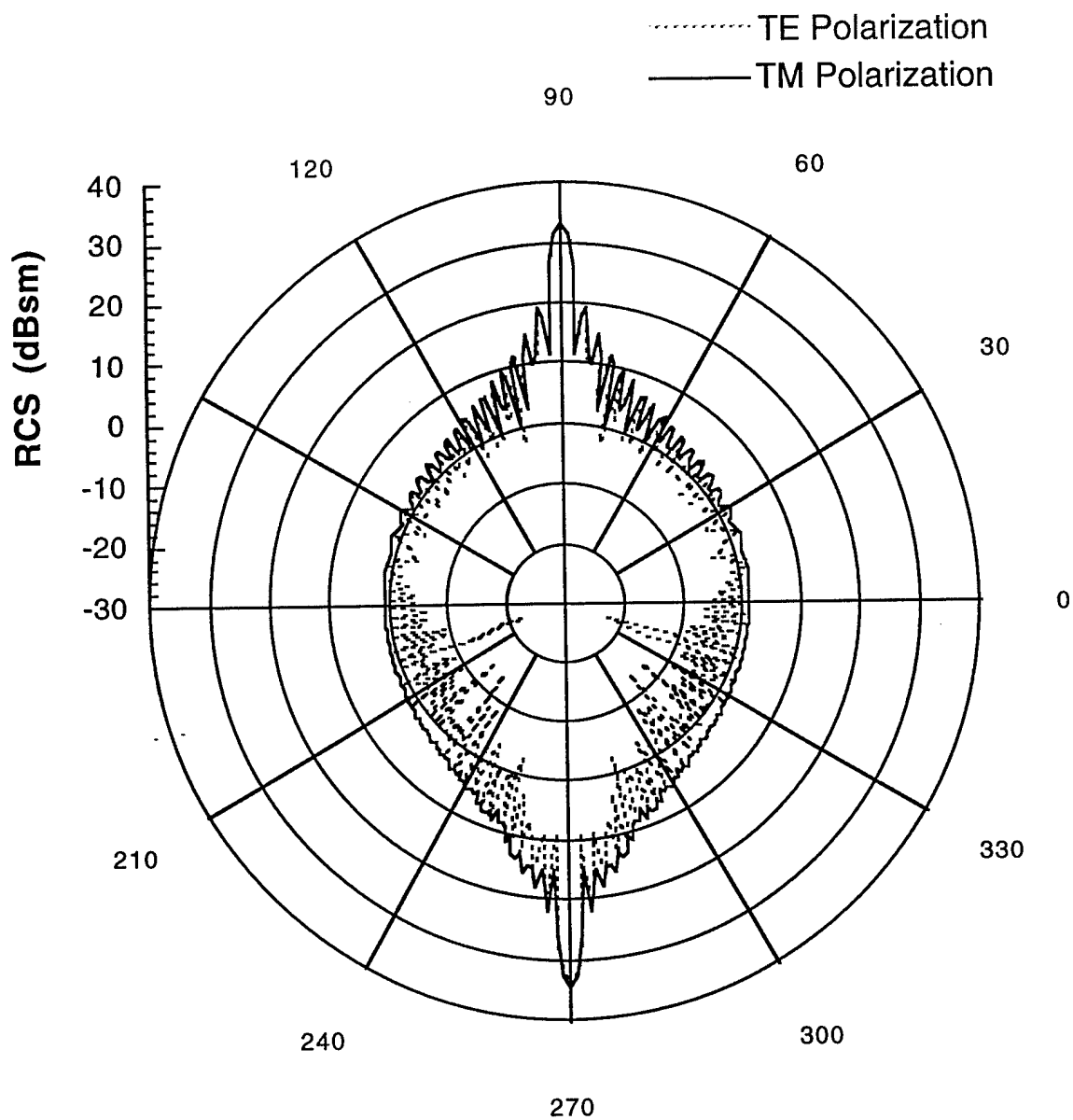


Figure B-43: Bistatic RCS of cylinder ( $r = 0.625$  in.) at 9 GHz: Incident angle is 90 degrees.

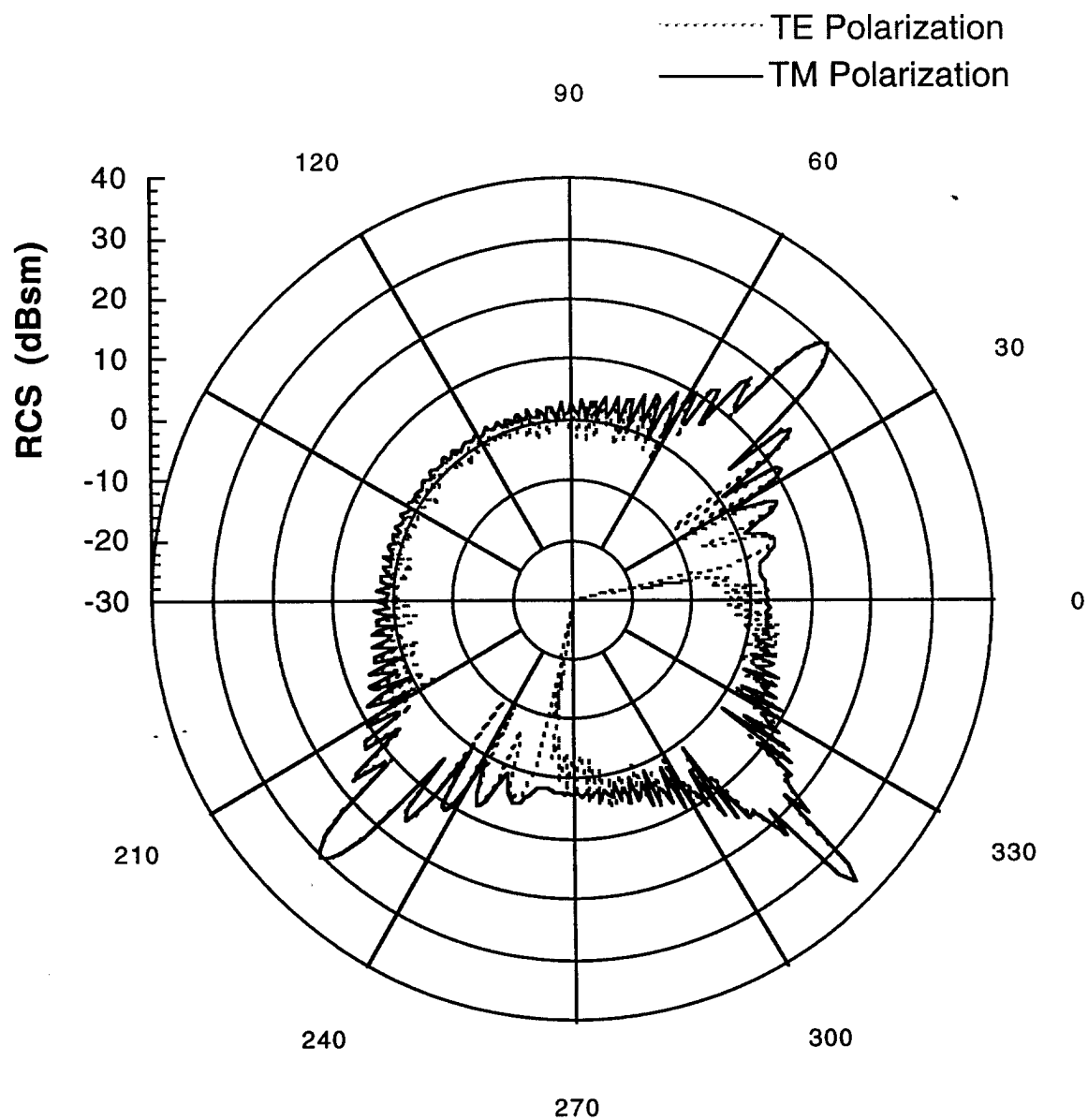


Figure B-44: Bistatic RCS of baseline cylinder ( $r = 0.625$  in.) at 9 GHz: Incident angle is 135 degrees.

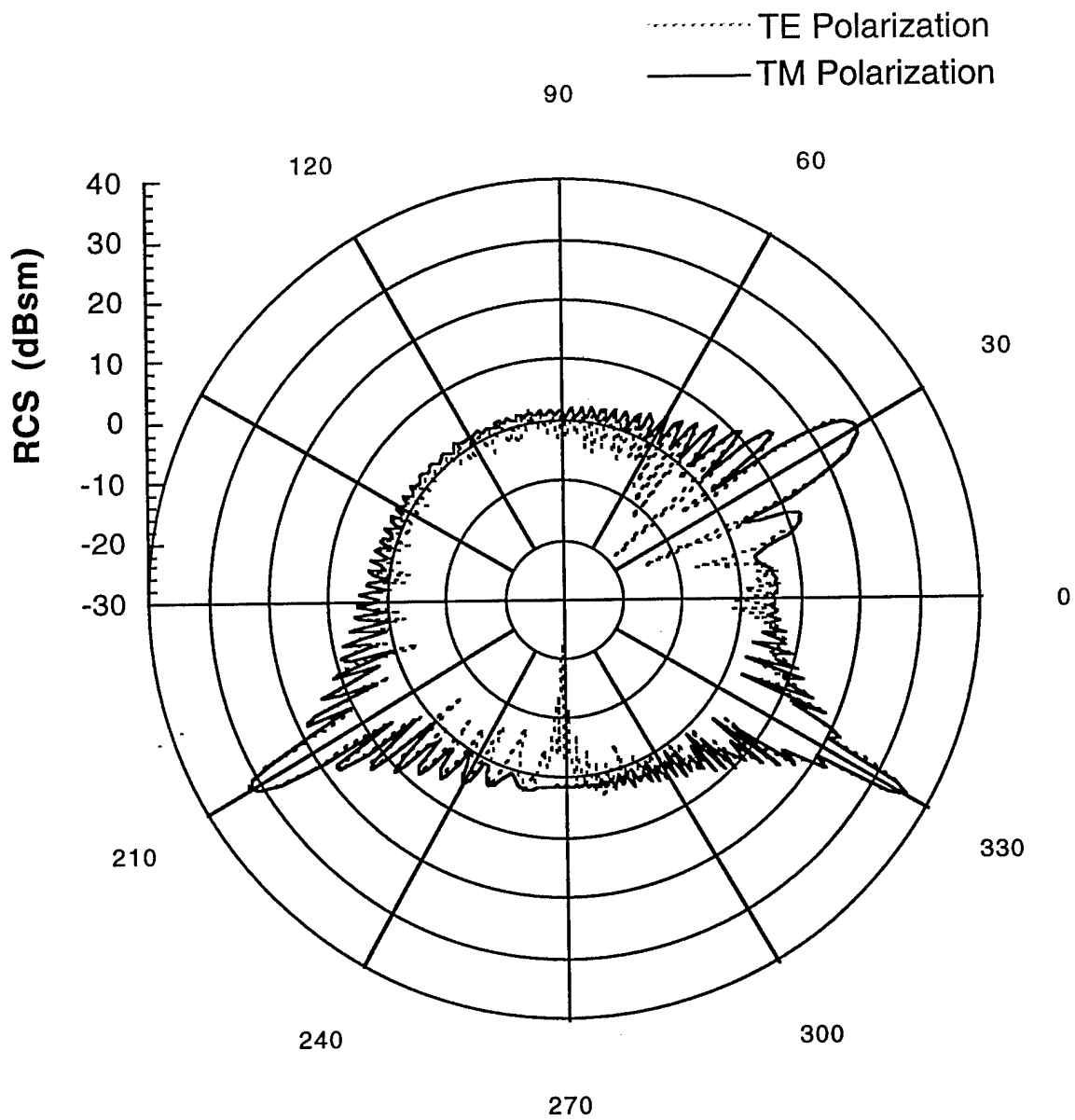


Figure B-45: Bistatic RCS of baseline cylinder ( $r = 0.625$  in.) at 9 GHz: Incident angle is 150 degrees.

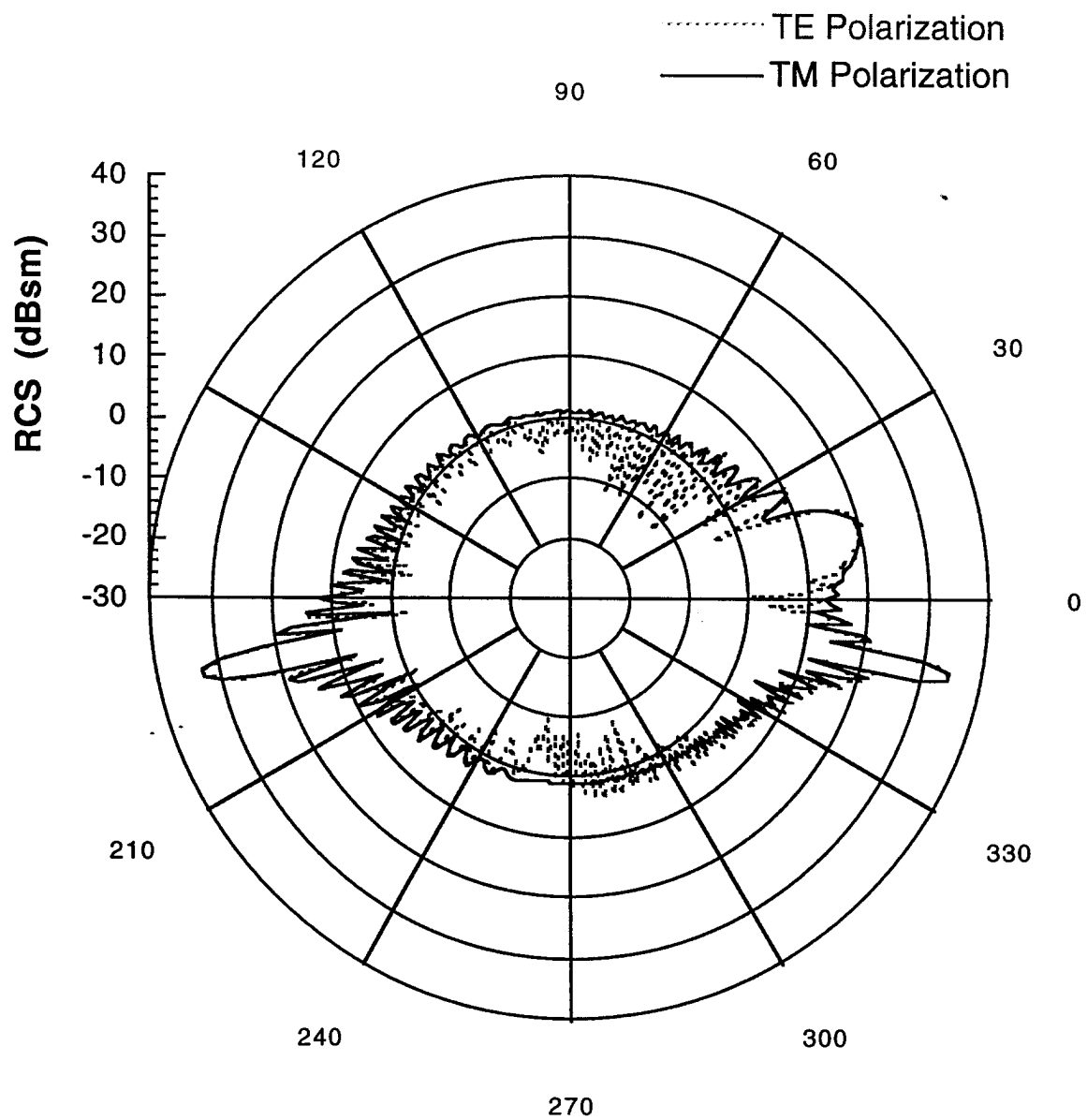


Figure B-46: Bistatic RCS of baseline cylinder ( $r = 0.625$  in.) at 9 GHz: Incident angle is 168 degrees (traveling wave angle).

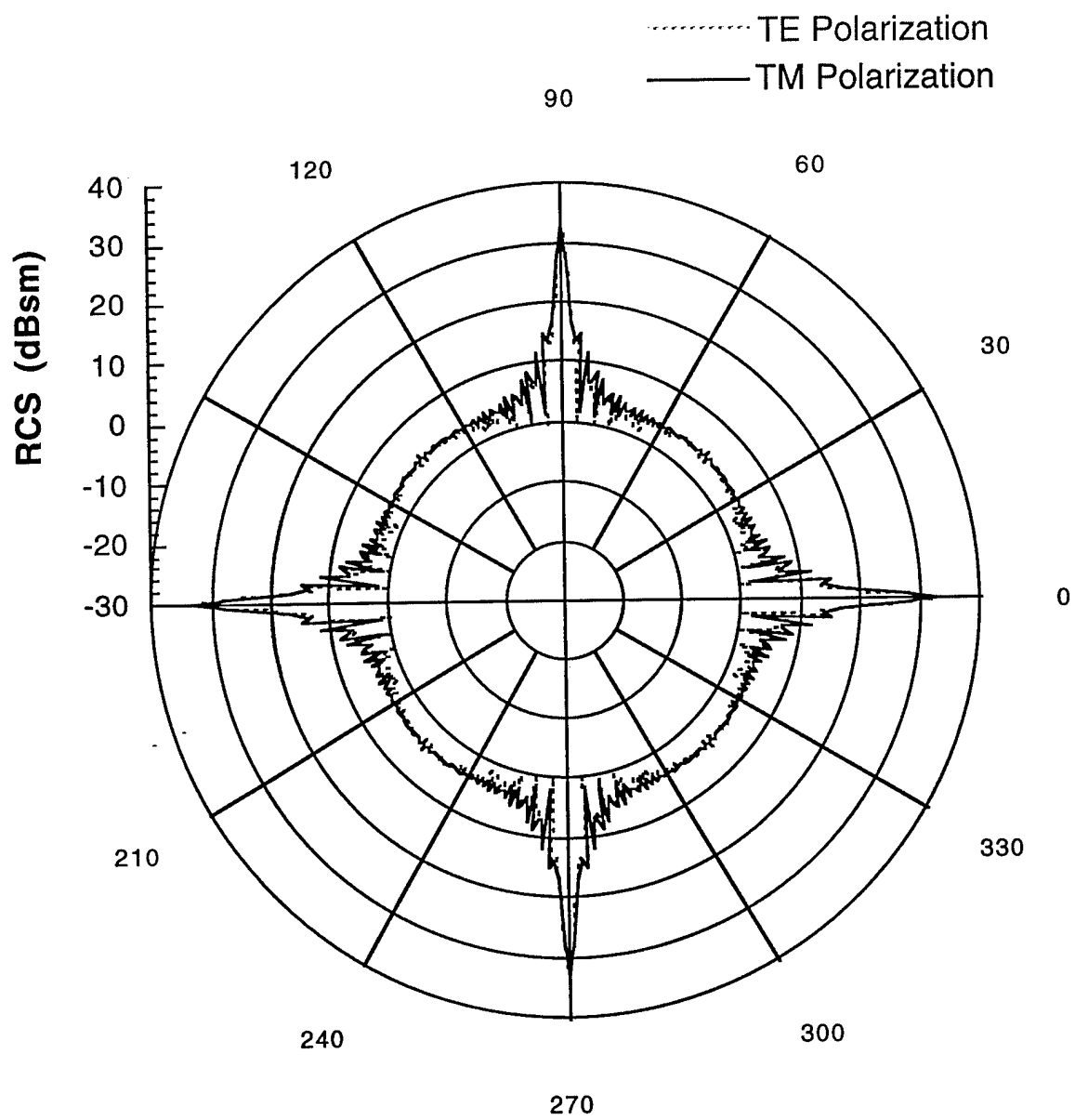


Figure B-47: Monostatic RCS of cylinder ( $r = 1.0$  in.) at 9 GHz



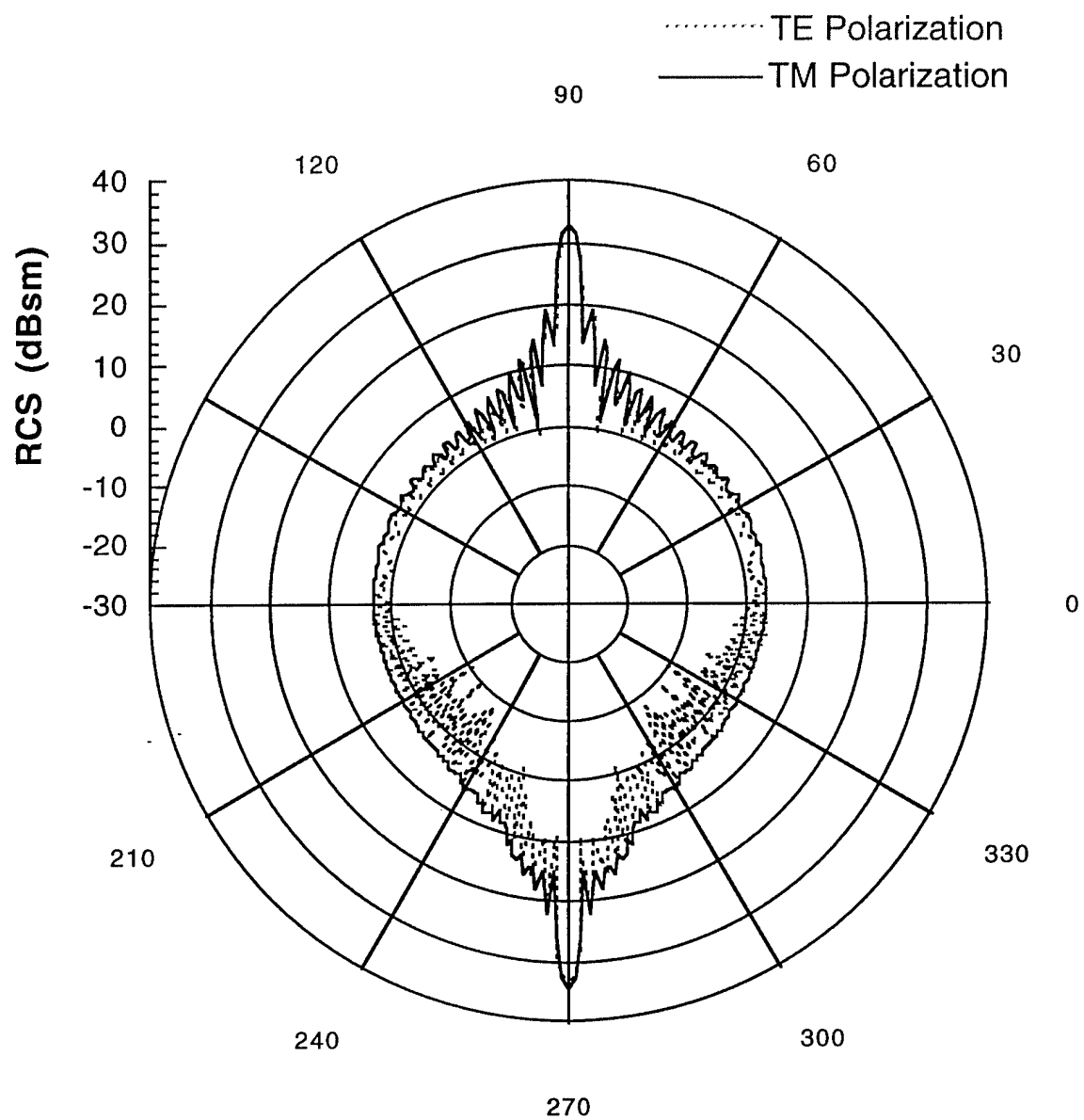


Figure B-48: Bistatic RCS of cylinder ( $r = 1.0$  in.) at 9 GHz: Incident angle is 90 degrees.

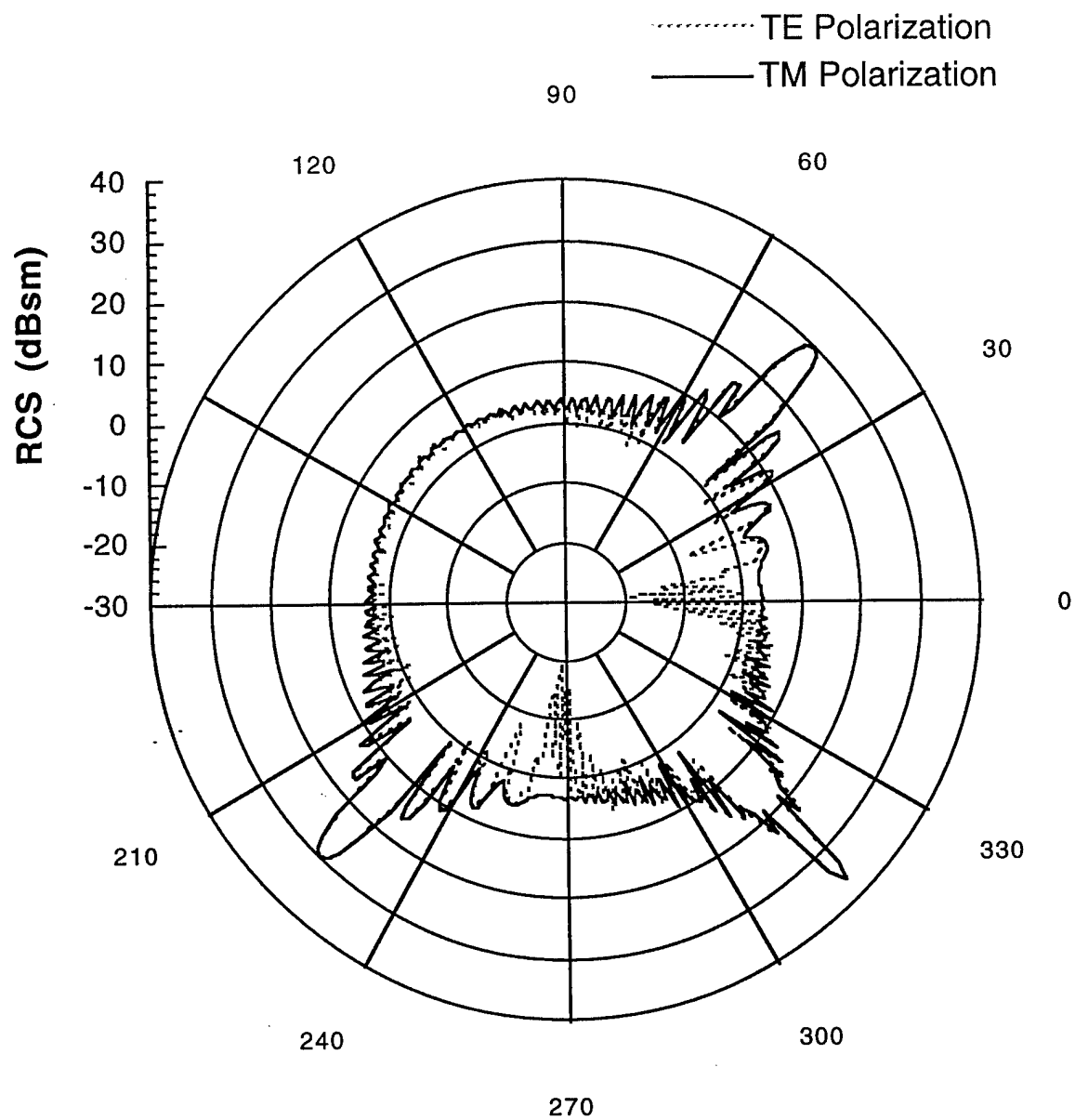


Figure B-49: Bistatic RCS of baseline cylinder ( $r = 1.0$  in.) at 9 GHz: Incident angle is 135 degrees.

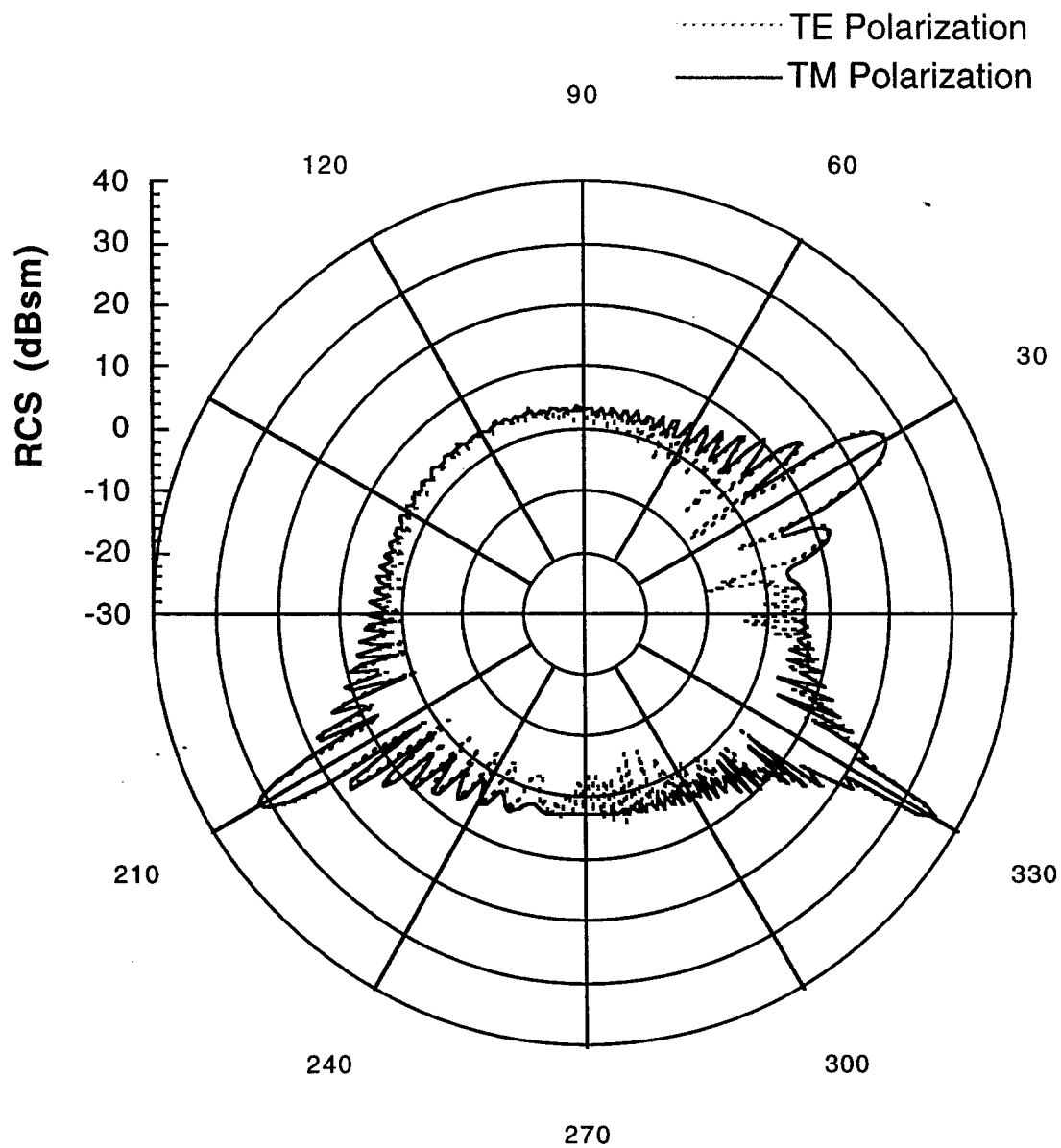


Figure B-50: Bistatic RCS of baseline cylinder ( $r = 1.0$  in.) at 9 GHz: Incident angle is 150 degrees.

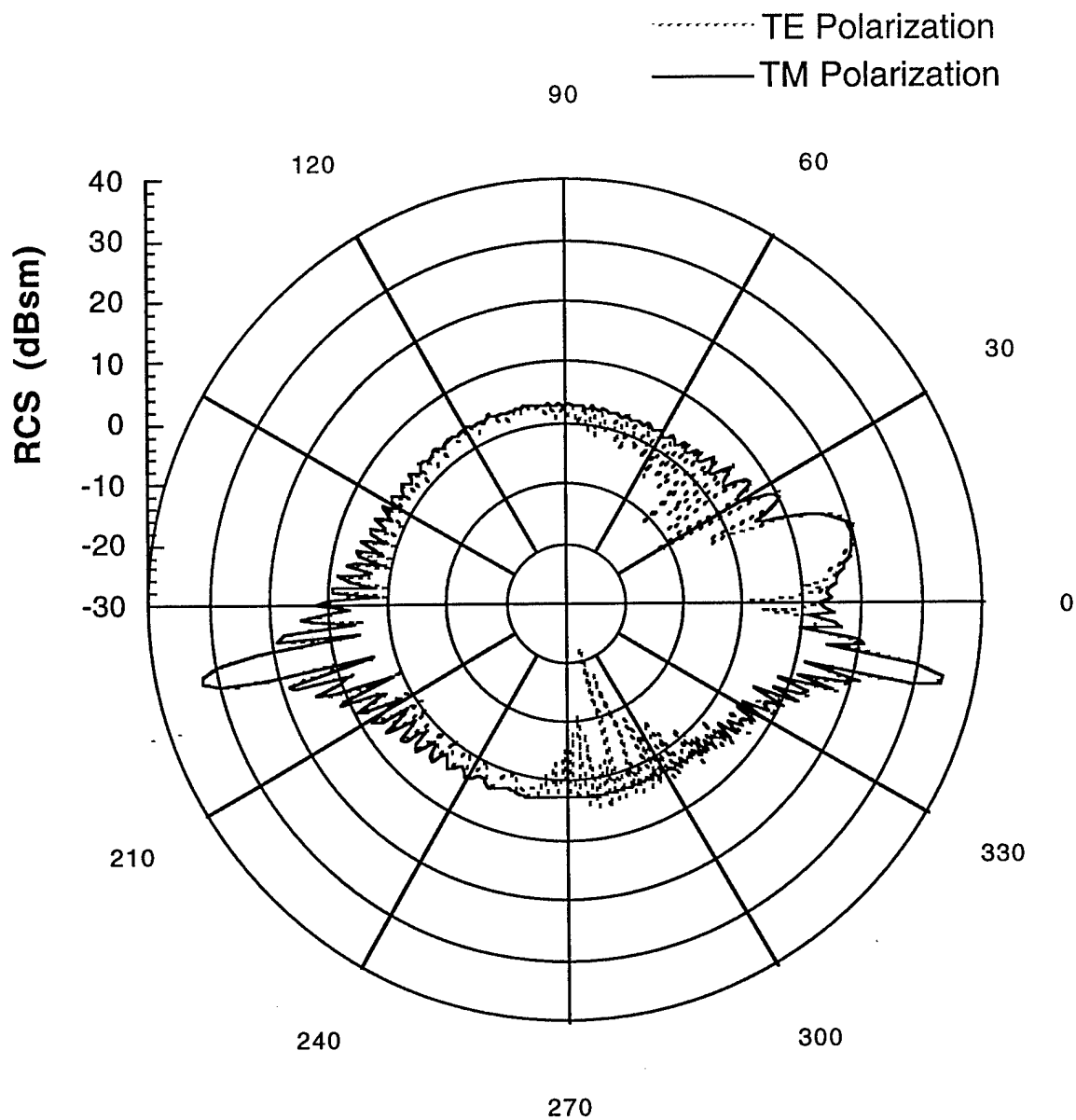


Figure B-51: Bistatic RCS of baseline cylinder ( $r = 1.0$  in.) at 9 GHz: Incident angle is 168 degrees (traveling wave angle).

## **APPENDIX C:**

### **TECHNOLOGY TRANSFER and NAVY RELEVANCE**

#### **Application of Techniques Developed**

The Ultra-Near Field Facility and the experimental and analytical techniques developed under this contract were used in a number of activities germane to Navy and NRL programs. Reflecting the infancy of ultra-near field measurements and holography, by necessity the activities listed below are of an exploratory nature. The primary purpose was to assess the feasibility of using ultra near-field techniques to gain a fuller understanding of various scattering and radiation phenomena involved. Some of these activities are continuing with the interested parties after the completion of this contract.

The experience and knowledge gained in the development of the Ultra-Near Field Facility under this contract has been incorporated into the design and installation of the new specialized Ultra-Near Field Facility in the Radar Division at NRL. Investigators on the present contract provided the technology transfer. In addition, the experience gained is being used in modifying and upgrading the original range used in this program.

Extensive measurements were done on NSWC supplied radar absorbing panels (LMS). These measurements provided unique probing of possible panel inhomogeneities that could impact the RCS properties of these panels.

Ultra-near field measurements were made for a variety of plates and dihedral fixtures, simulating some key aspects of ship topside structures. These results were supplemented with numerical simulations. Extrapolations of these results are being made with data obtained by NSWC on conducting cube-shaped targets. The sensitivity of the ultra-near fields and the  $\omega$ - $\kappa$  maps as a function of rounding the edges of the cubes is being investigated.

Measurements were made for the Naval Postgraduate School in support of near field back-projection studies for antennas. As an adjunct to these experiments, numerical simulations were also carried out to determine the extent of probe/antenna-under-test interactions and ways of minimizing them. Simultaneous calibration of magnetic and electric probes needed for cylindrical back-propagation has been achieved.

A limited feasibility study of the applicability of ultra-near field techniques was done to assess the crosspole performance of X-band and Ka-band feed horns used in the WINSAT program. In a related effort, the NRL range was used to make measurements on an end-fire slot array for the Space Sciences Division.

Exploratory near-field experiments were carried out for the SRI modified Sea Shadow scale model.

An electro-optic probe for use in ultra near-field measurements was delivered by Mission Research Corp. (MRC) to NRL at the end of this contract. This is a new design based on MRC's prior work for CRANE and NAVAIR (Pax River).

The NRL Ultra-Near Field range will be used by Material Sciences Division of NRL to demonstrate application of giant magnetoresistance (GMR) materials for sensor and antenna applications. Potential applications of this new technology include EW threat warning and IFOF among others.

Preliminary ultra-near field experiments were carried out for quasi-periodic arrays on different dielectric and R-card layers. The purpose of these experiments was to test the feasibility of using the NRL range to study the coupling and isolation of topside arrays on ship stacks/masts.

The experimental and simulation techniques developed under this contract are being transitioned to special programs under Dr. Saalfeld's cognizance.

#### **Impact/Navy Relevance:**

The combined experimental/computational ultra-near field techniques investigated so far, potentially provide fundamental diagnostic tools for:

- Identification of significant RCS contributors on ship stack/mast configurations, i.e. evanescent and propagating field behavior around gaps, edges and apertures;
- Quantification of antenna/array coupling and isolation effects using materials, screens and frequency selective surfaces in the reactive region of antennas;
- Assessment of array layouts and separation on finite complex surfaces, including curvature and truncation effects and coupling to neighboring ship structures;
- Synthesis and control of reactive fields for design of new classes of superdirective arrays using non-bidirectional materials;
- Design of new classes of materials having novel bandpass properties.

## REFERENCES

1. E.G. Williams, "Supersonic Acoustic Intensity," J. Acoust. Soc. Am. **97**, pp.121-127 (1995).
2. D. Taylor, P. Loschialpo, E. Williams, and W. Pala, "Dispersion Analysis of Surface Waves in the Near Field," Proc. PIERS, Cambridge, MA July 7-11, p.146 (1997).
3. D. L. Smith, S. Browning, S. Love, M. Morgan, and M. Parent, "Experimental Issues in Ultra Near-field Measurements," AMTA '99 Symp., Monterey, CA Oct. 4-8, pp. 8-12 (1999).
4. L.N. Medgyesi-Mitschang, P.G. Moore, D. L. Smith, and S. G. Lambrakos, "Bistatic Ultra Near-Field Holography for Imaging Surface Effects," PIERS 2000, Cambridge MA, July 2000.
5. ONR Program Review, Washington D.C., September 14, 2000.
6. M.G. Andreassen, "Scattering from Parallel Metallic Cylinders with Arbitrary Cross Sections," IEEE Trans. Antennas Propagat. **AP-12**, pp.746-754 (1964)
7. R.F. Wallenberg and R.F. Harrington, "Radiation from Apertures in Conducting Cylinders of Arbitrary Cross Section," IEEE Trans. Antennas Propagat. **AP-17**, pp. 56-62 (1969).
8. D.R. Wilton and R. Mittra, "A New Numerical Approach to the Calculation of EM Scattering Properties of Two-Dimensional Bodies of Arbitrary Cross Section," IEEE Trans. Antennas Propagat. **AP-20**, pp.310-317 (1972).
9. L.N. Medgyesi-Mitschang and J. M. Putnam, "Scattering from Finite Bodies of Translation: Plates, Curved Surfaces, and Noncircular Cylinders, IEEE Trans. Antennas Propagat. **AP-31**, pp. 847-852 (1983).
10. L.N. Medgyesi-Mitschang and J.M. Putnam, "Electromagnetic Scattering from Extended Wires and Two- and Three-Dimensional Surfaces," IEEE Trans. Antennas Propagat., **AP-33**, pp. 1090-1100 (1985).
11. J.M. Bornholdt and L.N. Medgyesi-Mitschang, "Mixed-Domain Galerkin Expansions in Scattering Problems," IEEE Trans. Antennas Propagat. **AP-36**, pp.216-227 (1988).

12. E.K. Miller, L. N. Medgyesi-Mitschang, and E. H. Newman, (Eds.) *Computational Electromagnetics: Frequency-Domain Method of Moments*, IEEE Press, Inc., New York, 1991.
13. I.S. Gradshteyn and I. M. Ryzhik, *Table of Integral, Series, and Products*, Academic Press, New York, 1980, p. 736, #6.677.3-4.
14. R.N. Bracewell, *The Fourier Transform and Its Applications*, Second Edition, Revised, McGraw-Hill Co., New York (1986).p. 93.
15. L.N. Medgyesi-Mitschang and J.M. Putnam, " Scattering from Composite Laminate Strips", IEEE Trans. Antennas Propagat. **AP-37**, pp. 1427-1436 (1989).
16. L.N. Medgyesi-Mitschang, J.M. Putnam, and M.B. Gedera, "Generalized Method of Moments for Three-dimensional Penetrable Scatterers," J. Opt. Soc. Am. **11**, pp. 1383-1398 (1994).
17. J.M. Putnam and M.B. Gedera, "CARLOS-3D: A General Purpose 3-D Method of Moments Scattering Code," IEEE Antennas Propagat. Mag. **35**, pp.69-71 (1993).
18. L. Peters, Jr., "End-fire Echo of Long Thin Bodies," IRE Trans. Antennas Propagat. **AP-6**, p.133, (1958).